

Electronic spectroscopy
of unsaturated hydrocarbons
and sulfur-terminated carbon chains
by cavity ringdown

Inauguraldissertation

Zur Erlangung der Würde eines Doktors der Philosophie
vorgelegt der Philosophisch-Naturwissenschaftlichen Fakultät
der Universität Basel

von

Alexey Denisov
aus Novosibirsk (Russland)

Basel, 2006

Genehmigt von der Philosophisch-Naturwissenschaftlichen Fakultät
auf Antrag von
Prof. Dr. John P. Maier und Prof. Dr. Martin Jungen

Basel, den 5. Juli 2006

Prof. Dr. Jakob Wirz

Dekan

To my mother

Acknowledgements

During the course of my Ph. D. studies, I had a chance to meet and work with very good people who deserve a great deal of credit for the work presented in this thesis.

I would like to thank Prof. John P. Maier for giving me the opportunity to work in his group. The excellent working environment and the resources to learn and do research during the period of my study are greatly acknowledged. I would also like to thank Prof. Martin Jungen for acting as the co-referee of my thesis.

I am grateful to PD. Dr. Harold Linnartz for introducing me to the experimental set-up and the laser technique. I would like to express my appreciation to Dr. Mitsunori Araki for his supervision and valuable comments.

I kindly thank my former and present coworkers Olga Peter-Vaizert, Pawel Cias, Elena Achkasova and Adam Nagy for their assistance with the experiment and moral support. I would like to thank all group members, especially Andrey Boguslavskiy, for fruitful discussions and enjoyable times.

I appreciate the help of Dr. Tomasz Motylewski who keeps supporting the CRD software that he has developed during his Ph. D. studies.

I am also grateful to the people who were technically involved in the experiment: Jacques Lecoultre for providing exotic isotopic species and Georg Holderied for solving all electronical problems. The experimental setup is supported and continuously improved by the workshop.

My sincere appreciations are given to Esther Stalder and Daniela Tischhauser from secretary office for taking care of bureaucratic matters and making my life easier. The Swiss National Science Foundation and the City of Basel are thanked for financial support.

TABLE OF CONTENTS

Table of contents	7
Chapter 1. Large carbon molecules in interstellar space.....	9
Introduction.....	9
Interstellar chemistry.....	10
Diffuse clouds.....	12
Dense clouds.....	13
Sulfur-bearing molecules.....	14
Large carbon molecules.....	15
Chapter 2. Rotational spectroscopy of polyatomic molecules	17
Linear molecules	17
Symmetric tops.....	18
Asymmetric tops.....	20
Chapter 3. History and principles of mass-spectrometry	22
Chapter 4. Experimental setup	27
Chapter 5. Sampling discharge plasma with quadrupole mass spectrometer	33
Introduction	33
Results and discussion.....	33
Mass spectrometry of sulfur-containing carbon plasma.....	38
Conclusions	38
Chapter 6. Spectroscopy of sulfur-terminated carbon chains in the gas phase.....	40
Introduction	40
Results and discussion.....	41
Conclusions	44
Chapter 7. Spectroscopy of nonlinear carbon chains	45
High-resolution electronic spectroscopy of a nonlinear carbon chain radical $C_6H_4^+$	45
Introduction	45
Results and discussion.....	46
Astrophysical relevance.....	52
Electronic spectroscopy of the nonlinear carbon chains $C_4H_4^+$ and $C_8H_4^+$	53
Results and discussion.....	55
Chapter 8. Unpublished results	62

Rotationally resolved spectrum of a vibrational band of ${}^2\Pi-X^2\Pi$ transition of C_6H	62
New measurement of C_5 absorption band at 510.93 nm.....	64
Refined position of $C_{10}H$ electronic absorption band.....	66
Chapter 9. An approach to the gas-phase absorption spectrum of C_{60}^+	68
Bibliography.....	71
Appendix A. Rotational lines assignment.....	79
Appendix B. Controlling the quadrupole mass spectrometer in LabView.....	85
Appendix C. Published papers.....	90
Electronic gas-phase spectrum of the pentaacetylene cation.....	91
Gas phase detection of cyclic B_3 : $2^2E' \leftarrow X^2A'_1$ electronic origin band.....	94
New laboratory data on a molecular band at 4429 Å.....	97
Rotational analysis of the $A^2B_1 \leftarrow X^2A_2$ electronic spectrum of the allyl radical.....	107
Gas phase electronic spectrum of propadienylyden C_3H_2	113
Curriculum vitae.....	119
The list of published papers.....	120

CHAPTER 1. LARGE CARBON MOLECULES IN INTERSTELLAR SPACE

Introduction.

The space between the stars is not absolutely empty as most people think. Since the beginning of the 20th century the study of physics and chemistry of the interstellar gas has played a prominent role in astrophysics. Most of the early work was focused on absorption line observations of diffuse interstellar clouds, which do not completely obscure the light from bright background stars. The electronic transitions of atoms and molecules can then be seen as sharp lines superimposed on the stellar spectra at visible and ultraviolet wavelengths. After the development of millimeter telescopes in the early 1970s, most of the interest shifted to the dense, dark molecular clouds where a rich chemistry is observed through the rotational emission lines of molecules.

The first interstellar molecules CH, CH⁺ and CN were identified between 1937 and 1941. However, evidence of much more complex species appeared 15 years earlier [1] that were later identified as interstellar [2]. Since then, more than 200 of such bands were discovered [3] which were called Diffuse Interstellar Bands (DIBs) for their broadness compared to sharp lines arising from atomic and diatomic species in space. A number of molecular carriers were suggested, such as CO₂, Na₂, O⁻, C⁻, H⁻, CH₄⁺, but all of them were disproved after careful laboratory studies. Numerosity of DIBs suggests that there is more than one molecule that is responsible for these absorptions and their broadness is usually attributed to the short lifetime of the excited electronic state or to the unresolved rotational structure of large molecules. Very likely DIB carriers are a class of molecules with similar structure, chemistry and cosmic abundances and the only prevalent element in space that is known to form a great diversity of large molecules is carbon.

The observation of unidentified, ubiquitous, molecular and solid-state features in astronomical spectra and the realization that these features are linked to carbonaceous materials have resulted in major scientific progress in the last 10 years. Laboratory and theoretical studies stimulated by these astronomical observations have led to a better understanding of the various forms of cosmic C such as polycyclic aromatic hydrocarbons (PAHs), C-chain molecules, carbon clusters, and carbonaceous solids. Ultimately, these astrophysically motivated investigations have led to the detection of novel forms of C and laid the foundations for the chemistry of fullerenes.

Astronomical observation of molecules helps to determine chemical pathways by which they are formed hence giving an insight into an interstellar chemistry. Each new studied and detected molecule provides a test for existing theories of interstellar chemistry. Laboratory astrophysics provides a realistic simulation of the conditions that exist in a given cosmic environment and gives quantitative data that are relevant to the interpretation of space observations.

Interstellar chemistry.

The interstellar medium (ISM) consists of gas and dust between the stars, which accounts for 20–30% of the mass of our galaxy. Much of this material has been ejected by old and dying stars. The ISM contains different environments showing large ranges in temperature ($10\text{--}10^4$ K) and densities ($100\text{--}10^8$ hydrogen atoms cm^{-3}). It is filled mainly with hydrogen gas, about 10% helium atoms and about 0.1% of atoms like C, N and O. Other elements are even less abundant. Roughly 1% of the mass is contained in microscopic dust grains. Molecular clouds and diffuse clouds occupy only a few percent of the interstellar space, though they contain almost 100% of its mass. The clouds are surrounded by warm, neutral intercloud gas and hot, ionized coronal gas that together fill most of the space (Table 1).

Table 1. Characteristic parameters of the various regions of interstellar space.

	Coronal gas	Radiatively ionized regions	Intercloud gas	Diffuse clouds	Molecular clouds
Temperature (K)	10^6	10^4	$10^3\text{--}10^4$	10^2	10
Density (cm^{-3})	$< 10^{-2}$	10^2	1	10^2	10^4
Identifiers	O VI	H, 656nm	21 cm	21 cm	CO, J=1-0
Fractional ionization	1	1	0.1	10^{-3}	10^{-7}
Filling factor	~50%	<1%	~50%	3%	<1%
Mass fraction				~50%	~50%

Carbon is a major player in the evolutionary scheme of the universe because of its abundance and its ability to form complex species. It is also a key element in the evolution of prebiotic molecules. Carbon plays an important role in the physical evolution of the ISM

because it is the main supplier of free electrons in diffuse IS clouds, thus contributing to the heating of IS gas. Carbon has an ionization potential (EI = 11.3 eV) below the Lyman edge, so C is almost completely ionized in space, with the exception of C in dense clouds. Currently the interstellar carbon abundance is considered to be 225 ± 50 ppm (atoms per 10^6 H atoms) [4], therewith the amount of carbon in gas phase is estimated to be 140 ± 20 ppm [5].

Table 2. The 129 reported interstellar and circumstellar molecules. [6]

Diatomic	Triatomic	Four Atoms	Five Atoms	Six Atoms	Seven Atoms	Eight Atoms	Nine Atoms	Ten Atoms
H ₂	C ₃	c-C ₃ H	C ₅	C ₅ H	C ₆ H	CH ₃ C ₃ N	CH ₃ C ₄ H	CH ₃ C ₅ N?
AlF	C ₂ H	l-C ₃ H	C ₄ H	l-H ₂ C ₄	CH ₂ CHCN	HCOOCH ₃	CH ₃ CH ₂ CN	(CH ₃) ₂ CO
AlCl	C ₂ O	C ₃ N	C ₄ Si	C ₂ H ₄	CH ₃ C ₂ H	CH ₃ COOH?	(CH ₃) ₂ O	NH ₂ CH ₂ COOH?
C ₂	C ₂ S	C ₃ O	l-C ₃ H ₂	CH ₃ CN	HC ₅ N	C ₇ H	CH ₃ CH ₂ OH	CH ₃ CH ₂ CHO
CH	CH ₂	C ₃ S	c-C ₃ H ₂	CH ₃ NC	HCOCH ₃	H ₂ C ₆	HC ₇ N	
CH+	HCN	C ₂ H ₂	CH ₂ CN	CH ₃ OH	NH ₂ CH ₃	CH ₂ OHCHO	C ₈ H	
CN	HCO	CH ₂ D ⁺ ?	CH ₄	CH ₃ SH	c-C ₂ H ₄ O	CH ₂ CHCHO		
CO	HCO ⁺	HCCN	HC ₃ N	HC ₃ NH ⁺	CH ₂ CHOH			
CO ⁺	HCS ⁺	HCNH ⁺	HC ₂ NC	HC ₂ CHO				
CP	HOC ⁺	HNCO	HCOOH	NH ₂ CHO				
CsI	H ₂ O	HNCS	H ₂ CHN	C ₅ N				
HCl	H ₂ S	HOCO ⁺	H ₂ C ₂ O	HC ₄ N				
KCl	HNC	H ₂ CO	H ₂ NCN					
NH	HNO	H ₂ CN	HNC ₃					
NO	MgCN	H ₂ CS	SiH ₄					
NS	MgNC	H ₃ O ⁺	H ₂ COH ⁺					
NaCl	N ₂ H ⁺	NH ₃						
OH	N ₂ O	SiC ₃						
PN	NaCN	C ₄						
SO	OCS							
SO+	SO ₂							
SiN	c-SiC ₂							
SiO	CO ₂							
SiS	NH ₂							
CS	H ₃ ⁺					Eleven Atoms	Twelve Atoms	Thirteen Atoms
HF	SiCN					HC ₉ N	CH ₃ OC ₂ H ₅	HC ₁₁ N
SH	AlNC							
FeO(?)	SiNC							

Molecules that are found in the interstellar space vary from simple diatomic to complex polyatomic chains that are very exotic in the terrestrial environment (Table 2). Certain molecules are easier to detect than others. For example, energy levels structure of linear carbon chain molecules is simple enough and for a given energy there are not many ways for it to be distributed, thus individual spectral lines can be quite strong. The energy levels structure of nonlinear molecules is very complicated and do produce the signal of similar strength the molecule would have to be several orders of magnitude more abundant than the linear one.

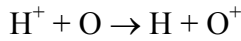
There is a variety of processes that can lead to the formation of molecules in the interstellar medium. These are mainly ion-neutral reactions because they are about a hundred times faster than neutral-neutral reactions. The latter can also have an activation barrier that would block the reaction pathway at low temperatures. Substantial chemical differences can be observed between molecular clouds that might be due to different physical conditions. Therefore using appropriate models one can try to derive from molecular composition the physical parameters of the clouds such as temperature, gas density, and radiation intensity.

Despite the long history of gas-phase chemical modeling (see [7], [8] and references therein) and the large amount of observational work, some long-standing enigmas and a few recent failures push for a re-visitation of commonly accepted schemes and hint that diffuse clouds are much more complex than usually assumed. Among these enigmas, observations show that complex molecules may achieve dark clouds abundances in the diffuse ISM [9]. The interpretation of such a phenomenon is still lacking a robust observational scenario and it is doubtful whether present theoretical models may be reconciled with observed column densities.

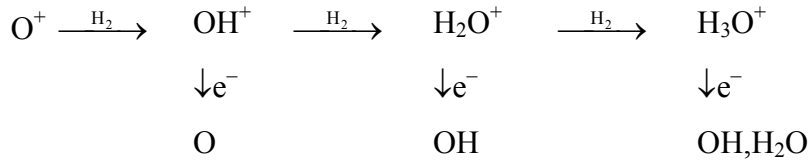
Diffuse clouds

The intensity of interstellar UV in diffuse clouds is so high that it can easily dissociate most molecules so that a substantial fraction of matter in diffuse clouds remains in the atomic form. Thus, the major species are H atoms and H₂ molecules. The first chemical model of diffuse clouds was proposed by Black and Dalgarno [10] in 1977 and was later refined by van Dishoeck [7].

The main gas phase reaction paths are now well established. Protons created by cosmic ray ionization can undergo an accidental resonance charge exchange with oxygen atoms, creating O⁺ which is able to react efficiently with H₂:



and O^+ reacts further

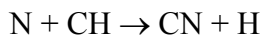
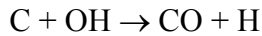


This is a fairly standard behavior: ion-molecule reactions will go until no further reactions are possible and then recombination with electrons gives neutral products.

The chemical network describing the formation of simple C molecules in diffuse clouds, where C is mostly ionized, begins with the radiative association reaction of C^+ with H_2 . The resulting CH_2^+ reacts with H_2 to form CH_3^+ , which produces CH and CH_2 through dissociative recombination with electrons.



The reaction of these neutral molecules with C^+ leads to the formation and build-up of polyatomic hydrocarbons. This reactional scheme is limited, however, by the photodissociation of the neutral molecules at short and moderate depths and by the lockup of C in the stable CO molecule at greater depths in the cloud.

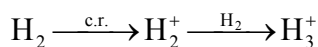


Dense clouds

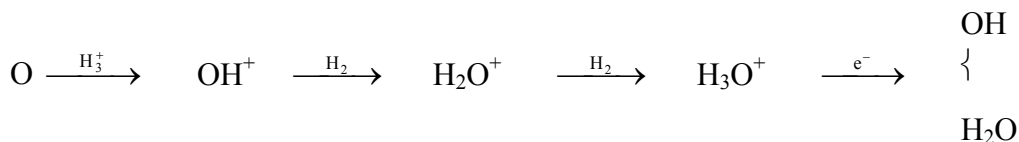
Cold, dark molecular clouds were discovered originally as dark patches on the sky but have subsequently been traced in molecular line emission. These clouds are particularly rich in molecules and often contain many of those listed in Table 2. Cold gas chemistry can efficiently form simple species such as CO, N_2 , O_2 , C_2H_2 , C_4H_2 , HCN and simple carbon chains [11]. Although UV radiation cannot reach the inside of the cloud, cosmic rays can penetrate deeply and ionize H_2 molecules. The energetic electrons from these molecules can in turn electronically excite other H_2 molecules making them to emit UV photons.

Studies in the infrared and radio regions show that many dark clouds are regions of low-mass star formation. The chemistry in dark clouds is somewhat similar to the chemistry in diffuse clouds, but the ultraviolet radiation intensity and the rates of photodissociation are greatly reduced. The higher densities lead to faster formation than in diffuse regions and

slower rates mean that abundances of molecules tend to be higher in dark clouds than in diffuse clouds. Cosmic rays will be driving the gas phase chemistry through the ion H_3^+ that arises directly from the ionization of H_2 :



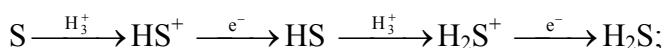
and H_3^+ is a proton donor which initiates many sequences of reactions, for example:



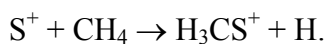
In dense clouds shielded from UV radiation, C is mostly neutral and the C chemistry starts with the reaction of C with H_3^+ and the formation of CH_3^+ by the formation of CH^+ and CH_2^+ . Complex hydrocarbons (such as CH_2CO , CH_3CN , and C_nH_m) are subsequently produced through C insertion reactions, condensation reactions, and radiative association reactions.

Sulfur-bearing molecules

The chemistry leading to the formation of the sulfur-bearing molecules in the interstellar space probably begins with S or S^+ ions as sulfur has low ionization energy. Reactions of these two species with H_2 are endothermic and will not occur in cold molecular gas at a significant rate. A possible route to H_2S is the following;

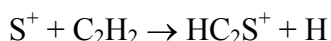


There are several interstellar molecules with C–S bonds (Table 2). As S^+ does not react with H_2 , it is available to react with lesser abundant species, including hydrocarbons.



By dissociative recombination the product ion H_3CS^+ can form H_2CS and CS .

The reaction



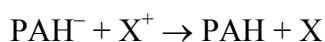
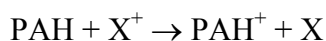
could be the first stage of the formation of C_2S . Similarly, the reaction of S^+ with CH_3CCH could result in C_3S .

Large carbon molecules

It has been shown [12] that polyacetylenic carbon chains and PAHs are a major products of the acetylene polymerization at high temperatures (1500-3000 K). Such processes are common in hydrocarbon flames and combustion, eventually leading to the formation of soot. Once the intermediates of these processes are established and characterized spectroscopically, it is possible to study these hostile environments remotely and revise the network of chemical processes that take place there. The same approach applies to the interstellar chemistry. Although no optical/UV features have been attributed yet to the spectra of large carbon molecules, the microwave spectra of molecular clouds confirm the presence of polyacetylenic chains of up to 13 atoms [13] and the observed mid-infrared features in the diffuse ISM are very characteristic of aromatic species.

The first large carbon chain molecules that were detected in molecular clouds were cyanopolyynes HC_{2n+1}N for $n=2..5$ [13-16]. The detection of such exotic and unexpected species has raised a number of questions. It seems reasonable that in the medium that consists mainly of hydrogen with only minor amounts of carbon and nitrogen highly saturated molecules would be readily produced. Nevertheless, searches for hydrogen-containing carbon chains in the interstellar space have shown that as a chain with a given number of carbon atoms adds more H the relative abundance drops rapidly and the numerous hydrocarbon derivatives are essentially absent [17]. There could be an unidentified chemical pathway that preferentially leads to the formation of long chains but it is also likely that these species are formed in a completely different scenario. In denser shells of C-stars carbon atoms can form dust particles and it is likely that the carbon chains are some form of intermediates or breakdown products. Since the interstellar dust is also assumed to be covered with amorphous carbon [18] and it was shown [19] that amorphous carbon can be considered as a collection of loosely bound molecular clusters, one can expect carbon chain molecules to appear in diffuse clouds as well [20] leaving grain surface through heat-up by collisions with other grains or with cosmic rays. Although the exact pathway is not known, it is clear that some processes must occur that limit the carbon mantle grown and return the carbon to the gas phase.

Large molecules such as polycyclic aromatic hydrocarbons PAHs can affect the chemistry of both diffuse and dense clouds through charge-transfer and neutralization reactions [21]



Of specific importance for the PAH production is the formation of the first aromatic ring which is benzene. This molecule and its radicals are formed by the spontaneous closure of a highly flexible C_6H_m chain molecule. The type of chains is restricted by flexibility and state of saturation.

Flexibility: since polyacetylenes are rather stiff molecules, the activation energies for closure of such structures are too high. The chain molecule has to contain more than two hydrogen atoms to dispose of at least one sp^2 hybridized carbon atom.

Saturation: at low pressures less saturated hydrocarbons are preferred.

One of the possible mechanisms of the PAH formation is shown on Figure 1.

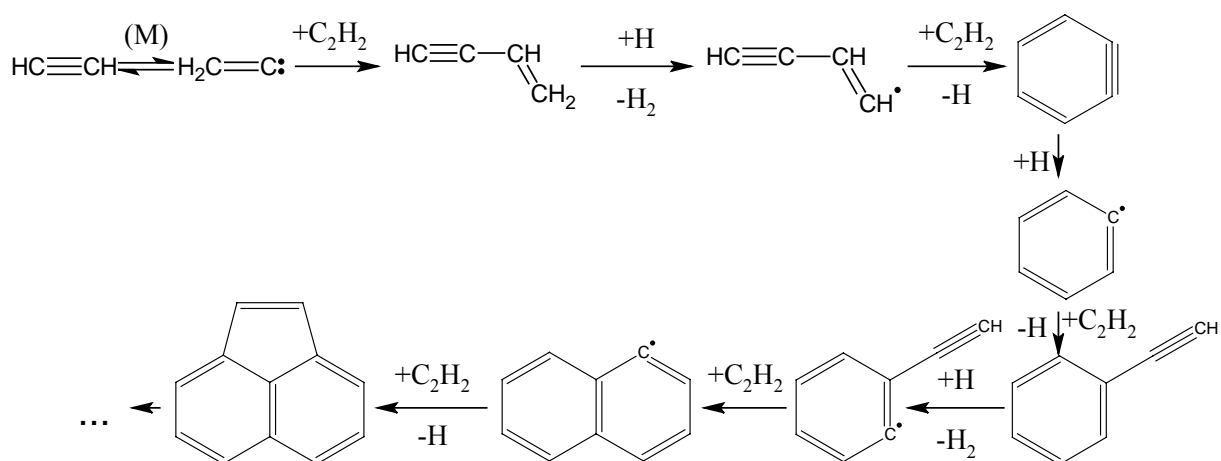


Figure 1. The dominant reaction pathway for the formation of polycyclic aromatic hydrocarbons in circumstellar envelopes[22]

The laboratory experiments and calculations [23] suggest that unimolecular ring closure is more effective than a Diels-Alder addition reaction towards benzene and the ultimate intermediate is $\text{HC}\equiv\text{C}-\text{C}\equiv\text{C}-\text{CH}=\text{CH}_2$. Astronomical detection of such nonlinear chains could be a way to visualize the regions of PAH formation. Up to now, very little is known about the electronic structure of such nonlinear carbon chains and their spectroscopic properties. In this work, the first electronic spectra of cations $\text{C}_{2n}\text{H}_4^+$ ($n=2-4$) are presented and molecular geometries are determined from the rotational structure.

CHAPTER 2. ROTATIONAL SPECTROSCOPY OF POLYATOMIC MOLECULES

High resolution spectroscopy is one of the most reliable methods to determine molecular structure. The main problem is that molecules have not more than three moments of inertia which is usually not enough to determine the large number of bond angles and lengths. When possible, isotopically substituted molecules can be studied, assuming that molecular geometry does not change. Nevertheless, even a set of three rotational constants can be a sufficient to discriminate between different proposed geometries of observed molecule.

In general, a molecule can rotate about three geometric axes and can have three different moments of inertia relative to these axes. The moment of inertia about an axis is defined as

$$I = \sum_i m_i r_i^2$$

where r_i is a distance from the atom to the axis. The axes are chosen in such a way that the tensor of moment of inertia is diagonal. The three moments of inertia, I_x , I_y and I_z determine the layout of the rotational levels of molecule. The internal molecular axes are labeled as A, B, C so that $I_A \leq I_B \leq I_C$. It is conventional to classify molecules into the following categories:

linear molecules $I_A = 0, I_B = I_C$,

spherical tops, $I_A = I_B = I_C$,

prolate symmetric tops, $I_A < I_B = I_C$,

oblate symmetric tops, $I_A = I_B < I_C$,

asymmetric tops, $I_A < I_B < I_C$.

Linear molecules

The rotational energy levels of rigid linear molecule are given by

$$E_{\text{rot}} = BJ(J+1)$$

where J is the rotational quantum number and B is the rotational constant defined as

$$B = \frac{h^2}{8\pi^2 I_B}$$

A real molecule is not a rigid rotor because the bond between atoms A and B can stretch at the same time as the molecule rotates. As rotation increases, the centrifugal force stretches the bond, increasing r and decreasing the effective B value. The bond length also depends, in an average sense, on the vibrational state v . The non-rigid rotor energy level equation for vibrational state v is

$$F_v(J) = B_v J(J+1) - D_v [J(J+1)]^2 + \dots$$

where D_v and higher order terms are centrifugal distortion constants. The influence of a vibrational excitation is given as

$$B_v = B_e - \sum_i \alpha_i \left(v_i + \frac{1}{2} \right)$$

neglecting higher order terms, where B_e is the rotational constant of equilibrium geometry and α_i – constants of rotation-vibration interaction.

The selection rules for *rovibronic* transitions (i.e. transitions that involve electronic excitation of molecule) are $\Delta J = 0, -1, +1$, giving rise to the Q-, P- and R-branches of the rotational structure, respectively.

Symmetric tops

A *symmetric top* rotor has the same moment of inertia about two principal axes. The three moments of inertia about these three principal axes are labeled I_a , I_b and I_c , with the convention that $I_c \geq I_b \geq I_a$. A symmetric top can have the two larger moments of inertia equal ($I_c = I_b > I_a$), which is called a prolate rotor, or it can have the two smallest moments of inertia equal ($I_c > I_b = I_a$), which is called an oblate rotor. If a molecule has a symmetry axis of three- or more fold symmetry, it is always a symmetric top. Molecules of lower symmetry can be near-symmetric tops, having two rotational constants of close values and with a lack of spectral resolution they can behave like symmetric tops. Similar to linear molecules, a symmetric top has one of the principal axes along the molecular symmetry axis. In a prolate symmetric top, the a -axis lies along the symmetry and in an oblate symmetric top it is the c -axis. The rotational energy levels for the ground vibrational state of a rigid prolate symmetric top are represented as

$$E_{J,K} = B J(J+1) + (A - B)K^2,$$

where K is the projection of the total angular momentum, on the symmetry axis. For an oblate symmetric top,

$$E_{J,K} = B J(J+1) + (C - B)K^2,$$

The value of K must not be greater J then as it represents the component of J . Since the energy does not depend on the sign of K , all states with the exception of $K = 0$ are doubly degenerate, corresponding to opposite directions of rotation around the symmetry axis. Figure 2 shows the energy level diagram for symmetric top molecules. Every K ladder has the structure rotational levels same as linear molecule but offset by $(A - B)K^2$ in energy.

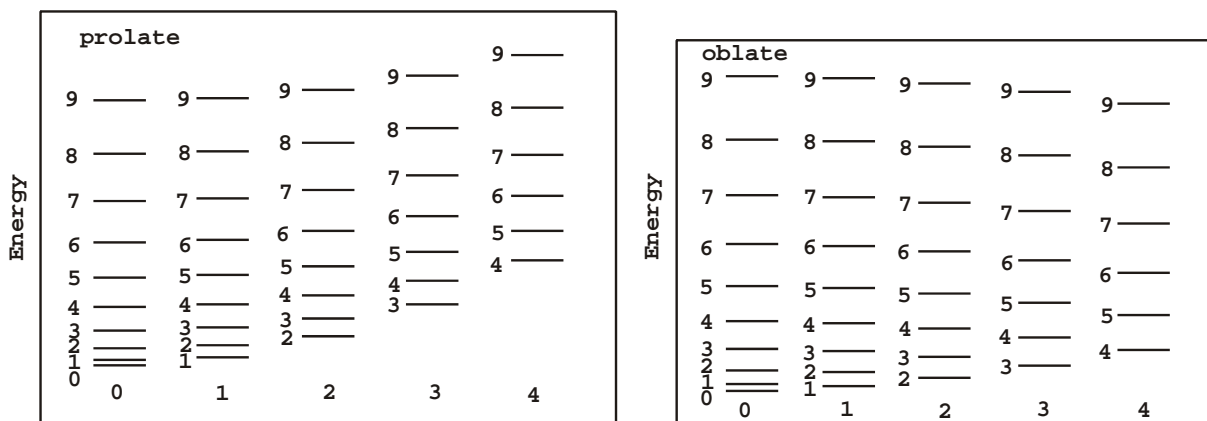


Figure 2. Energy levels of symmetric top.

The spectra of linear and symmetric tops can generally be classified as parallel and perpendicular depending upon the direction of the electronic transition dipole moments. Parallel transitions occur when a transition moment is aligned along the symmetry axis of the molecule within a given K ladder

$$\Delta K = 0 \text{ and } \Delta J = \pm 1 \text{ for } K = 0,$$

$$\Delta K = 0 \text{ and } \Delta J = 0, \pm 1 \text{ for } K \neq 0.$$

In the rigid rotator approximation transitions in each ladder will overlap each other and the resulting spectral lines will match those of linear molecule with the rotational constant B .

If a transition dipole moment is perpendicular to the symmetry axis, its interaction with the electromagnetic provides torque around this axis, leading to

$$\Delta K = \pm 1 \text{ and } \Delta J = 0, \pm 1.$$

The spacing between two adjacent ladders, K and $K + 1$, is $(A - B)(2K + 1)$ that gives rise to a series of rotational progressions spaced by $2(A - B)$, so called K -structure. The scheme of allowed transitions for the prolate top is shown on Figure 3.

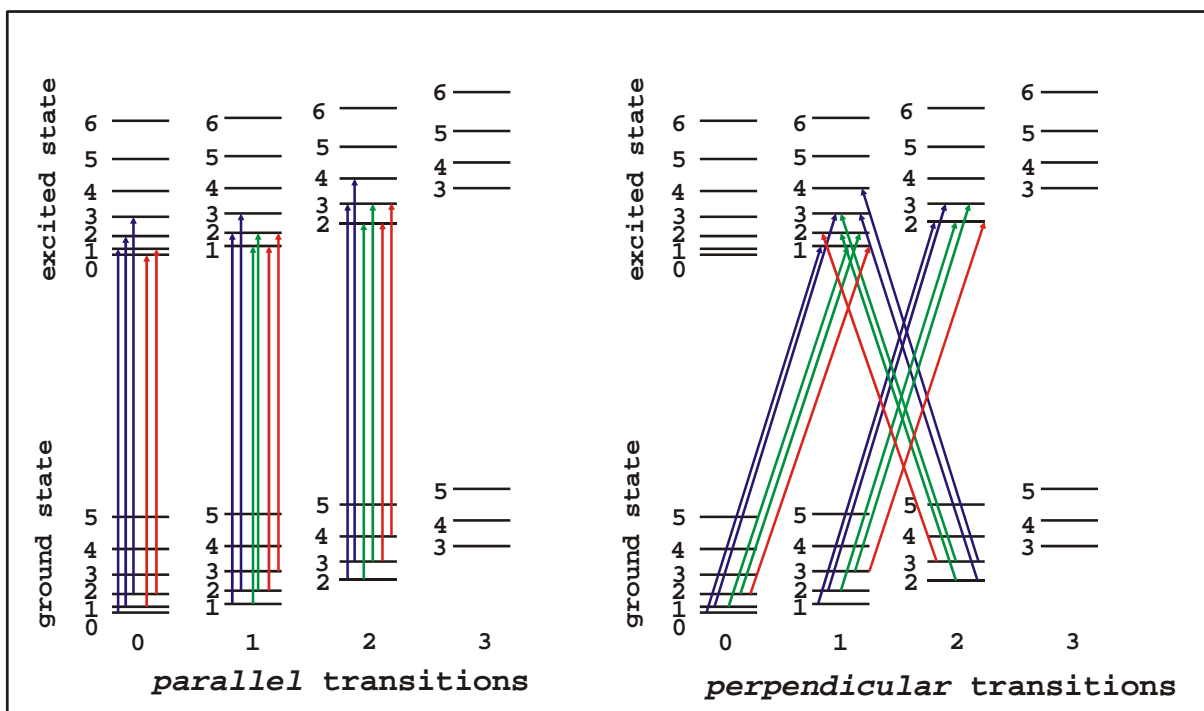


Figure 3. A scheme of allowed transitions for prolate rotor. R-, Q- and P-branch transitions are marked with different colors.

Asymmetric tops

The majority of polyatomic molecules fall in the asymmetric-top category. When the three principal moments of inertia of a molecule differ, the molecule is classified as an asymmetric top. The energy level formulation for a rigid asymmetric top is considerably more complex than that for symmetric-tops or linear molecules. With the exception of low rotational levels, the rotational energy and transitions cannot be conveniently expressed in simple algebraic terms. Nonetheless, it is quite often that the moments of inertia about two axes are close in value and can be assumed to be a symmetric top rotor to a first order, with its levels split to remove the remaining degeneracy. Each level of the rotational quantum number J of an asymmetric rotor are split into $2J+1$ levels which are specified by the quantum numbers K_a and K_c . The value K_a represents the projection of the angular momentum on the symmetry axis if the molecule was a prolate symmetric top rotor and the value K_c corresponds to the limiting case for an oblate symmetric-top. In this way, the levels of an asymmetric rotor are labeled as $J_{K_a K_c}$.

Ray's asymmetry parameter, κ , is often used to characterize the degree of asymmetry:

$$\kappa = \frac{2B - A - C}{A - C}$$

When $A \approx B$, κ approaches +1 for the *oblate* case and when $B \approx C$, κ approaches -1 for the *prolate* case.

For asymmetric tops the rotational transitions can be classified as a-type, b-type and c-type depending upon the orientation of the electronic transition dipole moment to one of the rotational axes. For an asymmetric rotor the selection rules for *a*-type transitions are:

$$\Delta J = 0, \pm 1; \quad \Delta K_a = 0, \pm 2, \dots; \quad \Delta K_c = \pm 1, \pm 3, \dots;$$

for *b*-type transitions:

$$\Delta J = 0, \pm 1; \quad \Delta K_a = \pm 1, \pm 3, \dots; \quad \Delta K_c = \pm 1, \pm 3, \dots;$$

for *c*-type transitions:

$$\Delta J = 0, \pm 1; \quad \Delta K_a = \pm 1, \pm 3, \dots; \quad \Delta K_c = 0, \pm 2, \dots;$$

The situation can get even worse as electronic transitions are not always polarized neatly along the inertial axes. This can lead to hybrid band structures.

CHAPTER 3. HISTORY AND PRINCIPLES OF MASS-SPECTROMETRY

Mass spectrometry makes use of forces that affect charged species placed in electric and/or magnetic field to separate these species. The motion of charged particles is described by the second Newton Law and the Lorentz Law:

$$\mathbf{F} = m \cdot \mathbf{a}$$

$$\mathbf{F} = z(\mathbf{E} + \mathbf{v} \times \mathbf{B})$$

Here F is the force acting on a particle, m is its mass, a – acceleration, z – charge of the particle, E – electric field, $\mathbf{v} \times \mathbf{B}$ – vector product of the particle's velocity and the applied magnetic field. The scalar values are given in italic and vectors – in bold. It can be noticed that separation of particles will depend on their *mass to charge ratio* (m/z).

The pioneer of mass-spectrometry is Sir Joseph John Thomson. He has shown that cathode rays produced by Crooke's tube exhibit a single m/z and must be composed of a single type of negatively charged particle. Comparing this to the charge of ions that was known from experiments on electrolysis, he concluded that the mass of this particle should be 1800 times smaller than the mass of the hydrogen ion. The particle was called *electron* and J.J. Thomson was awarded a Nobel Prize in 1906 for this discovery. Applying the same technique for studying anode rays he observed many kinds of particles [24]

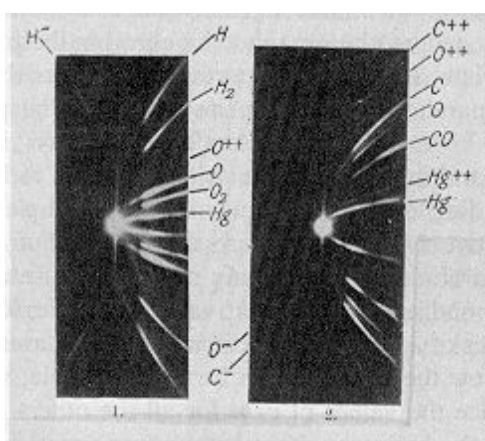


Figure 4. Photographs made by the positive rays after they have suffered electric and magnetic deflections [24].

Now, when the possibility of ions separation was shown, the research efforts were aimed at the creation of a compact mass analyzer with high selectivity suitable for the laboratory use. The first mass spectrometers were built analogous to optical spectrometers known at that time. They incorporated magnetic sector as a monochromator with the magnetic field oriented perpendicularly to the direction of the ionic flux [25]. Ions with different m/z ratios move in this field in arcs of different radii. The second electric sector was used to discriminate the kinetic energy of moving ions. Mass-spectrometers of this kind are still in use because they achieve the highest mass resolution amongst different types of mass spectrometers and because they provide highly reproducible results allowing quantitative analysis. However, high cost of these machines and their bulk stimulated search for new schemes of mass-selection. In 1950s Wiley and McLaren developed time-of-flight (TOF) mass spectrometer that separates ions not in space but in their travel time from accelerating electrodes to detector [26]. Ions accelerating in the electric field will have the kinetic energy

$$T = z \cdot V = \frac{mv^2}{2},$$

where V is the potential between accelerating electrodes. The resulting speed of ions will again depend on the m/z ratio. Assuming that all ions start from the same point and at the same time, the flight time for the analyzer of length L will be represented by the following expression

$$t = \frac{L}{v} = L \sqrt{\frac{m}{2zV}}.$$

Mass scan is achieved by observing the time dependence of the signal coming from the ions detector. This makes TOF mass spectrometers to be the fastest mass analyzers available with the highest mass range. TOF mass spectrometers are best suited for pulsed ion sources. However the mass scale is relative and depends on experimental parameters and the spectrometer has to be calibrated every time using some known reference peaks. The mass resolution of TOF mass spectrometers $m/\Delta m$ normally does not exceed 300-400 and their demand to high vacuum in the TOF tube (around 10^{-7} mbar) complicates using such spectrometers for monitoring plasma of slit nozzles that are running at the pressure around 0.1 mbar.

Next step of the progress in mass spectrometry was made by Wolfgang Paul who discovered in 1950s that electromagnetic field of quadrupole can be used to focus ions [27].

Constant electric field would focus ions in one plane and defocus in another, but alternating field can focus ions in both planes.

Quadrupole mass filter consists of four equally spaced high-precision cylindrical rods placed parallel to each other. Opposite rods of the filter are connected and form positive and negative pairs that are subject to constant and alternate potential (Figure 5).

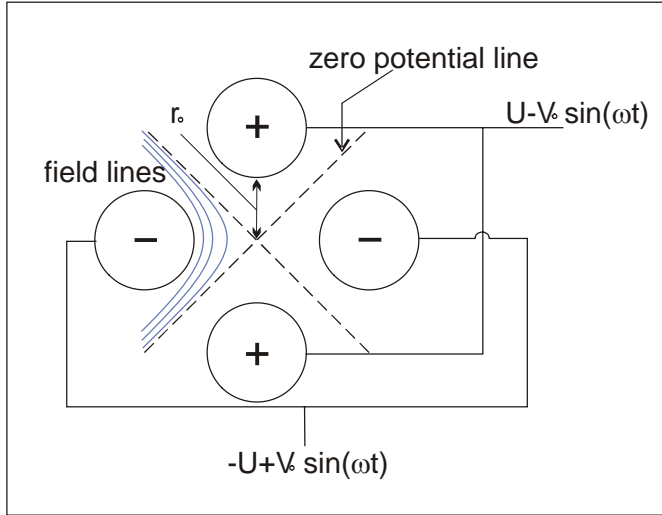


Figure 5. The scheme of the quadrupole mass filter.

The motion of ions in quadrupole field is described as a solution of a system of linear second order differential equations. Such equations were studied for the first time in 1868 by Mathieu [28] and are named after him. When applied to the motion of ions, these equations can be written in the following form:

$$\frac{d^2x}{dt^2} + \frac{\omega^2}{4}(a + 2q \cos \omega t)x = 0$$

$$\frac{d^2y}{dt^2} - \frac{\omega^2}{4}(a + 2q \cos \omega t)y = 0$$

$$\frac{d^2z}{dt^2} = 0$$

$$a = \frac{4zU}{m\omega^2 r_0^2}$$

$$q = \frac{2zV}{m\omega^2 r_0^2}$$

Mathieu equations have two types of solutions:

Stable motion: ions oscillate in the xy -plane with finite amplitude and pass quadrupole along z -axis without hitting the rods.

Instable motion: the amplitude of oscillation increases exponentially in x , y or both directions and eventually ion hits a rod.

The type of the solution depends only on parameters a and q and does not depend on the initial parameters of the ionic motion such as the speed of ion. Thus, in the a - q space there are stability and instability regions. The region of interest is the intersection of x - and y -stability regions shown on Figure 6 [28].

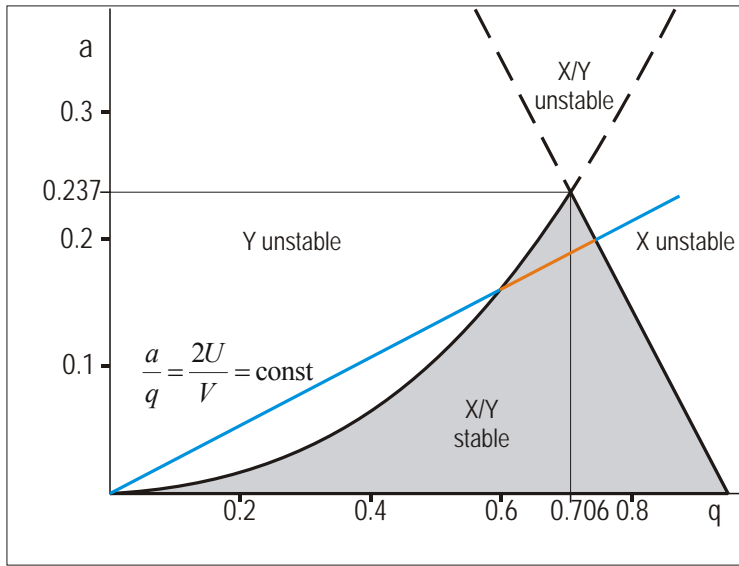


Figure 6. The stability diagram of the solutions of Mathieu equations.

For specified values of r_0 , ω , U and V all ions with the same m/z ratio correspond to the same point on the stability diagram. As the ratio $\frac{a}{q} = \frac{2U}{V}$ does not depend on m , all points corresponding to different ion masses will be situated on the working line $a/q = \text{const}$. Points lying on the q -axis ($a=0$, i.e. $U=0$) will be stable for $0 < q < q_{\text{max}} = 0.92$ which means that all ions with masses in the range of $\infty > m > m_{\text{min}}$ will have stable trajectories. In this case quadrupole will serve as an ion guide focusing all heavy enough ions.

The range of transmitted ion masses Δm becomes narrower with the increase of the voltage U , i.e. with the increase of the slope of the working line, and reaches its zero value when the line crosses the top of the stability region. In this case ion transmission is determined only by fluctuations of the electromagnetic field. Changing the values of U and V simultaneously and proportionally keeping the a/q ratio constant will bring ions of different masses inside the stability region making quadrupole work as a mass-spectrometer.

Because of their versatility and simplicity, quadrupole mass-filters became common in very different research fields, from organic and biochemistry to the molecular physics, being used as mass-spectrometers or as ion guides.

CHAPTER 4. EXPERIMENTAL SETUP

Ions and radicals, studied in this work, were produced in a pulsed discharge slit nozzle using acetylene diluted in helium or argon. The plasma source was mounted on a translation stage so that the distance from the nozzle opening to the probe laser beam could be varied in the range of 0–16 mm. The nozzle was placed in the stainless steel crosspiece evacuated by Roots pump system with total pumping capacity of 2775 m³/h that maintained the background pressure of 10⁻² mbar. During the experiment the pressure in the chamber is kept at a chosen value (normally, 0.060 – 0.200 mbar) by automatical adjustment of the valve opening time. It has been found [29] that this procedure significantly increases the stability of the production of transient species. Mirrors for CRD experiment were mounted to the chamber with flexible bellows tube that allowed fine adjustment of each mirror in order to create stable optical resonator. The plano-concave mirrors used in the experiment were produced by Research Electro-Optics Inc. and had a reflecting surface of 5 mm radius, 1000 mm curvature radius and a reflectivity of 99.98 to 99.998 %. Installed at a distance of 52 cm from each other they form a stable optical resonator with a spacing of longitudinal modes of about 0.008 cm⁻¹ so that for a laser with a bandwidth of 0.05 cm⁻¹ a multimodal cavity excitation is always allowed, reducing interference effects in cavity to the minimum. A small helium flow near the surface of mirrors protects them from being contaminated by plasma products. The vacuum in the chamber is ensured by sealed 1" quartz windows.

Absorption spectroscopy of atoms and molecules in the gas phase is a powerful tool of analytic and physical chemistry that allows one to determine absolute concentrations and record absorption spectra of diverse species. The ability to measure absolute concentration is the reason why absorption spectroscopy is still used although such elaborated methods as resonance enhanced multiphoton ionization (REMPI) and laser-induced fluorescence (LIF) are available. Amongst absolute methods a cavity ringdown spectroscopy (CRDS) is of special importance as it combines good sensitivity and relatively simple experimental setup.

Regular absorption spectroscopy measures the amount of light that is transmitted through the sample. The drawback of the method is the limited sensitivity as a small variation of optical density has to be measured on top of a big amount of light passing through the sample. The sensitivity can be increased by extending the absorption path or by frequency modulation schemes. The CRDS is based on measuring not the magnitude but rather the speed

of light decay. The sample is placed inside an optical resonator that consists of two highly reflective mirrors so that the light that enters the resonator reflects back and forth (Figure 7).

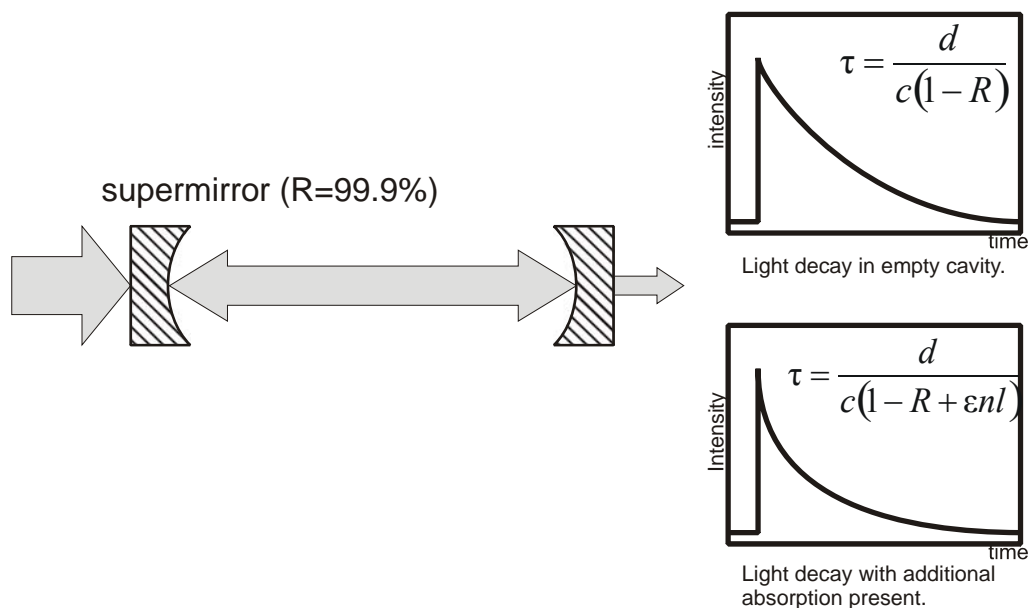


Figure 7. The principle of cavity ringdown spectroscopy.

Every time the light is reflected from a second mirror, the small part of it escapes the resonator and goes to the detector. The stronger sample absorbs the faster light decays. Depending on the reflectivity, the effective path length can be up to several kilometers. The first CRDS measurement was reported in 1988 by O’Keefe and Deacon [30] who showed that using a pulsed laser one can avoid interference effects in the resonator. They demonstrated the sensitivity of the method by recording the spectrum of the doubly forbidden $b^1\Sigma_g^+(\nu = 1,2) \leftarrow X^3\Sigma_g^-(\nu = 0)$ electronic transition of oxygen.

The advantage of CRDS compared to other highly sensitive methods of optical spectroscopy is the absolute scale of the detected signal. This allows quantitative measurements without calibration.

Probe laser beam was shot at 60 Hz frequency whereas the gas valve was running at 30 Hz so for every plasma pulse the background absorption could be subtracted. A tunable dye laser that was used in the experiment is a SCANmate 2E by Lambda Physik with a tunable range of 340..900 nm. For high-quality scans the laser bandwidth of 0.15 cm^{-1} can be reduced to 0.05 cm^{-1} by installing additional intracavity etalon. The dye laser was pumped by an excimer laser (COMPex 110 by Lambda Physik) with a wavelength of 308 nm (Xe+HCl mixture in neon) that generated 10 ns laser pulses with a typical power of 120 mJ.

Laser beam was spatially filtered by 1:1 telescope system with a $100 \mu\text{m}$ pinhole placed at the focal point and guided to the optical resonator. The light that leaked out of the cavity

was detected by a fast photodiode (Hamamatsu S1336-44BQ, spectral response range 190 to 1100 nm, response time 0.5 μ s). Narrow-band optical filter was placed in front of photodiode to block most of the background light and the light generated by the discharge. After amplification, the signal was digitized and fitted to the exponential decay curve by standard routine. Typical decay times ranged from 7 to 50 μ s and depended mainly on the quality of available mirrors. A decay time of 50 μ s corresponds to the effective path length of 860 meters through a plasma jet. Spectra were calibrated using the Burleigh pulsed wavemeter WA-4500 with working range of 400 to 1100 nm and wavelength determination accuracy of 0.02 cm^{-1} . The determined wavelength value was transmitted to the computer via RS-232 protocol and recorded as a separate data channel.

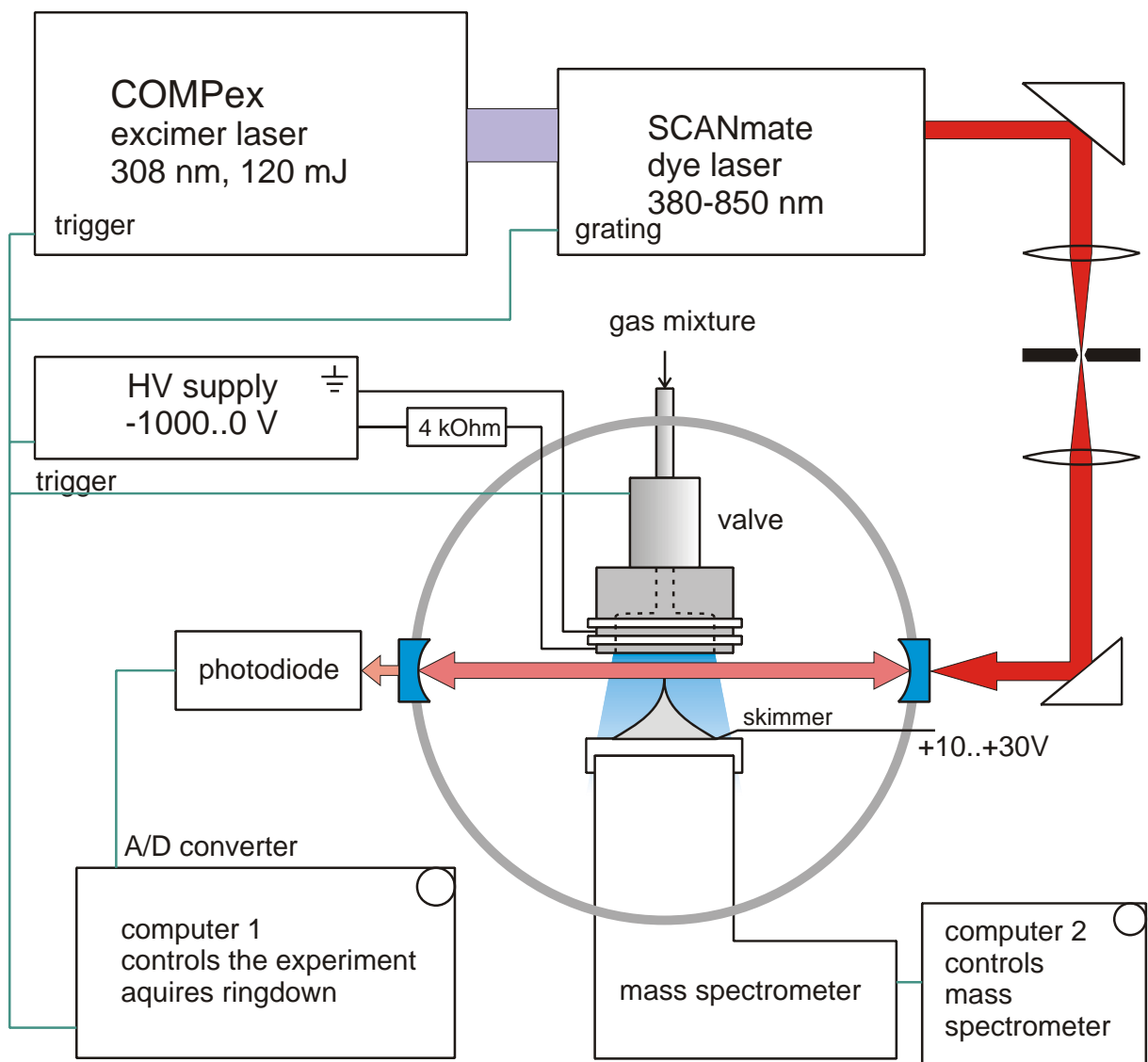


Figure 8. The organization of the experimental setup.

Transient species were produced in plasma that was generated by letting an electrical discharge through the specially prepared gas mixture (normally a dilution of 0.5%–1% of acetylene in helium or argon). The flow of the gas with a stagnation pressure of 10 bar was operated by a solenoid valve (Series 9 valve made by Parker Hannifin Corporation) that formed 1 ms gas pulses at 30 Hz frequency. The expansion nozzle had multilayer geometry: it was formed by slotted ceramic insulators separating the electrodes as shown on Figure 9. The negative voltage of -250 – -1000 V was applied to outer electrodes whereas the inner electrode was grounded. It was shown [31] that a negative potential of outer electrodes to the inner plate is important because of the significant mobility difference of positive and negative charge carriers (molecular ions and electrons) in plasma. The discharge pulse of 250 μ s was synchronized with the maximum opening of the gas valve to produce stable conditions for recording the whole laser ringdown event. The current on the electrodes was monitored by measuring the voltage dropdown on load resistors. The advantage of this scheme is that the discharge is confined in the region prior to the nozzle opening and it will not interfere the molecular cooling in the supersonic expansion. The laser followed the beginning of the discharge so that the total ringdown event was recorded during a single plasma pulse. The measured rotational temperature of produced species was in the range of 25 to 40 K.

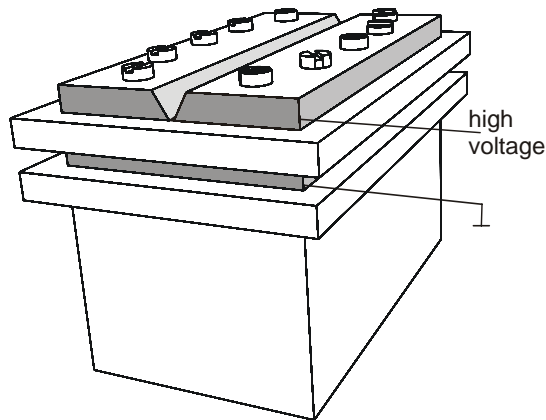


Figure 9. The slit nozzle consists of two blade electrodes, one slotted electrode and aluminum body, separated by slotted ceramic plates.

Described detection scheme does not allow studying molecules selectively. Instead, all species produced in the plasma are observed simultaneously and one has to prove if observed spectral feature belongs to the molecule of interest. In order to facilitate this task the setup was augmented with a mass spectrometer that would sample the plasma downstream to the optical probing region. The spectrometer of choice was Inficon PPM400 by Balzers AG, a quadrupole mass spectrometer specially designed for monitoring the plasma. The main difference compared to standard quadrupole mass spectrometer is a kinetic energy filter for

ions entering the quadrupole. Three electrostatic lenses are used as ion transfer optics as well as energy filter (Figure 10). A divergent ion beam arriving at the first lens is defocused around the beam stop and then focused again into the mass filter. In this way, a bandpass for the ion energy is established. All electrostatic potentials can be biased to adjust the mass spectrometer to ions of particular energy.

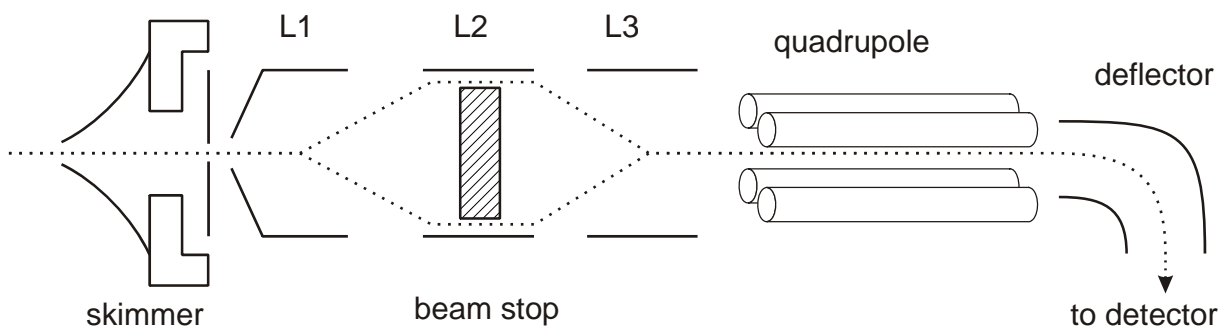


Figure 10. The mass spectrometer, adapted to sample discharge plasma. The kinetic energy filter consists of three electrostatic lenses (L1, L2, L3) and a beam stop that block ions with energy above a threshold. The teflon cap with the skimmer protects mass spectrometer from electromagnetic interference.

Some additional modifications were made to improve the sensitivity of the mass spectrometer by reducing the electromagnetic noise on the detector arising from the discharge. The extraction hood of the spectrometer (that has an entry orifice of 100 μm) was covered with a teflon cap that has an aerodynamic skimmer on top of it. With this small adaptation the electromagnetic noise from the discharge has been reduced virtually to zero allowing clean scans to be recorded up to the ion masses of 200 a.m.u. A small positive potential (+10 to +30V) was applied to the skimmer to get the maximum current of ions. Ions were detected by a conversion dynode that was run in the single ion counting mode. Typical detected amounts of ions were 10 to 10^4 ions per ms.

For the discharge length of 250 μs running at 30 Hz the ions are produced only during $250 \cdot 10^{-6} \text{ s} \times 30 \text{ Hz} = 7.5 \cdot 10^{-3} = 0.75\%$ of the time. The PPM400 mass spectrometer and its bundled software, designed for continuous ions detection, do not support gated ion detection so a special counting scheme was built. The ion count signal from the secondary electron multiplier with conversion dynode was converted to the TTL pulse form and then registered by a National Instruments PCI-6602 eight-channel counter board. One channel was used to form a gate pulse that was triggered by the discharge trigger. This gate pulse was used to open the second, counting channel for a time interval when ions are expected to arrive to the detector. For the nitrogen plasma it was determined that first N_2^+ ions arrive to the detector 50 μs after the discharge is ignited and expire 100 μs after the end of the discharge (the time

period when the ion current exceeds 20% of its peak signal). A program was written in LabView™ 5.1 that controlled the quadrupole mass spectrometer via RS-232 interface [32], operated the PCI-6602 counter using the driver provided by National Instruments, displayed recorded mass spectra and stored them to hard disk (see the Appendix B for the program transcript). The time sequence of running experiment is shown on Figure 11.

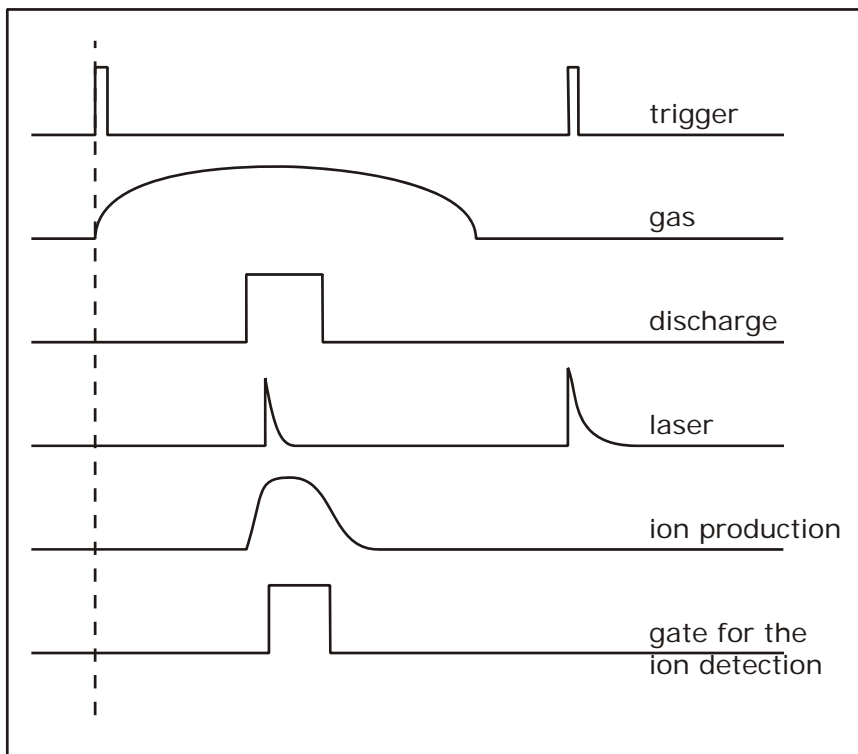


Figure 11. The time sequence of the experiment. Trigger sequence runs at 60 Hz, every second ringdown event is used for subtraction of background absorption.

CHAPTER 5. SAMPLING DISCHARGE PLASMA WITH QUADRUPOLE MASS SPECTROMETER

Introduction

Methods that combine an electrical discharge and a supersonic expansion are commonly used for producing different kinds of transient species [31, 33]. Particularly, it was shown [34] that linear carbon chains could be produced in a slit nozzle through an electrical discharge of a precursor gas. Although there exist some models of the chemistry that takes place inside such plasmas [35], it is nearly impossible to take into account all factors that influence the plasma conditions. Hence, the characterization of the chemical compound of plasma can only come through the experimental observations. This can be either an indirect spectroscopic measurement or a direct sampling the plasma with mass spectrometer.

The two most common techniques to measure ions are quadrupole and time-of-flight (TOF) mass spectrometry. Intrinsic pulsed character of TOF instrument makes it more appropriate for monitoring the discrete ion flow from the pulsed plasma source. However, for slit nozzles with profuse gas flux it is impossible to achieve required high vacuum conditions without installing differential pumping system. On the contrary, quadrupole mass spectrometer of decent resolution is inexpensive and compact and it can be built into the existing experimental setup without its substantial modification.

Because of the continuous character of the quadrupole mass spectrometer one has to modify the detection scheme and use the gated integration of the signal.

Results and discussion

The mixture of acetylene in helium is a commonly used precursor for producing carbon-containing radicals and ions. The mass spectrum of its plasma produced in the pulsed discharge nozzle has been obtained recently [36] using TOF mass spectrometer so it would be particularly interesting to compare obtained mass spectra and to justify the applicability of the constructed setup to monitor pulsed plasma sources. Figure 12 presents the mass spectrum of the acetylene mixture in helium recorded in steps of 0.1 mass unit with the accumulation of the ion current during 1000 ms for each data point.

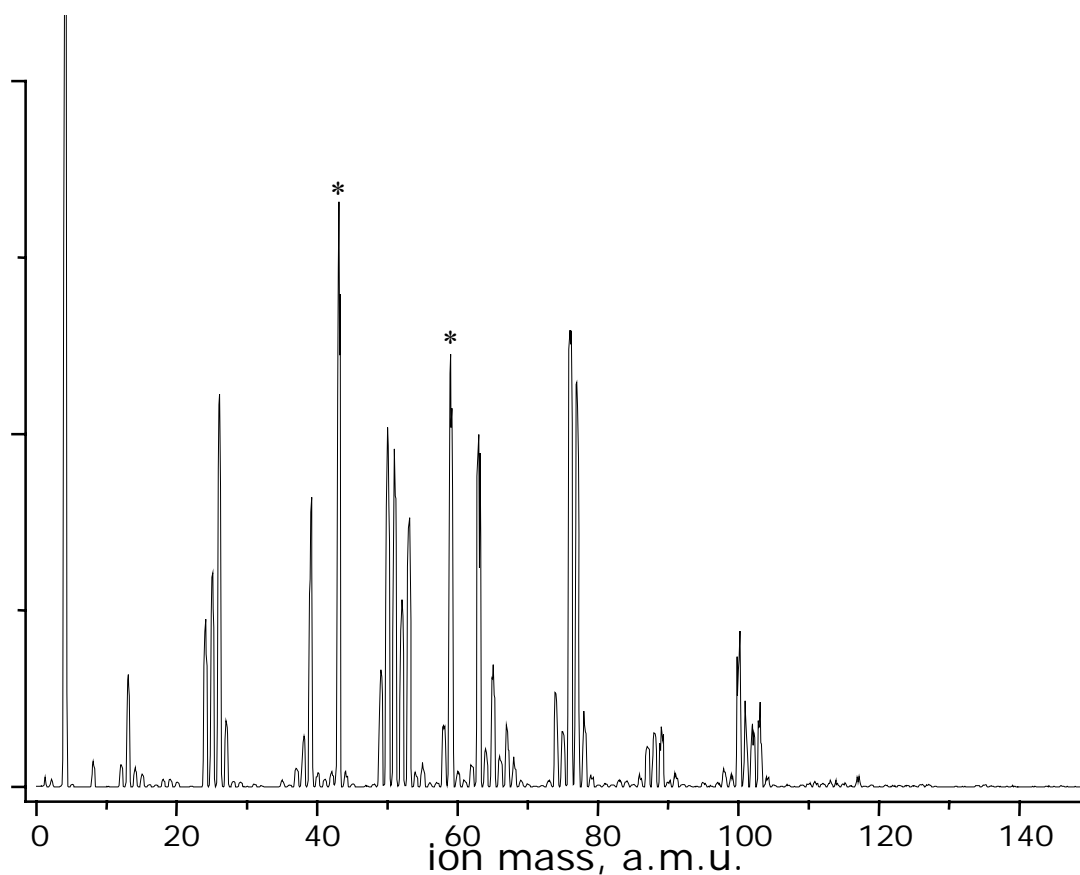


Figure 12. The mass spectrum of 0.5% C_2H_2 in helium discharge. Peaks at masses 58 and 43, marked with asterisks, are characteristic marks of acetone, $(CH_3)_2CO^+$ and its fragment CH_3CO^+ , respectively.

One can see that mass peaks are arranged in the series of groups, where each group corresponds to ions with certain number of carbon atoms (C_nH_m). The series with even n are more intense with a strongest peak corresponding to $C_nH_2^+$. The most prominent structure of these ions are polyacetylene cations that are readily observed in this kind of plasma [37-39]. The mass spectrum confirms that linear carbon chains are the dominating products in the acetylenic discharge. Nevertheless, significant number of ions, especially those with odd n , have three or four hydrogen atoms. These ions probably have prolate structure analogous to the structure of $C_6H_4^+$, which has been identified in such plasma under similar conditions using optical cavity ringdown spectroscopy [40]. Compared to the TOF mass spectrum [36], the spectral resolution has clearly increased so that peaks of ions with adjacent masses are clearly separated. Higher spectral resolution also makes weaker peaks visible, providing more information about the plasma ionic composition. Thus, quadrupole mass spectrometer, equipped with a kinetic energy filter, is an appropriate tool to monitor the ionic composition

of plasma in pulsed discharge nozzles, that can compete and even overcome TOF mass spectrometers.

The carrier gas has a great influence on the production of transient species. The difference in the plasma composition can be visualized by recording mass spectra of acetylene dilutions in different carrier gases. Compared to helium, argon as a carrier gas obviously promotes the aggregation of acetylene fragments into longer chains (Figure 13). One can clearly distinguish mass peaks of $C_{12}H_2^+$ and $C_{12}H_3^+$. Once again, mass peaks of polyacetylene cations dominate the spectrum.

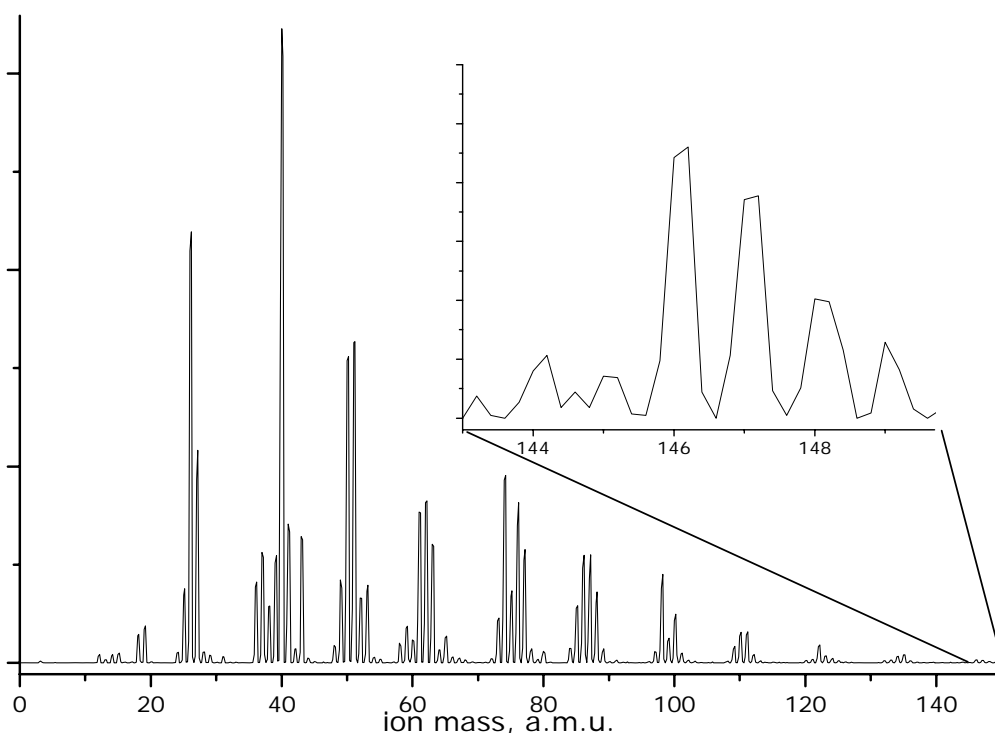


Figure 13. The mass spectrum of 0.5% C_2H_2 in argon discharge. Part of the spectrum is magnified to illustrate the resolution and the sensitivity of the setup.

The discharge through the mixture of acetylene in neon shows a remarkably richer mass spectrum (Figure 14). Not only longer chains are observed in this plasma but also the species distribution is much richer because of the species containing more hydrogen atoms. The inset shows that on average in neon plasma carbon chains have one hydrogen atom more than in argon. This makes neon an attractive carrier gas for studying nonlinear carbon chains having three or four hydrogen atoms. Due to its costliness, however, it can only be used in the exceptional cases, when conventional carrier gases do not provide sufficient concentration of a species of interest.

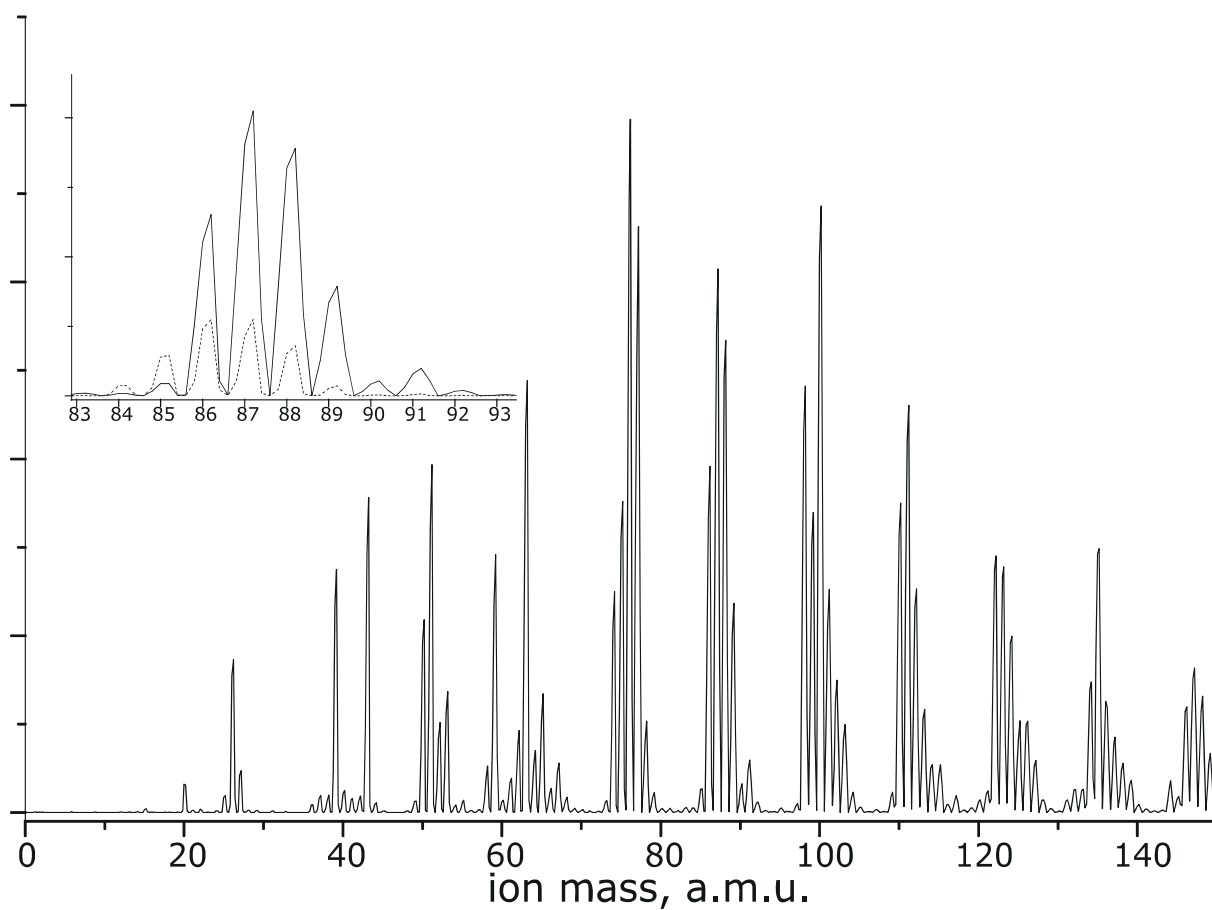


Figure 14. The mass spectrum of 0.5% C₂H₂ in neon discharge. The inset shows the comparison of species distribution in neon (solid line) and argon (dotted line) plasma mass spectra recorded under similar conditions.

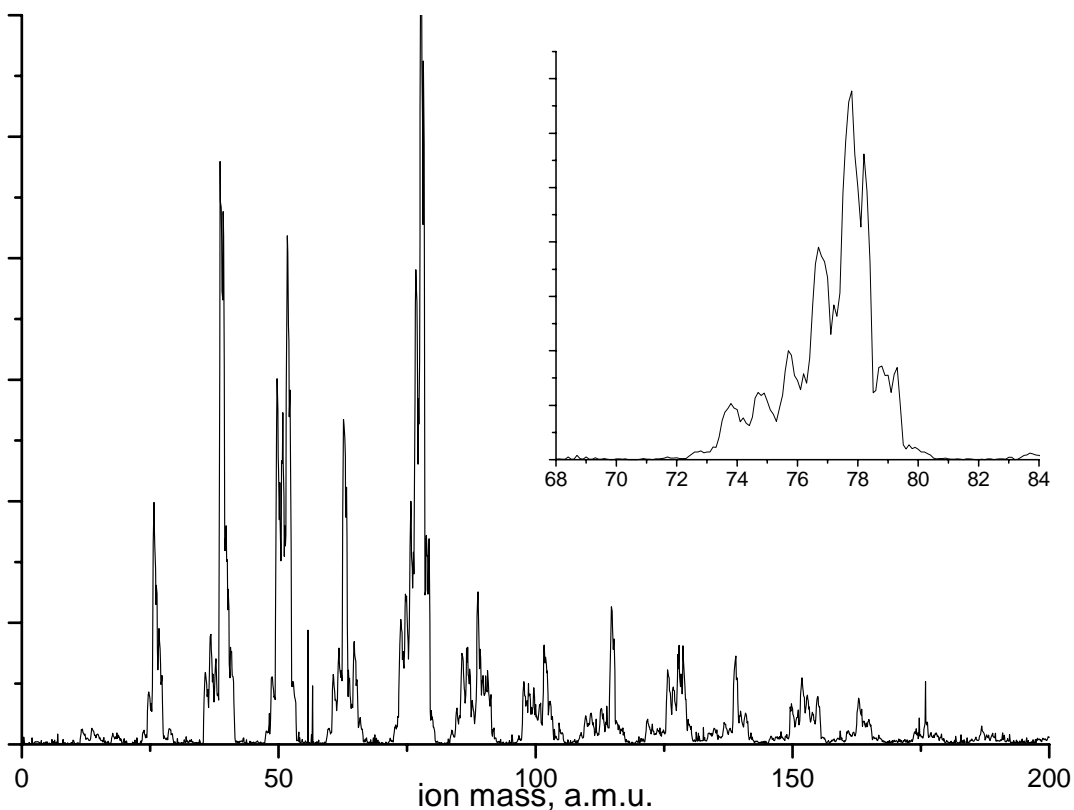


Figure 15. Mass spectrum of 0.3% benzene in argon discharge plasma. The inset shows mass distribution of ions with six carbon atoms.

Benzene is another possible precursor for producing radicals and ions in the gas phase. Although the concentration of benzene in plasma is limited by its vapor pressure, some absorption features are only observed with this precursor, for example, broad band at 442.9 nm [41]. The peculiarity of the species distribution in the plasma can be depicted by the observed mass spectrum (Figure 15) that was recorded for the 0.3% benzene in argon mixture. As it was discussed, the acetylene plasma consists primarily of chain structures containing only a few hydrogen atoms. At the same time, various fragments of benzene can constitute wider variety of structures although hydrogen-deficient structures still dominate. On the contrary to previous assumptions [41], benzene fragments do react with each other producing ions of masses up to 178 a.m.u. (which is probably due to anthracene cation $C_{14}H_{10}^+$). However, because a lot of different species are generated in the discharge simultaneously at comparable concentrations, it would be hardly possible to assign them in the cavity ringdown spectrum. Even the assignment of the band at 442.9 nm is disputable as it was made assuming that no species with more than six carbon atoms can be produced in benzene plasma [42].

Mass spectrometry of sulfur-containing carbon plasma

Although $C_2H_2+CS_2/Ar$ plasma is commonly used to produce sulfur-terminated carbon chains, its composition has not been extensively studied. Such discharges have been utilized to produce laser induced fluorescence spectra of the transient species $HC_{2n}S$ ($n = 1-3$) and the $SCCS^-$ anion [43-45], and pure rotational spectra of HC_nS ($n = 2-8$) [46, 47] and C_nS ($n = 4 - 9$) [48]. Despite the importance of this discharge system for the production of sulfur bearing species relevant to astrophysics, it has never been studied by a mass-selective technique. In this work the plasma was sampled using commercial quadrupole mass spectrometer. Only a small amount of C_2H_2 was added to the mixture of 0.3% CS_2 in argon to favour the production of sulfur-containing species and highlight corresponding peaks in the mass spectrum. High discharge stability allowed the detection of cationic chains of different type containing up to 7 carbon atoms. The structure of these species has not been unambiguously identified but based upon optical observations these are unsaturated linear and nearly-linear carbon chains terminated with sulfur and hydrogen atoms.

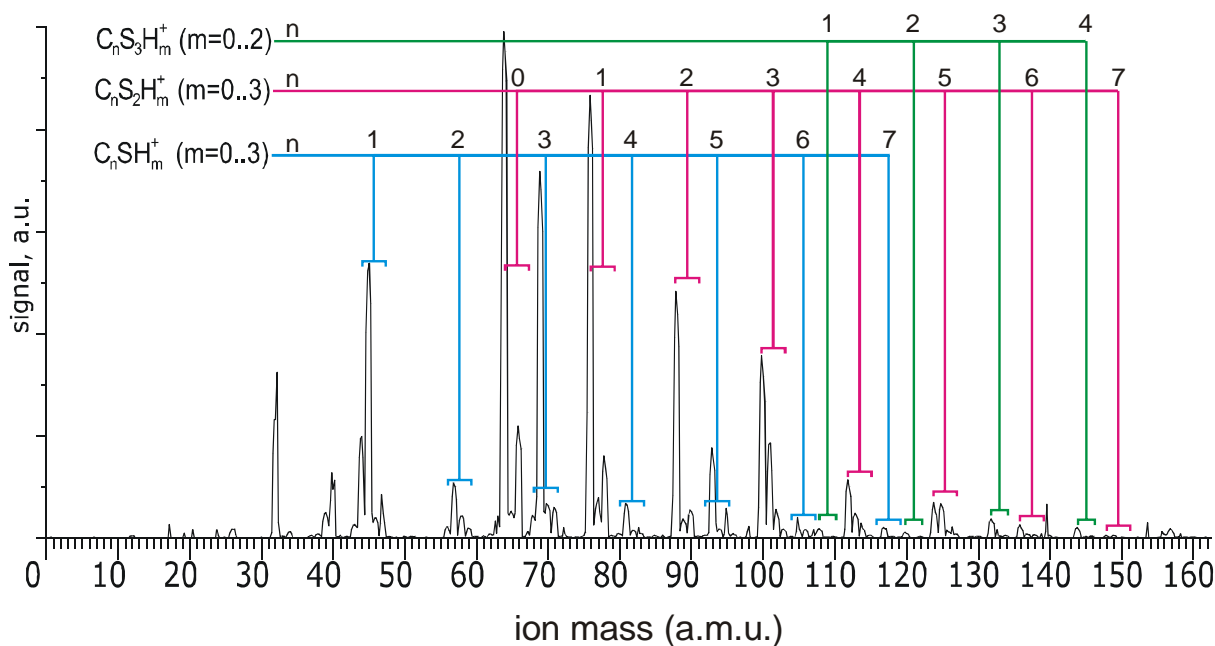


Figure 16. The mass spectrum of CS_2 mixture in argon with trace amounts of acetylene. Vertical bars mark different homologous series.

Conclusions

The designed scheme of gated ion detection using quadrupole mass spectrometer shows high resolution and signal-to-noise ratio, that outperforms the reported observation of the

pulsed discharge nozzle plasma using time-of-flight mass spectrometer [36]. Presented scheme can be used for monitoring pulsed discharge supersonic ion sources with any typical gas precursor that is used with the present experimental setup. Obtained results indicate that linear carbon chains are dominating species in the acetylenic discharge. Evidence of the formation of PAH cations in benzene plasma are observed. Mass spectra demonstrate significant differences in the plasma compound depending on the carrier gas.

CHAPTER 6. SPECTROSCOPY OF SULFUR-TERMINATED CARBON CHAINS IN THE GAS PHASE

Introduction

Sulfur-bearing conjugated carbon systems are of interest to many fields of scientific enquiry ranging from molecular electronics to astrophysics. As molecular electronic devices they are invoked due to the propensity of the sulfur terminal to bond to a gold surface [49]. Single sulfur-bearing conjugated molecules have been placed between gold electrodes with voltages applied between them, thereby allowing the measurement of current passing through a single molecule [50]. The current-voltage characteristics observed depends critically upon the electronic structure of the bridging sulfur-bearing conjugated carbon system [51]. It is known that sulfur plays an important part in the chemistry of the interstellar medium [9]. Sulfur bearing carbon chains such as C_3S and C_5S have been discovered in space by rotational spectroscopy [52-54]. Sulfur heteroatoms terminating carbon chains cause strong polarization of the π -electron cloud and increases the oscillator strength of its electronic transitions. As such, despite the lower abundance of sulfur in the interstellar medium as compared to carbon, the sulfur terminated carbon chains can absorb strongly and may be considered as candidate carriers of the diffuse interstellar bands. Confirmation as carriers of diffuse interstellar bands can only come from a direct comparison with gas-phase optical laboratory spectra. As sulfur-bearing carbon chains such as C_nS and HC_nS are radicals, they must be produced as transient species. This is usually performed with a sulfur-seeded hydrocarbon discharge.

Results and discussion

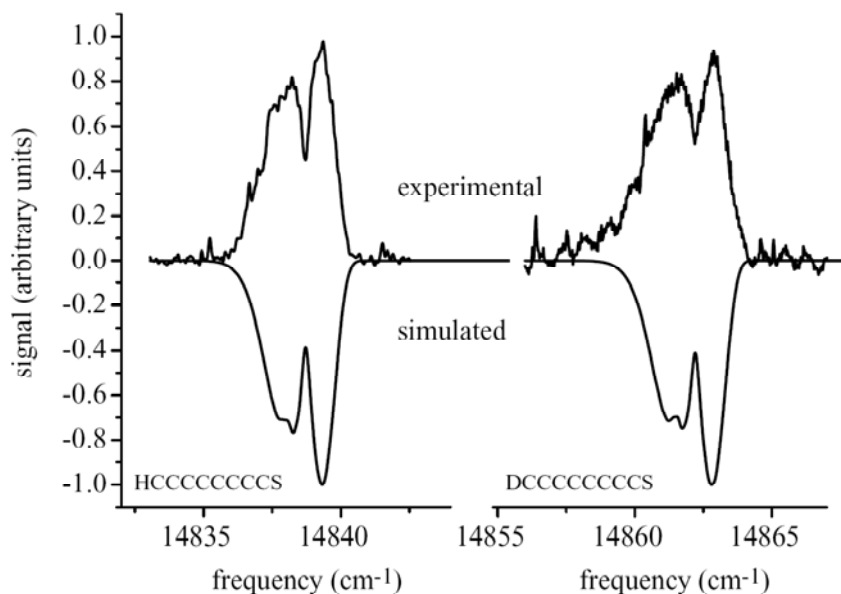


Figure 17 The origin band of HC₈S (left) and DC₈S (right) measured by CRDS. The origin of HC₈S lies 80 cm⁻¹ to the blue of the prediction in Ref. 5, based on a linear relationship of the absorption wavelength and chain length. Simulations were performed using the spectroscopic constants listed in Table 3.

For production of HC₈S (DC₈S) a 0.5% C₂H₂ (and/or C₂D₂) with 0.1% CS₂ mixture in argon was used while for production of HC₁₀S (DC₁₀S), C₂H₂ was substituted by 0.4% C₄H₂ (and/or C₄D₂). Figure 17 shows the measured origin bands of HC₈S and DC₈S measured by CRDS.

The origin position of HC₈S, 14838.4 cm⁻¹, is only 80 cm⁻¹ to the blue of that predicted by a linear relationship between chain length and origin wavelength, extrapolated from the smaller species, HC₂S, HC₄S, and HC₆S [43, 44]. The slight deviation from linearity is continued for HC₁₀S and its deuterated analog, DC₁₀S. The broad spectra of these species are shown in Figure 18. The origin positions of HC₁₀S and DC₁₀S cannot be estimated better than the laser resolution (0.15 cm⁻¹) due to the severe lifetime broadening. Spectroscopic constants for HC₈S, DC₈S, HC₁₀S and DC₁₀S are summarized in Table 3.

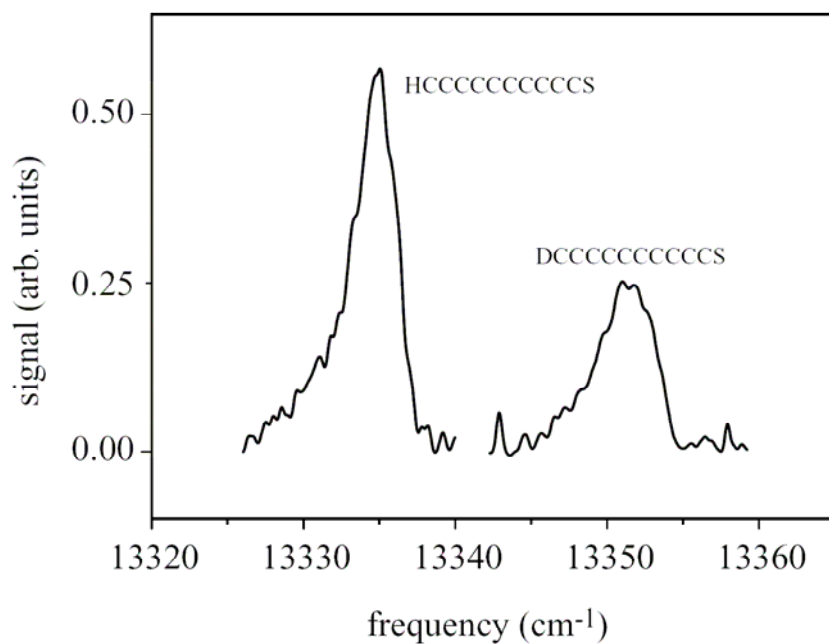


Figure 18. Origin bands of HC₁₀S (left) and DC₁₀S (right) measured by CRDS. From the broadening of the bands the excited state lifetime is estimated to be about 2.6 ps.

The strongly linear relationship between absorption wavelength and chain size is a reflection of the cumulenic bonding structure in the HC_{*n*}S species induced by the carbon-sulfur double bond. The bonding pattern was confirmed by the quantum chemical calculations described above. This relationship is also seen in the C_{*n*}H⁻ anions [55], where one end of the chain exhibits cumulenic bonding which merges smoothly to acetylenic character on moving to the terminal hydrogen. It is this acetylenic character, induced at the hydrogen terminal, which explains (at the Hückel level of theory) the deviation from linearity. It has been shown that for the long carbon chains, HC_{2*n*}H, the relationship between chain length and absorption wavelength is strongly non-linear [56]. As the near-linear relationship is expected to continue, a prediction can be made for the origin position of HC₁₂S. Based on the present data (making a small correction due to non-linearity), this species is expected to absorb at 820±5 nm (Figure 19).

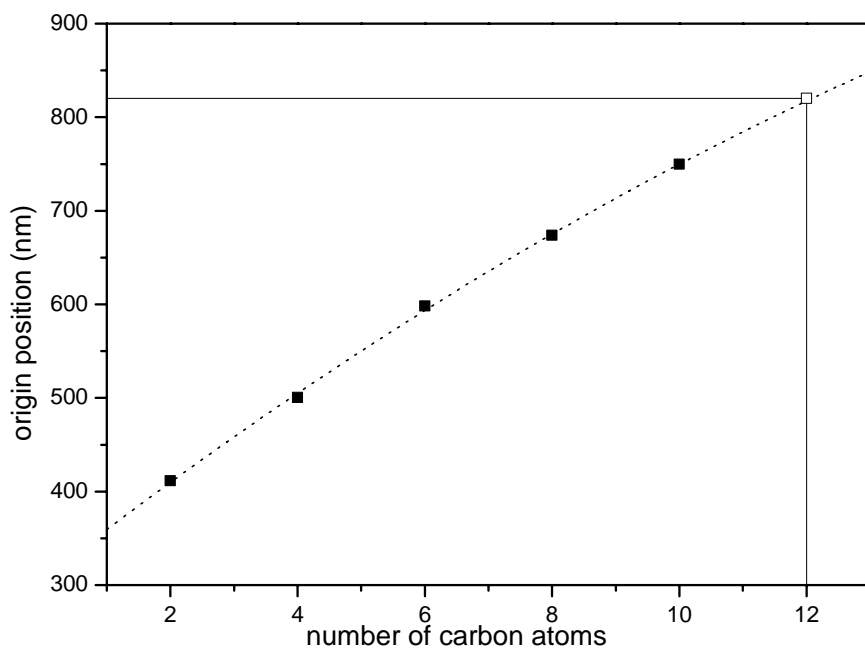


Figure 19. A plot of the origin band wavelength of the HC_{2n}S series as a function of the number of carbon atoms in the chain, $2n$. The relationship is remarkably linear, a reflection of the cumulenic bonding in these systems. A quadratic fit to the points measured for $n = 2\text{--}5$ yields an estimate for the absorption position of HC_{12}S of 820 nm.

The shift in origin band position upon deuterium substitution is caused by the difference in zero-point energies in the ground and excited states. This is 23 cm^{-1} to higher energies for HC_8S and 17 cm^{-1} for HC_{10}S . This compares with 35 cm^{-1} for HC_6S and 54 cm^{-1} for HC_4S . The decreasing deuterium shift upon increasing the chain size reflects the decreasing effect that the electronic excitation has on the vibrational modes involving motion of the hydrogen (deuterium) moiety. With this in mind, it is expected that the origin band position of DC_{12}S will lie about 12 cm^{-1} to the blue of the HC_{12}S band position. It has been noted that the excited state lifetimes of the HC_{2n}S series decrease with increasing chain length. Laser induced fluorescence work has estimated the lifetimes of HC_4S and HC_6S to be 30 ns and 270 ps respectively [43, 44]. The lifetime of HC_8S is thus expected to be shorter still. Due to lack of resolution, the lifetime could not be estimated from the spectrum displayed in Figure 17. The line width used in the simulated spectra was 0.15 cm^{-1} . If the lifetime broadening is no more than this order of magnitude, a conservative lower limit for the lifetime can be made of 70 ps. From spectral simulation, the lifetime of the $\text{A}^2\Pi$ excited state of HC_{10}S is estimated to be 2.6 ps.

Table 3. The origins and the effective rotational constants (in cm^{-1}) of the vibronic bands of the HC_8S and HC_{10}S radicals, and their deuterated analogs.

	T_0	B''	B'	ΔA_{SO}
HC_8S	14838.4(1)	0.00958 ^a	0.00954(2) ^d	0.7
DC_8S	14861.9(1)	0.00938(2) ^b	0.00935(3) ^d	0.7
HC_{10}S	13333.7(5)	0.00551(1) ^c	0.00542(5) ^d	2.5
DC_{10}S	13350.8(8)	0.00541(1) ^{b,c}	0.00535(5) ^d	2.5

Only the change in ASO could be determined accurately by the fitting procedure. *a*). Previously determined by microwave spectroscopy [46]. *b*). The rotational constants of the deuterated species in the ground state were calculated according to the assumption that the structure of deuterated species is unchanged upon isotopic substitution. *c*). The rotational constant of HC_{10}S in the ground state was estimated under consideration of increasing chain length. *d*). Rotational constants in the excited state were extrapolated using the rotational constant ratio B''/B' of HC_6S and HC_4S . Reported errors were estimated during the fitting procedure.

Conclusions

By quadrupole mass spectrometry it was found that a sulfur-seeded hydrocarbon discharge produces a range of hydrogen and sulfur bearing carbon chains, and that these species dominate the discharge chemistry. This is in accord with previous detection of sulfur bearing chains as products of CS_2 /hydrocarbon discharges. The dominant series appearing in the mass spectrum are the $\text{C}_{2n+1}\text{SH}_m$ and $\text{C}_n\text{S}_2\text{H}_m$ series. The production of the even chains HC_{2n}S was confirmed by cavity ringdown spectroscopy. The spectrum of HC_8S was measured for the first time and was found to lie within 80 cm^{-1} of the prediction according to an extrapolation from smaller members of the same series [43, 44]. The extremely broad origin band of HC_{10}S was measured for the first time and confirmed the slight deviation from linearity of the relationship between chain size and absorption position. This measurement provided an updated estimate for the position of the HC_{12}S origin band, which is expected near 820 nm. The near linear relationship between the absorption wavelength and the length of the carbon chain is indicative of cumulenenic bonding. None of the spectra of the HC_{2n}S chains match those of the DIBs. The predicted position of the origin band of HC_{12}S does not lie nearby any DIBs and thus these species can be ruled out as carriers thereof.

CHAPTER 7. SPECTROSCOPY OF NONLINEAR CARBON CHAINS

High-resolution electronic spectroscopy of a nonlinear carbon chain radical $C_6H_4^+$

Introduction

In recent years many experimental studies have been reported presenting high-resolution spectra of pure and highly unsaturated carbon chain radicals. Microwave [57], infrared [58], and UV–VIS spectra [59] are available both from matrix and gas-phase studies, all of them having in common that the major part of the observed geometries is linear. Even for very long chains, such as $HC_{22}H$ [56] and $HC_{17}N$ [60], linear structures have been found. Theoretical studies, however, predict for longer chains cyclic structures as well. In the case of C_{13} , for example, theory predicts a cyclic ground-state structure [61], but the experimentally observed IR spectrum is clearly that of a linear chain [62]. A reason for this discrepancy might be simply that the experimental techniques – supersonic jet expansions or matrix deposition experiments – favor the production of linear species, because large-amplitude bending motions (that are necessary to close the ring) are frozen in the production process. A similar situation might apply to the interstellar medium, where many linear carbon chain species already have been identified and the number of cyclic structures is still rather limited [63].

In this work the electronic spectrum of a member of a so far unstudied class of carbon chain radicals is presented: a nonlinear and noncyclic species. The spectrum was observed around 604 nm when scanning for coincidences with diffuse interstellar band features in hydrocarbon plasma. The observed spectrum has a clear rotational and K-type structure. Simulation of the spectrum allows an accurate determination of the molecular constants of the carrier. Study of the partially and completely deuterated species gives information on the number of (equivalent) hydrogen atoms. Final identification becomes possible following semiempirical and ab initio geometry optimizations for a number of species. These indicate that the band at 604 nm is due to the carbon chain cation $C_6H_4^+$ with a nonlinear $HC\equiv C-C\equiv C-CH=CH_2^+$ planar molecular geometry. This is confirmed by the observation of their transition in the absorption spectrum obtained after mass-selective deposition of $C_6H_4^+$ ions generated in a hydrocarbon plasma in a 6 K neon matrix.

Spectroscopic data for species of the form $C_6H_4^{(+)}$ are so far missing. Only a photodissociation study has been reported in which $C_6H_4^+$ was generated following a ring opening reaction in cyanobenzene [64]. In the latter study geometry optimizations are reported using MNDO calculations, which result in a series of equilibrium structures for the cation in which the heat formation of the possible acyclic structures is about 150 kJ mol^{-1} lower than that of benzene-type structures. Among these is a geometry that is confirmed in the present study, a linear noncyclic structure that is very close to the geometry proposed for the neutral species: 1-hexene-3,5-diyne [65].

Results and discussion

The experimental setup has been described in details in the corresponding chapter. Presented absorption spectra were recorded using 0.5% C_2H_2 (or C_2D_2) in helium with a discharge of -300 V , a stagnation pressure of 10 bar and pressure in the vacuum chamber of 0.220 mbar. It is an important fact that the highest absorbance was detected with a minimal voltage applied to the electrodes of the discharge nozzle. Previous results obtained with the same discharge nozzle show that such a behavior is a characteristic of positive ions on the contrary to neutral species that are produced in higher concentrations with the increase of the voltage. A possible explanation of this useful phenomenon is that high negative potential on outer electrodes can prevent positive ions from leaving the discharge area and crossing the probe beam. This speculation is supported by the fact that cations exhibit stronger absorption when probed closer to the nozzle opening.

The obtained gas-phase spectrum of the absorption band around 604 nm is shown on the upper trace of Figure 20. One can see a regular sequence of rotational transitions as well as a progression of sharp R-branch bandheads, known as K-structure. The latter is a characteristic feature of parallel transitions of prolate tops. The spacing of rotational lines in resolved P-branch gives a good estimation to for the value of B'' (C'') (on the first step the molecule is treated as *prolate* top and the values of B and C constants are considered equal). The change in rotational constants upon electronic excitation is reflected by a change of line spacings for higher J levels of the P-branch, which gives values for B' (C'). The R-branch region consists of a series of unresolved bands with clear bandheads corresponding to $K = 0-7$ as indicated in Figure 20. The distance between the bandheads is a good indication for the value $\Delta A - \Delta B = (A'' - A') - (B'' - B')$, and the intensity ratio can be used to estimate A'' . The Q -branch bands are rather weak and cannot be assigned directly. The overall pattern indicates a rotational temperature of the order of 40(5) K. The rotational profile of the

spectrum was fitted using a simulation program WANG [66]. The observed values of the rotational constants are given in Table 4. The assignment of rotational lines in the P-branch is given in Appendix A (page 79). The rotational constants B and C are found to be about 0.045 cm^{-1} . Comparing this result to the available rotational constants of different kinds of carbon chain radicals determined in previous studies [38, 39, 67] one can conclude that the molecule consists most likely of six or seven carbon atoms. Using C_2D_2 instead of C_2H_2 yields a 67 cm^{-1} blueshifted spectrum with nearly identical spectral features, as shown in Figure 21. This indicates that the carrier is not a bare-carbon species but contains one or more hydrogen atoms.

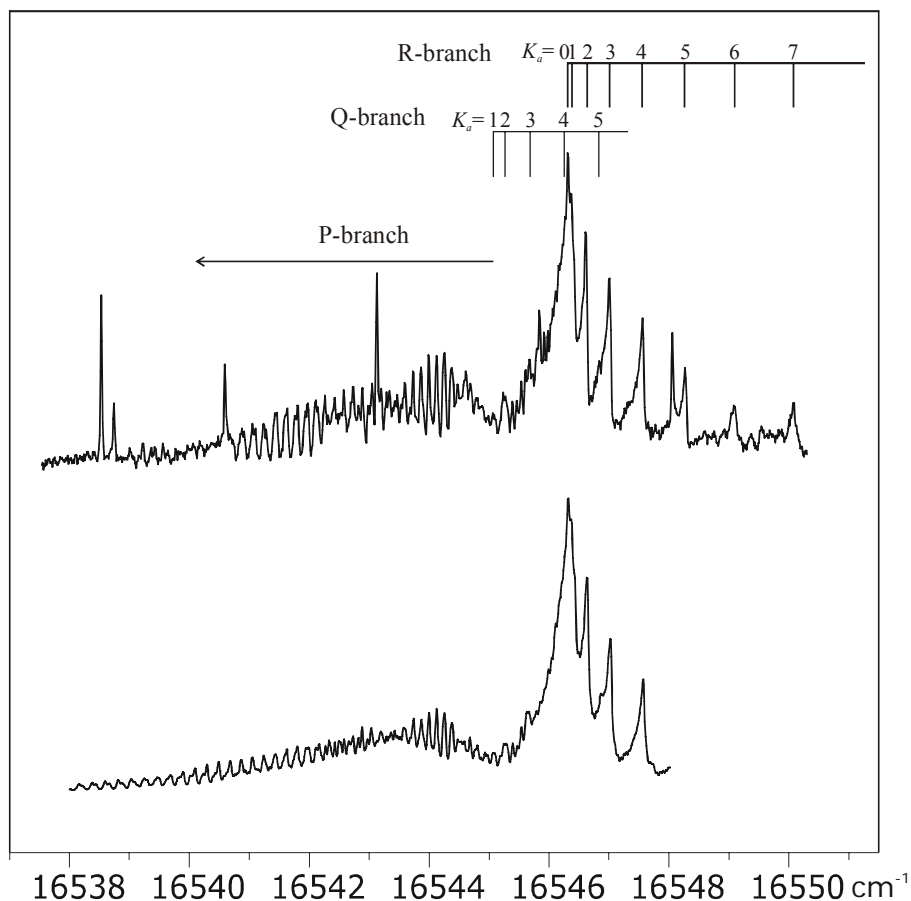


Figure 20. Band observed at 604 nm using CRD spectroscopy through a supersonic planar plasma expansion. The rotational and K -type structure that is observed experimentally (top trace) can be simulated with a rotational temperature of 40 K, using constants derived from geometry optimizations for the nonlinear planar and noncyclic C_6H_4^+ carbon chain cation (second trace).

An effective procedure to determine the number of hydrogen atoms in molecule is to record an absorptions spectrum of mixture of isotopes using a $\text{C}_2\text{H}_2+\text{C}_2\text{D}_2$ mixture. A low-

resolution scan, in which mainly the strong peaks for $K = 0$ and 1 will be visible, gives five broad absorption bands including bands originating from fully H- (16546 cm^{-1}) and fully D- (16613 cm^{-1}) substituted species Figure 22. Three remaining bands located at 16500 cm^{-1} (a), 16560 cm^{-1} (b), and 16595 cm^{-1} (c) are due to partially deuterated species. Taking into account the fact that deuterium isotopic shifts of electronic bands are generally additive [68], it can be concluded that the observed molecule contains four hydrogen atoms: the *a*, *b*, and *c* bands correspond to species with one, two, and three D atoms, respectively. The one-, two-, and threefold-deuterated species should give four, six, and four absorption peaks respectively by statistical arguments, but only three, four, and three peaks are observed. This indicates that two of the four hydrogen atoms are rather similar in their position. The same method cannot be applied to determine the number of carbon atoms because corresponding isotopic shifts are too small and absorption features of partially deuterated derivatives will overlap each other.

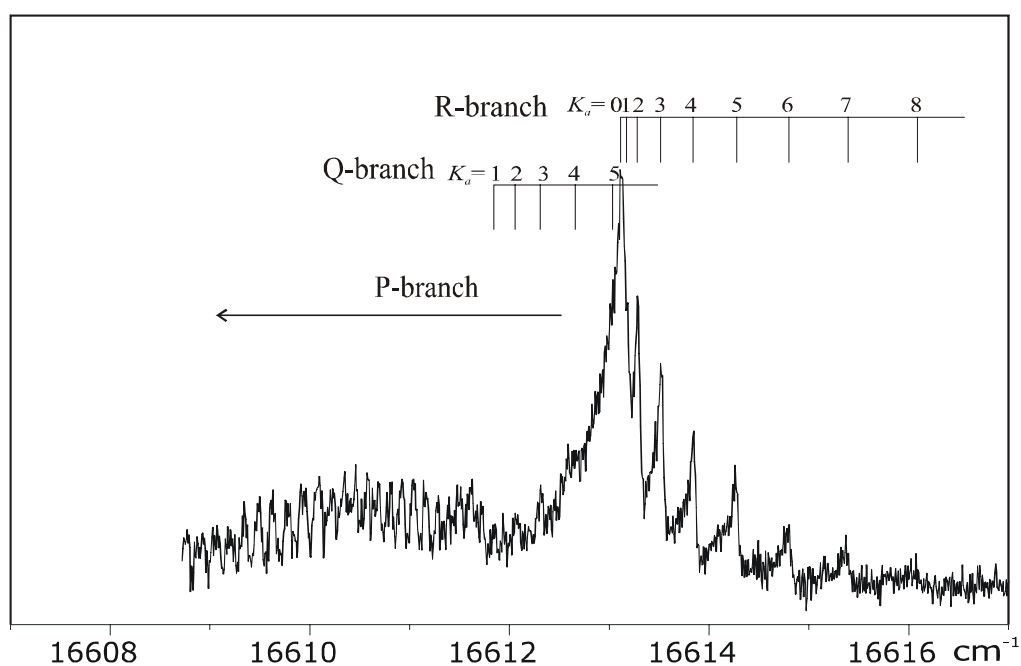


Figure 21. Spectrum for the fully deuterated C_6D_4^+ species, blueshifted by approximately 67 cm^{-1} with respect to the C_6H_4^+ cation.

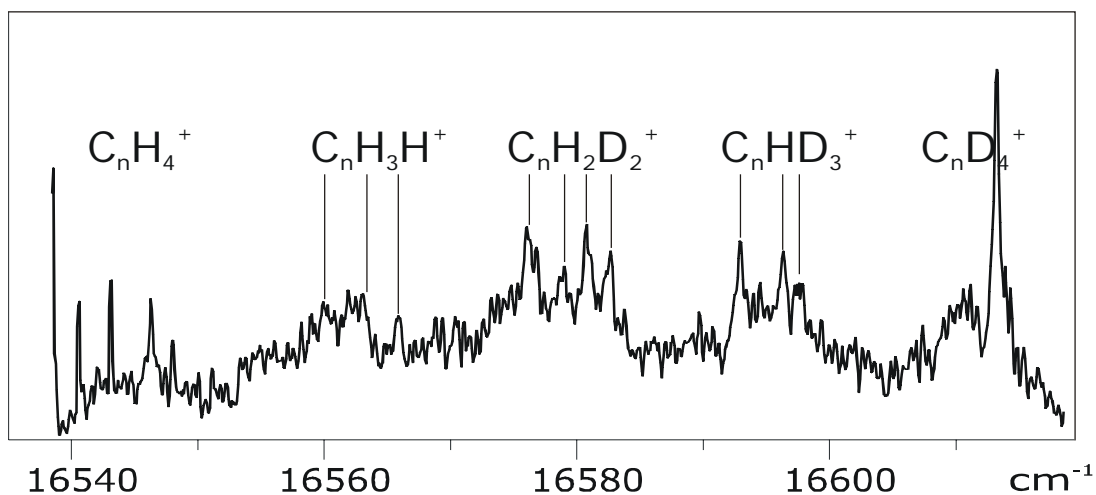


Figure 22. Electronic spectrum of partially deuterated species.

Equilibrium structures for various isomers of $C_6H_4^{(+)}$ and $C_7H_4^{(+)}$ (and fully deuterated isotopes, both neutral and positively charged) have been calculated using MOPAC [69] (PM3/UHF). The structure that gets closest to the observations is that of the nonlinear chain $HC\equiv C-C\equiv C-CH=CH_2^+$ (Figure 23) for which $A'' = 1.230 \text{ cm}^{-1}$, $B'' = 0.0465 \text{ cm}^{-1}$, and $C'' = 0.0448 \text{ cm}^{-1}$. This structure corresponds to one of the geometries calculated in [64] and is close to the previously proposed geometry of the neutral C_6H_4 . Other isomeric structures yield sets of substantially different constants, particularly for the fully deuterated species, whereas the corresponding $DC\equiv C-C\equiv C-CD=CD_2^+$ gives $A'' = 0.889 \text{ cm}^{-1}$, $B'' = 0.0414 \text{ cm}^{-1}$, and $C'' = 0.0395 \text{ cm}^{-1}$, close to the values derived from a fit of the observed spectrum.

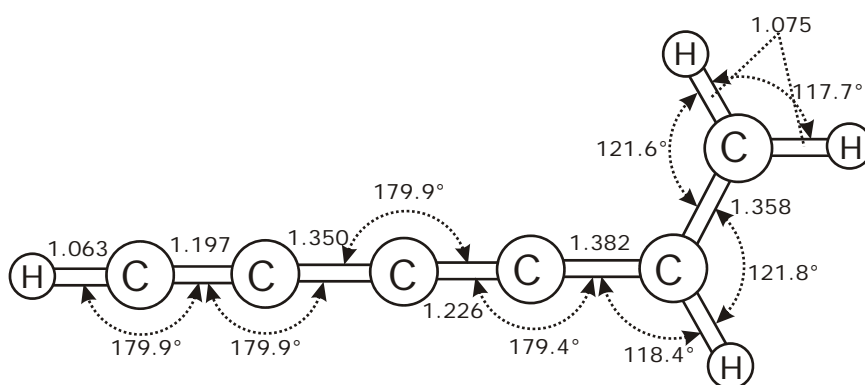


Figure 23. Optimized molecular structure of $C_6H_4^+$ using *ab initio* calculations. The bond lengths are given in Å.

In order to refine the expected geometry of $C_6H_4^+$, *ab initio* calculations have been performed using GAMESS [70]. In previous work ROHF/6-31G** calculations have been reported on the isomerization of C_4H_4 radical cations [71]. An identical method is applied here to $C_6H_4^+$. Rotational constants were determined using the *ab initio* optimized structure with bond lengths and angles as indicated in Figure 23. The resulting constants are summarized in Table 4.

Table 4. Observed and calculated molecular constants of $C_6H_4^+$ and $C_6D_4^+$.

	$C_6H_4^+$		$C_6D_4^+$	
	Observed ^a	<i>Ab initio</i> ^b	Observed ^a	<i>Ab initio</i> ^b
A''	1.24	1.217	0.89	0.889
B''	0.04674	0.0471	0.0416	0.0420
C''	0.04524	0.0453	0.0400	0.0401
$A'-A''$	0.0763		0.0450	
B'	0.04518		0.0403	
C'	0.04375		0.0387	
T_{00}	16 544.965		16 611.91	
^a Expected errors of the rotational constants are 0.1 cm^{-1} in A and 0.001 cm^{-1} in B and C . Expected errors of T_{00} are 0.01 cm^{-1} for $C_6H_4^+$ and 0.1 cm^{-1} for $C_6D_4^+$.				
^b Equilibrium values (ROHF/6-31G**).				

Ray's asymmetry parameter κ for the calculated structure equals -0.997 that confirms that the molecule can be treated as a prolate top. Using the *ab initio* results, the rotational spectrum was simulated with an assumed resolution of 0.05 cm^{-1} (lower trace on Figure 20). The calculated and observed spectra match very well apart from minor intensity deviations and a few absorption lines that belong to another carrier. Similar transition energies of $C_6H_4^+$ and HC_6H^+ suggest that they involve the same $\pi \leftarrow \pi$ excitation in the conjugated chain. In the C_s point group π -orbitals are antisymmetric with respect to the symmetry plane of the molecule, thus, the symmetry of both ground and excited states of $C_6H_4^+$ is A'' and the observed electronic transition can be assigned to ${}^2A'' \leftarrow X^2A''$.

The proof of the absorption band assignment comes from a mass-selective matrix study that was performed following the gas phase analysis. This experiment combines mass selection and matrix isolation spectroscopy and has been described [72]. The $C_6H_4^+$ ($C_6D_4^+$) cations were produced from a phenylacetylene–deuterated-2,4-hexadiyne mixture in helium in a hot cathode discharge source. A 90° deflector and a quadrupole mass spectrometer are used to steer the ion beam onto the matrix, where the mass-selected ions are codeposited with excess of neon at 6 K. The absorption spectra are recorded by guiding monochromatized light (0.1 nm bandpass) through the matrix onto a photomultiplier. The resulting spectra for matrices prepared with mass of $C_6H_4^+$ or $C_6D_4^+$ are shown in Figure 24. Two strong bands are observed, one around 609 nm and one around 585 nm, for $C_6H_4^+$. No strong bands are observed to lower energy; i.e., the band at 609 nm corresponds to the origin band. The main structures to the blue of the dominant peaks (609 nm for $C_6H_4^+$ and 606 nm for $C_6D_4^+$) are matrix artifacts due to a site structure. The 114 cm^{-1} blueshift of the gas-phase spectrum with respect to the matrix band at 609 nm is typical for electronic transition of a chain of this size [59]. The band at 585 nm is due to another isomer of $C_6H_4^+$, since the relative intensity of the two bands varies strongly with different precursors. Upon deuteration the band at 609 nm shifts by $62(3)\text{ cm}^{-1}$ to the blue which is very close to the 67 cm^{-1} shift observed in the gas phase. The band observed at 585 nm in the matrix only shifts $17(3)\text{ cm}^{-1}$ upon deuteration. Subsequent neutralization of the trapped species by irradiation of the matrix with a medium-pressure mercury lamp leads to the disappearance of both bands. This confirms that the carrier of the 609 nm matrix and the 604 nm gas-phase carrier is a $C_6H_4^+$ cation, as was concluded from the gas-phase spectrum.

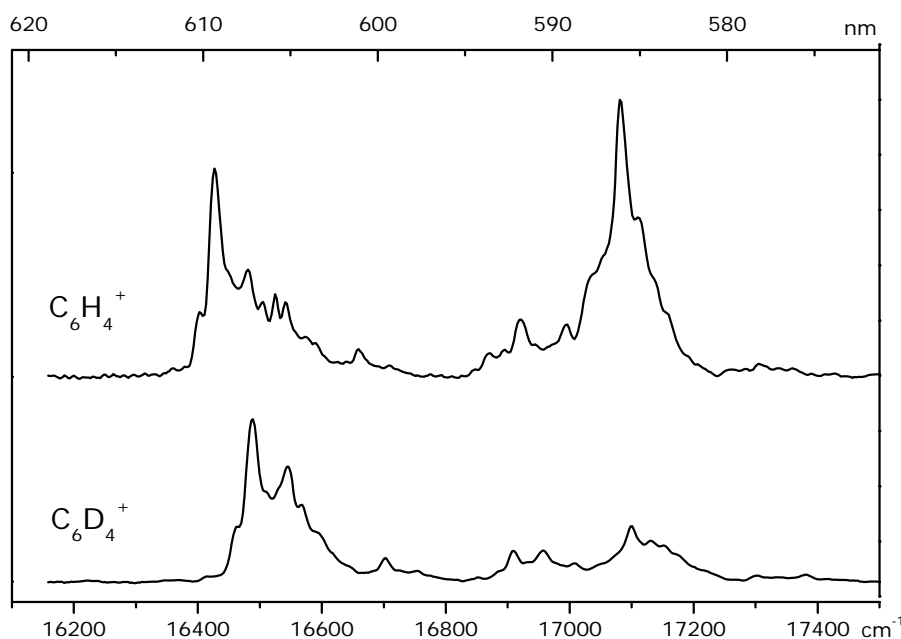


Figure 24. Electronic absorption spectra of $C_6H_4^+$ (upper trace) and $C_6D_4^+$ (lower trace) measured in 6 K matrices after codeposition of mass-selected cations with excess of neon.

Astrophysical relevance

All the spectroscopic information is in favor of the identification of the band observed at 604 nm as due to the ${}^2A''-X\ {}^2A''$ electronic origin band transition of the nonlinear planar $HC\equiv C-C\equiv C-CH=CH_2^+$ carbon chain cation. The inferred rotational constants may guide a search for this species by millimeter-wave spectroscopy to allow a more accurate geometry determination. This is of interest as the number of microwave studies of carbon chain cations is still rather limited [73]. It furthermore would make a radio-astronomical search for this species in dense interstellar clouds possible. The optical spectrum obtained here allows a comparison with the available lists of diffuse interstellar band (DIB) positions [74, 75]. A comparison with the hitherto reported DIBs shows that there exists an overlap between the band observed around $16\ 545\ \text{cm}^{-1}$ and a broad DIB (full width at half maximum (FWHM) $\sim 14\ \text{cm}^{-1}$) reported at $16\ 537.3\ \text{cm}^{-1}$. In order to check whether this discrepancy of $8\ \text{cm}^{-1}$ might be due to a temperature effect, a comparison has been made between an artificial DIB spectrum in the 604 nm range and the simulated $C_6H_4^+$ spectrum for low (10 K), intermediate (40 K), and high (150 K) temperatures (Figure 25). Although it is clear that for higher temperatures the spectrum of the nonlinear $C_6H_4^+$ might start filling up the broadband

around $16\,545\text{ cm}^{-1}$, it is hard to account for the difference in intensity of the *P* and *R* branches. This is not reflected in the DIB spectrum.

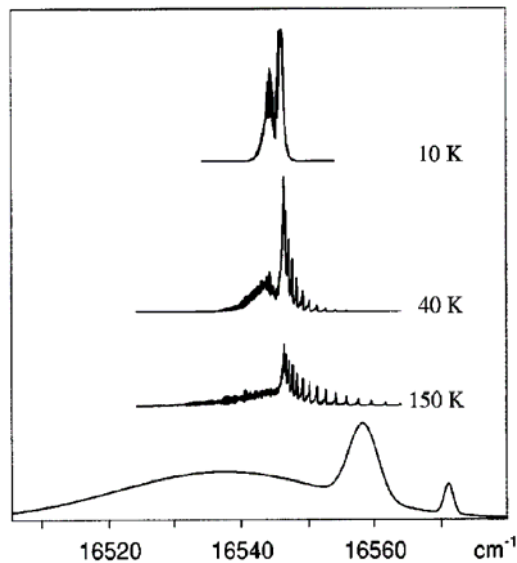


Figure 25 Artificial DIB spectrum ([74]) in the 604 nm range (lowest trace) and the simulated C_6H_4^+ spectra for 10, 40, and 150 K (upper three traces).

Electronic spectroscopy of the nonlinear carbon chains C_4H_4^+ and C_8H_4^+

High-resolution spectroscopy of unsaturated carbon chain radicals is of interest in view of interstellar chemistry, as well as terrestrial discharge and flame processes. Electronic transitions of the polyacetylene cations HC_nH^+ [38, 39, 76, 77] and radicals C_nH [78] with even number carbons have now been studied. Recently a nonlinear planar carbon chain radical C_6H_4^+ , $\text{HC}\equiv\text{C}-\text{C}\equiv\text{C}-\text{CH}=\text{CH}_2^+$, was detected in a supersonic planar discharge with cavity ring down spectroscopy in the 604 nm region [40]. Therefore, the related C_4H_4^+ and C_8H_4^+ nonlinear chains were expected to be produced in the plasma discharge in a sufficient concentration for detection.

Hydrogenated nonlinear chains can exist in dark interstellar clouds as well as linear ones. However, the intensity of rotational transitions for a linear molecule with a smaller rotational partition function is stronger than for an asymmetric top, and thus, a long nonlinear carbon chain has not yet been detected by radio astronomy, even though the population may be comparable. In the case of electronic transitions, an asymmetric top molecule is not at a

disadvantage compared with the linear one. Thus, the nonlinear chains can be considered as candidates, causing the diffuse interstellar band (DIB) absorptions in much the same way as the linear series [79].

The short nonlinear carbon chain $\text{HC}\equiv\text{C}-\text{CH}=\text{CH}_2$ is predicted to be an intermediate between acetylene and polyaromatic hydrocarbons in the interstellar chemistry of circumstellar envelopes [22]. Laboratory experiments indicate that photodissociation of aromatic molecules produces a nonlinear carbon chain [64]. The potential energy surface for three C_4H_4 isomers is also of relevance in the fields of organic chemistry and reaction dynamics [80]. Therefore, species and their ions having $\text{H}-\text{C}_n-\text{CH}=\text{CH}_2$ ($n = 2, 4, 6, \dots$) nonlinear chain structures are of interest, and information by high-resolution spectroscopy is needed.

The 604 nm origin of the ${}^2\text{A}''\text{-X}^2\text{A}''$ transition of C_6H_4^+ [40] is close to the 600 nm ${}^2\Pi_u\text{-X}^2\Pi_g$ one of HC_6H^+ [77]. Both transitions involve the same $\pi \leftarrow \pi$ excitation. The transition energy difference in a homologous series should be comparable because C_6H_4^+ and HC_6H^+ are produced by an extension of the acetylene chain from C_4H_4^+ or HC_4H^+ [81]. The same argument may be applied to the six- and eight-carbon chain species. This trend is shown in Figure 26a, and the transition energies of C_4H_4^+ and C_8H_4^+ are consequently estimated to lie near 510 and 712 nm, respectively.

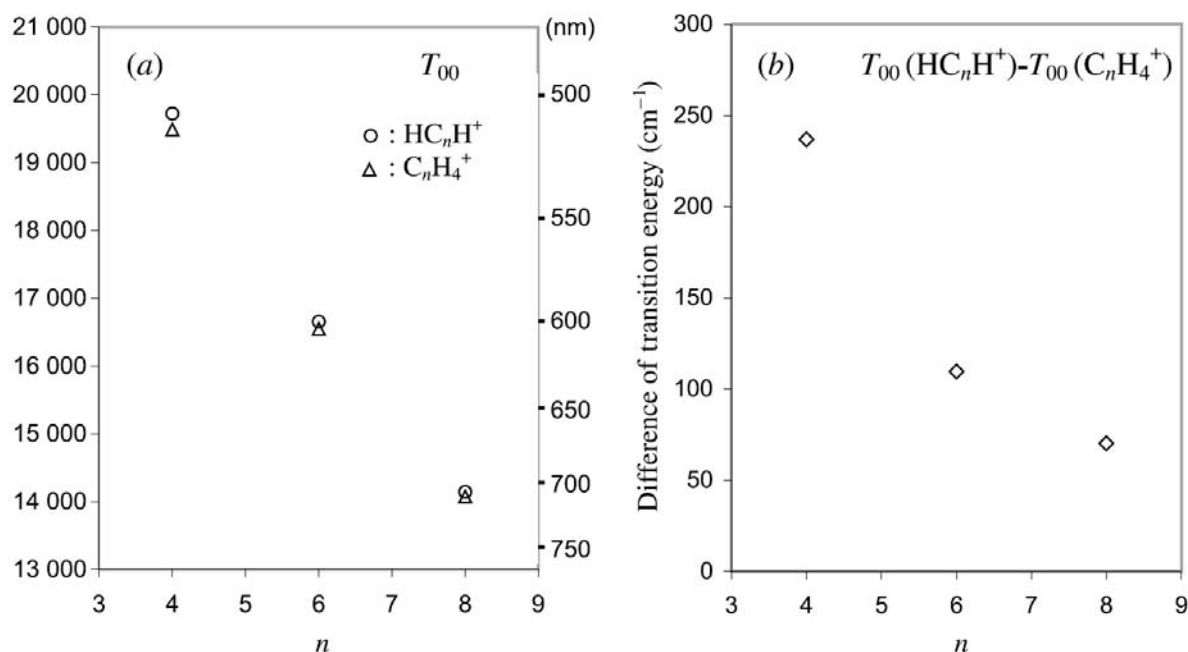


Figure 26. (a) Energies of the origin bands in the $2\Pi_u\text{-X}^2\Pi_g$ transition of HC_nH^+ and the $2\text{A}_1\text{-X}^2\text{A}_1$ transition of C_nH_4^+ . For HC_nH^+ ($n = 4, 6, 8$) and C_6H_4^+ , those are the observed values. The transitions of C_4H_4^+ and C_8H_4^+ were estimated by shifting the HC_4H^+ and HC_8H^+ values down by the difference

of HC_6H^+ to C_6H_4^+ ; (b) Observed transition-energy differences between HC_nH^+ and C_nH_4^+ with the same number of carbon atoms.

The electronic transition of mass-selected C_4H_4^+ was subsequently observed in a neon matrix with origin band at 515 nm, in good agreement with the estimated value. Based on this, the gas-phase spectrum was searched for in a cavity ring down spectrometer, and the origin band was observed at 513 nm. Similarly the electronic transition of C_8H_4^+ was also detected in the gas phase in the expected 712 nm region. The observed rotational structure in the gas-phase spectra indicates that these are due to the nonlinear, planar carbon chains $\text{HC}\equiv\text{C}-\text{CH}=\text{CH}_2^+$ and $\text{HC}\equiv\text{C}-\text{C}\equiv\text{C}-\text{C}\equiv\text{C}-\text{CH}=\text{CH}_2^+$.

Results and discussion

To locate the electronic transition of C_4H_4^+ , neon-matrix isolation spectroscopy in combination with mass selection was used at first. The C_4H_4^+ cation was produced from benzene–helium mixture in a hot cathode discharge source. A 90° deflector and a quadrupole mass spectrometer were used to steer the ion beam onto the substrate, where the mass-selected ions were codeposited with excess of neon at 6 K [72]. The absorption spectra were recorded by guiding monochromatized light (0.1 nm bandpass) through the matrix onto a photomultiplier. The observed spectrum is shown on Figure 27.

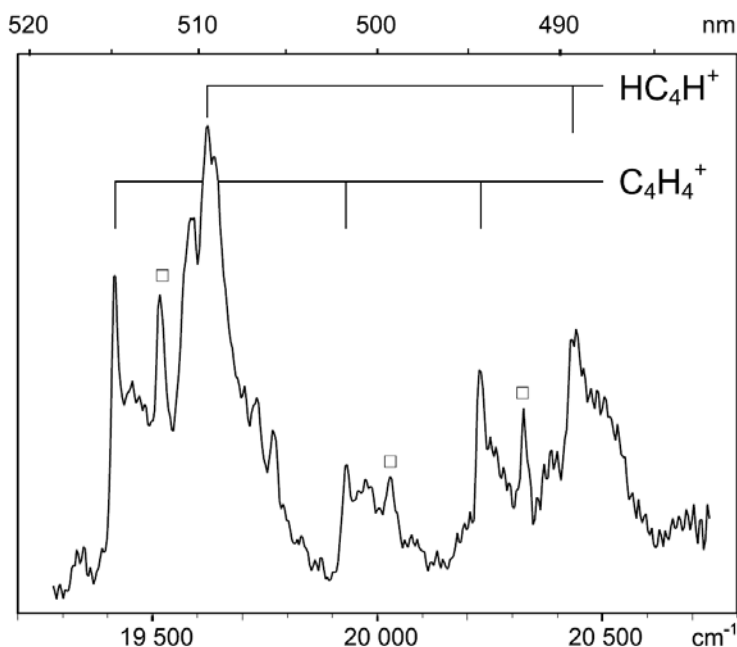


Figure 27. The electronic absorption spectrum of C_4H_4^+ , measured in a 6 K matrix after codeposition of mass-selected cations with excess of neon. The peaks marked with \square that are located 100 cm^{-1} to the blue from the dominant ones are matrix artifacts due to site structure. The bands at 19630 and 20440 cm^{-1} are due to the diacetylene cation HC_4H^+ .

All bands observed in the absorption spectrum disappeared upon UV irradiation of the matrix, a test used to indicate that the species is a cation. Three bands of $C_4H_4^+$ were observed; the one at 19416 cm^{-1} can be assigned to the origin of the electronic transition and the 19931 and 20229 cm^{-1} ones to transitions to excited levels in the upper electronic state corresponding to vibrational frequencies of 515 and 813 cm^{-1} , because the population of the species at 6 K is entirely in the lowest level of the ground state.

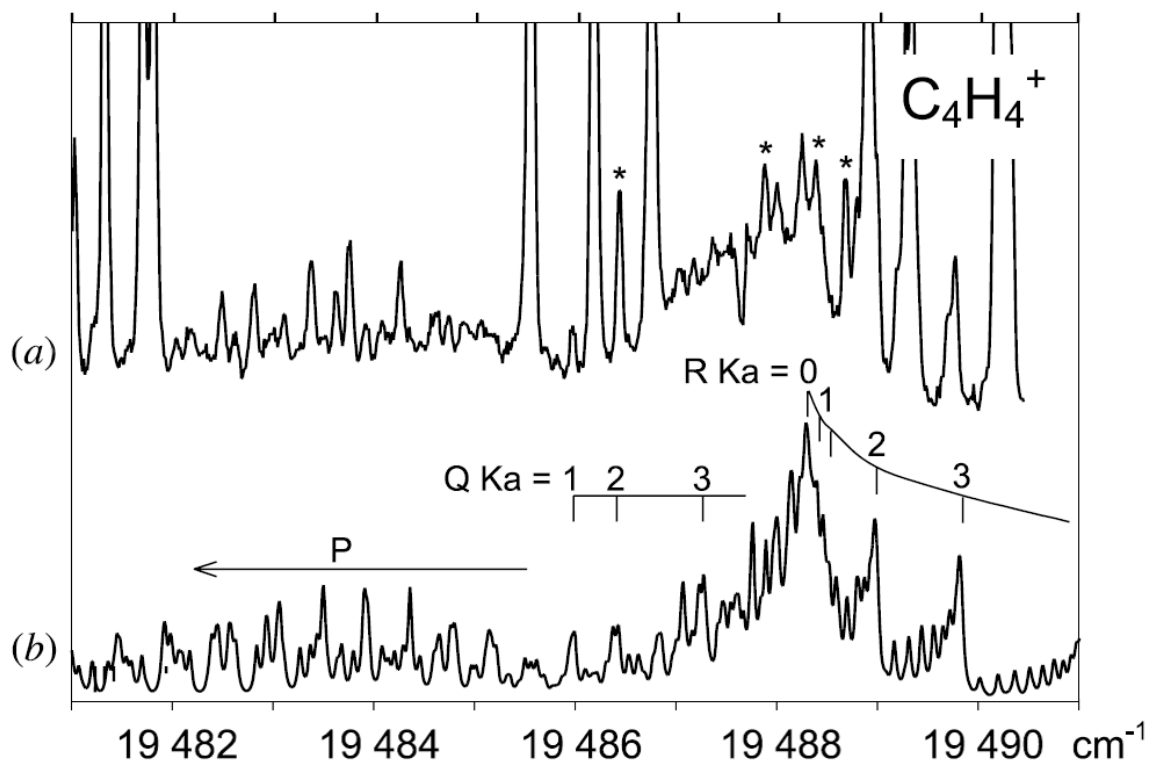


Figure 28. The origin band of the ${}^2A''\text{-}X^2A''$ electronic transition for $C_4H_4^+$ observed using cavity ring down spectroscopy through a supersonic planar plasma expansion. The observed rotational structure (a) can be simulated with a temperature of 30 K using constants derived from geometry optimization by *ab initio* calculation (b). Bands marked with * are due to another carrier. The peaks going off-scale are due to the Swan bands of C_2 and were used for the frequency calibration.

The origin transition of $C_4H_4^+$ was searched for around the 19416 cm^{-1} region, and a band having P- and R-branches was found at 19486 cm^{-1} , as shown in Figure 28a. The deuterated species could not be detected unambiguously due to many absorption lines of C_2 overlapping the expected region of $C_4D_4^+$ absorption.

The energy of the electronic transition of $C_8H_4^+$ was expected around 14030 cm^{-1} by reference to Figure 26. One band was found in the gas phase at 14073 cm^{-1} , as shown in Figure 29. The optimized condition was quite similar to that for $C_6H_4^+$, a -300 V discharge

through a mixture of 0.5% C₂H₂ in helium and with probing 1.5 mm downstream from the slit.

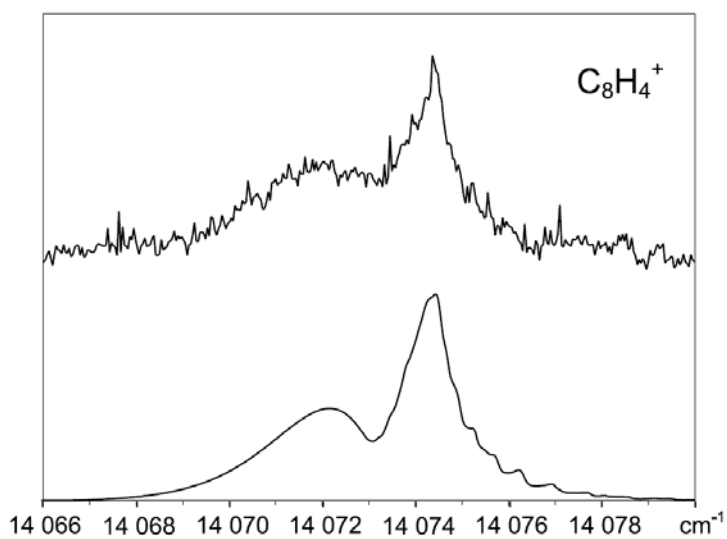


Figure 29. The ${}^2A''-X^2A''$ origin band in the electronic transition for $C_8H_4^+$ observed using cavity ring down spectroscopy through a supersonic planar plasma expansion. The rotational structure observed (upper trace) can be simulated (lower trace) using constants derived from geometry optimization by an ab initio calculation and a temperature of 50 K.

The differences in frequency between the observed origin bands of $C_4H_4^+$, $C_6H_4^+$, and $C_8H_4^+$ and of the corresponding HC_nH^+ series [38, 76, 77] are 237, 110, and 70 cm^{-1} , as shown in Figure 26*b*. The shifts decrease with increasing number of carbon atoms. This indicates that the contribution of the nonlinear part, $-CH=CH_2$, to the molecular orbital decreases on extension of the carbon chain. This trend in the two homologous series suggests that the observed bands can be assigned to $C_4H_4^+$ and $C_8H_4^+$ with the common chain structures. $C_8H_4^+$ has five isomers constructed by combination of ethylene and acetylene, as shown in Figure 30.

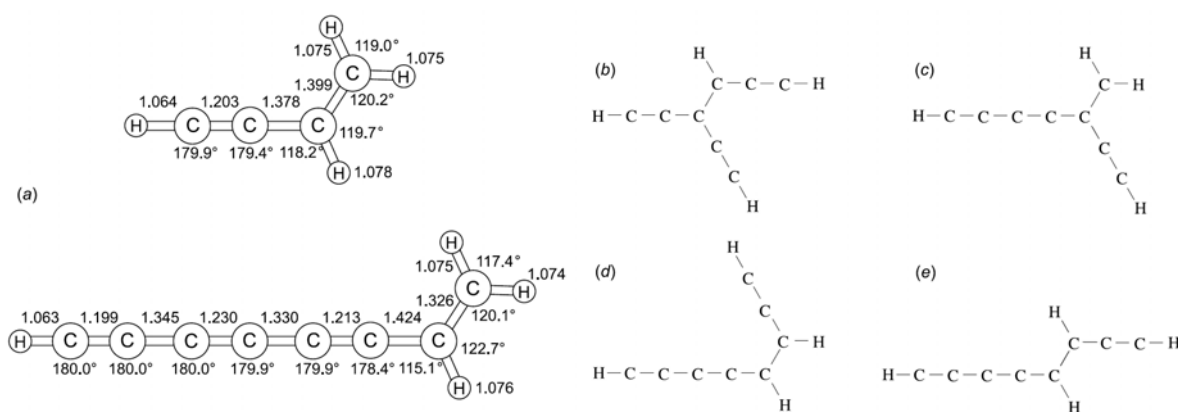


Figure 30. Optimized molecular structure in the ground state of $C_4H_4^+$ and $C_8H_4^+$ using *ab initio* calculations. The bond lengths are given in Å. Other isomers of $C_8H_4^+$ are indicated by simple pictures.

Structure (b) is intermediate between a prolate and an oblate top, but the observed spectrum has the profile of a typical near-prolate top and a-type transition. In the view of this, structure (b) is rejected as the carrier of the observed spectrum. Geometries (b) and (c) do not have eight carbons in a line but instead have a branching structure. Owing to the correlation of the transition energy of $C_nH_4^+$ and HC_nH^+ (Figure 26), these should be π - π type electronic excitations in the conjugated system. Transition energies of the structures (b) and (c) would not show the correlation with the HC_nH^+ series. Structures (d) and (e) are cis and trans isomers, and both should have their electronic transition close to each other. No other signal could be detected within ± 100 cm^{-1} from the observed band. Thus, the structures (c), (d), and (e) can be rejected as candidates for the observed spectrum. There remains structure (a), which would correlate with the HC_nH^+ series, and therefore this is the best candidate for the assignment. Consequently the symmetry of the electronic transitions observed for $C_4H_4^+$ and $C_8H_4^+$ is ${}^2A''-X^2A''$.

Determination of the rotational constants from the observed spectra is difficult because of overlap by the Swan bands of C_2 [82] in the case of $C_4H_4^+$ (Figure 28) and the non-resolved

rotational contour on $C_8H_4^+$ (Figure 29). Thus, the rotational constants and molecular structure in the ground state of $C_4H_4^+$ and $C_8H_4^+$ were determined by *ab initio* calculations using GAMESS [70] with ROHF/6-31G**, the same method used in previous works [40, 71]. The optimized bond lengths and angles are given in Figure 30. From the latter, the rotational constants were calculated (Table 5).

Table 5. Calculated rotational constants and assumed ratios between the ground and excited states.

	$C_4H_4^+$	$C_6H_4^+$ [40]	$C_8H_4^+$
A'' (cm^{-1})	1.562	1.217	1.220
B'' (cm^{-1})	0.162	0.0471	0.0193
C'' (cm^{-1})	0.147	0.0453	0.0190
A''/A'	0.91	0.94 ^a	0.96
$B''/B', C''/C'$	1.06	1.03 ^a	1.01

^a Experimentally determined

In the case of the polyacetylene cations HC_nH^+ , the ratio B''/B' of rotational constants between the ground and excited states decreases and approaches 1.0 on extension of the carbon chain (Figure 31).

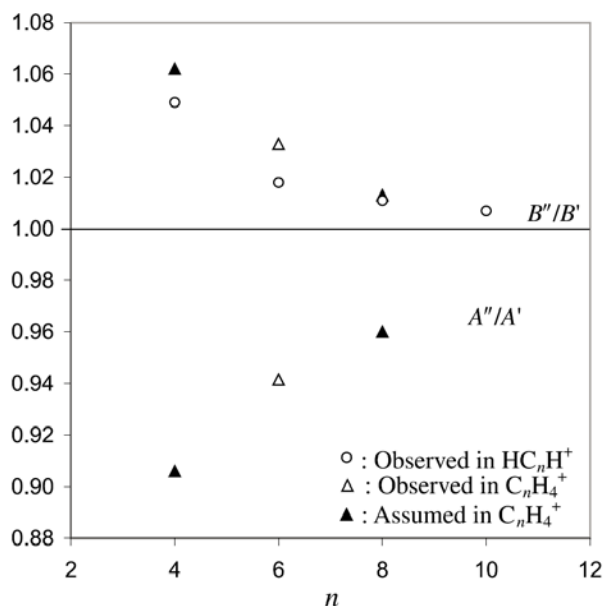


Figure 31. Ratios of rotational constants between the ground and excited states for HC_nH^+ and $C_nH_4^+$. A''/A' are <1.0 whereas B''/B' are >1.0 , and it is assumed that $B''/B' = C''/C'$ in $C_nH_4^+$.

The ratios B''/B' and C''/C' for the $C_nH_4^+$ series should follow the same trend and converge to the HC_nH^+ value for the long chains. Ratio A''/A' should increase and approach 1.0 on extension of the carbon chain. These trends were assumed in order to estimate the

rotational constants in the excited states of $C_4H_4^+$ and $C_8H_4^+$ (Table 5). The profiles of the origin bands in the electronic transitions of $C_4H_4^+$ and $C_8H_4^+$ were then simulated using the ground-state rotational constants given by the *ab initio* calculation and the extrapolated excited-state values from the $C_6H_4^+$ data. The observed profiles are then well reproduced (Figure 28 and Figure 29) using the WANG program [66]. By comparison of the simulated and observed spectra, the assignments were confirmed, and more accurate transition frequencies were inferred. These are given in Table 6.

Table 6. Comparison of the origins (cm^{-1}) of the ${}^2A''-X{}^2A'$ electronic transition of $C_nH_4^+$ and ${}^2\Pi_u-X{}^2\Pi_g$ of HC_nH^+ .

n	HC_nH^+	$C_nH_4^+$	ΔT_{00}
4	19722.61 [76]	19485.80	236.81
6	16654.69 [77]	16544.98 [40]	109.71
8	14143.18 [38]	14073.00	70.18

The optical spectrum obtained for $C_8H_4^+$ allows a comparison with the available lists of DIB positions [74, 75]. This shows that there is an overlap between the band observed around 14073 cm^{-1} and two DIBs reported at 14068.9 and 14078.4 cm^{-1} . To check whether these differences in frequency might be due to a temperature effect, a comparison was made between an artificial DIB spectrum in the 709–714 nm range and the simulated $C_8H_4^+$ spectrum for the temperature of 150 K as shown on Figure 32. The absorption band of the nonlinear $C_8H_4^+$ does not fit the DIB absorption.

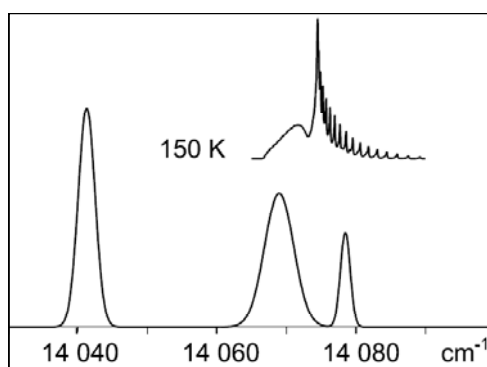


Figure 32. Artificial diffuse interstellar band absorptions in the 709–714 nm range (lower trace reproduced from ref. [74]) and the simulated $C_8H_4^+$ laboratory spectra at 150 K (upper traces).

An upper limit of the column density for the $C_nH_4^+$ series in diffuse clouds can be estimated by comparison of the laboratory and DIB data in a similar fashion to that used before [83]. For this, it is assumed that the oscillator strengths of the 0–0 band in

the ${}^2A''-X^2A''$ transition for $C_nH_4^+$ ($n = 4, 6, 8$) and $A^2\Pi_u-X^2\Pi_g$ for HC_nH^+ (22) are equal (i.e., 0.04, 0.06, and 0.08 for $C_4H_4^+$, $C_6H_4^+$, and $C_8H_4^+$) and that a signal-to-noise ratio of 5 is required for detection of a DIB absorption. The FWHM of the bands is about 2 \AA , and the sensitivity limit for detection is 0.002 \AA [74]. This leads to upper limits for their column densities of 2×10^{12} , 1×10^{12} , and $0.6 \times 10^{12} \text{ cm}^{-2}$ for $C_4H_4^+$, $C_6H_4^+$, and $C_8H_4^+$, respectively.

CHAPTER 8. UNPUBLISHED RESULTS

Rotationally resolved spectrum of a vibrational band of ${}^2\Pi-X^2\Pi$ transition of C_6H

The recent detection of the ${}^3\Sigma^- - {}^3\Sigma^-$ electronic transition of C_6H^+ in neon matrices at 515.8 nm [84] has stimulated the search of the corresponding gas phase absorption spectrum in this range. Considering the usual shifts of gas phase spectra compared to neon matrices, the absorption spectrum was recorded in the range 512 to 517 nm using an acetylene mixture in helium as the plasma precursor. The spectrum reveals five absorption bands with similar profiles (Figure 33) that could match the rotational profile of the C_6H^+ ion. Nevertheless, none of these bands could be attributed to the absorption of C_6H^+ for several reasons.

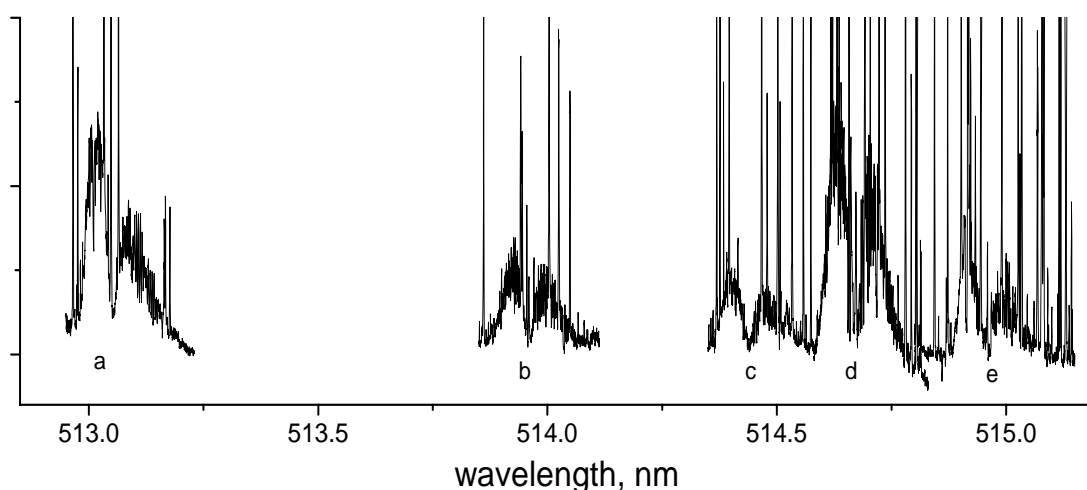


Figure 33. The overview of the observed absorption bands in the region 513-515 nm.

The stronger absorption signal was observed when a higher voltage was applied to the discharge nozzle, an empirical indication of a neutral carrier species as discussed above. Band *b* has a pronounced Q-branch, whereas it should be missing in the spectrum of a $\Sigma - \Sigma$ transition. Bands *a* and *e* have a complicated rotational structure, indicating the presence of a nonlinear carrier molecule. Noticeably similar rotational profiles of bands *c* and *d* suggest that they may arise from the same electronic transition, perhaps being the two spin-orbit components of a ${}^2\Pi - {}^2\Pi$ electronic transition. Such a transition, belonging to the C_6H radical, has been observed previously at 526.5 nm, which corresponds to an energy shift of 440 cm^{-1} . This energy shift could be attributed to a vibrational excitation of the molecule. To test this

assumption the rotational structure of the ${}^2\Pi\text{--}{}^2\Pi$ electronic transition of C_6H was simulated in PGOPHER [85] using the reported spin-orbital interaction (A) and rotational constants (B) for ground and excited states [86]. Afterwards, the fit of individual rotational lines was performed by variation of the energy of the excited state and the corresponding rotational constant B' . The table of the assigned rotational lines can be found in Appendix A (page 83).

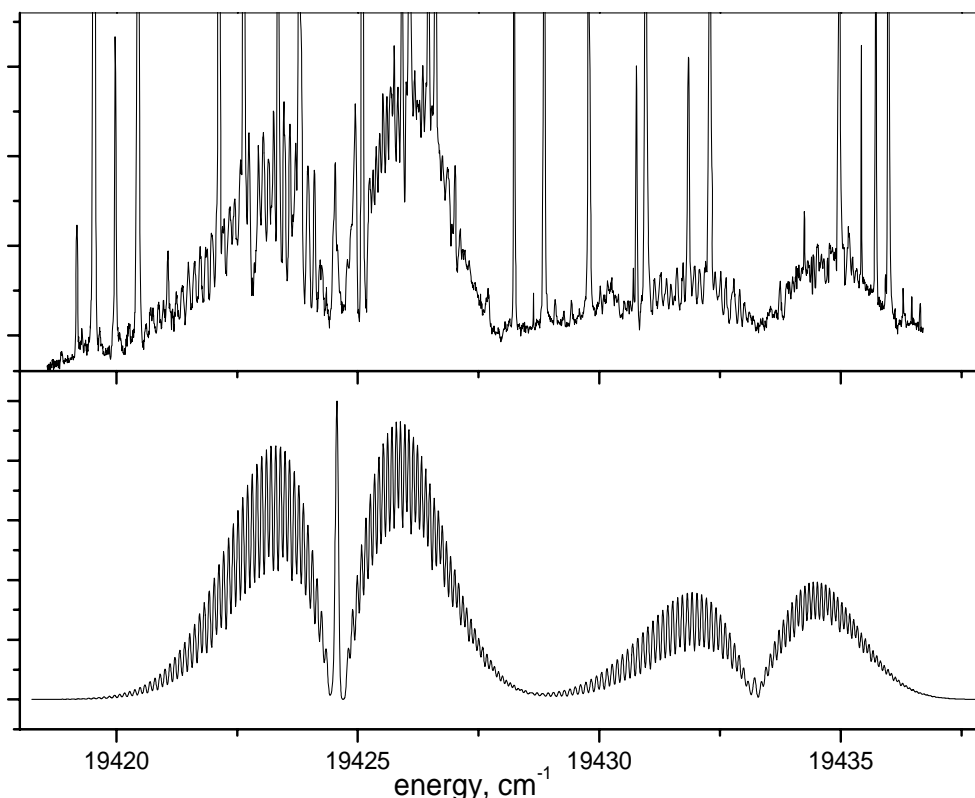


Figure 34. Observed spectrum of the vibrational band of C_6H (upper trace) and its simulation (lower trace).

Figure 34 shows the comparison of the observed and the simulated spectra. The same spacing and intensity ratio of the spin-orbit components of the spectrum is already a good indication that the spectrum belongs to the same electronic transition as the origin band at 526.5 nm. The assignment is confirmed by a good match of the individual rotational lines of the observed and simulated spectra. All obtained spectroscopic constants are given in Table 7. The vibrational excitation energy in the upper electronic state is 439 cm^{-1} and can be due to a bending motion. The spectral resolution of 0.07 cm^{-1} (as estimated by the simulation) is not sufficient to resolve l -type splitting of rotational lines due to the rotation-vibration interaction.

Table 7. Spectroscopic constants for ground and excited states of C₆H.

	Origin band	Vibrational band
ΔE	^a 18989.7677(7) cm ⁻¹	^b 19428.8974(67) cm ⁻¹
A''	^a -15.04 cm ⁻¹	
A'	^a -23.6876(10) cm ⁻¹	
B''	^a 0.046404974(1) cm ⁻¹	
B'	^a 0.0455976(17) cm ⁻¹	^b 0.046208(18) cm ⁻¹

^a Values taken from [86].

^b Values were obtained through rotational lines fit in PGOPHER.

New measurement of C₅ absorption band at 510.93 nm

The first gas phase absorption spectrum of the ${}^1\Pi_u \leftarrow X^1\Sigma_g^+$ electronic transition of C₅ has been measured by CRDS in 1999 [87]. Since then the data processing routine has been improved so that the ringdown time is determined by an exponential fit of the whole ringdown event instead of using only two gates in the beginning and in the end of the light decay [88]. The electronic absorption spectrum of C₅ was recorded once again to compare the sensitivity of new fitting method. The upper trace on Figure 35 is recorded using a complete exponential fit whereas the lower trace represents the spectrum recorded in 1999. The latter was scaled so that the noise levels of the two spectra match each other.

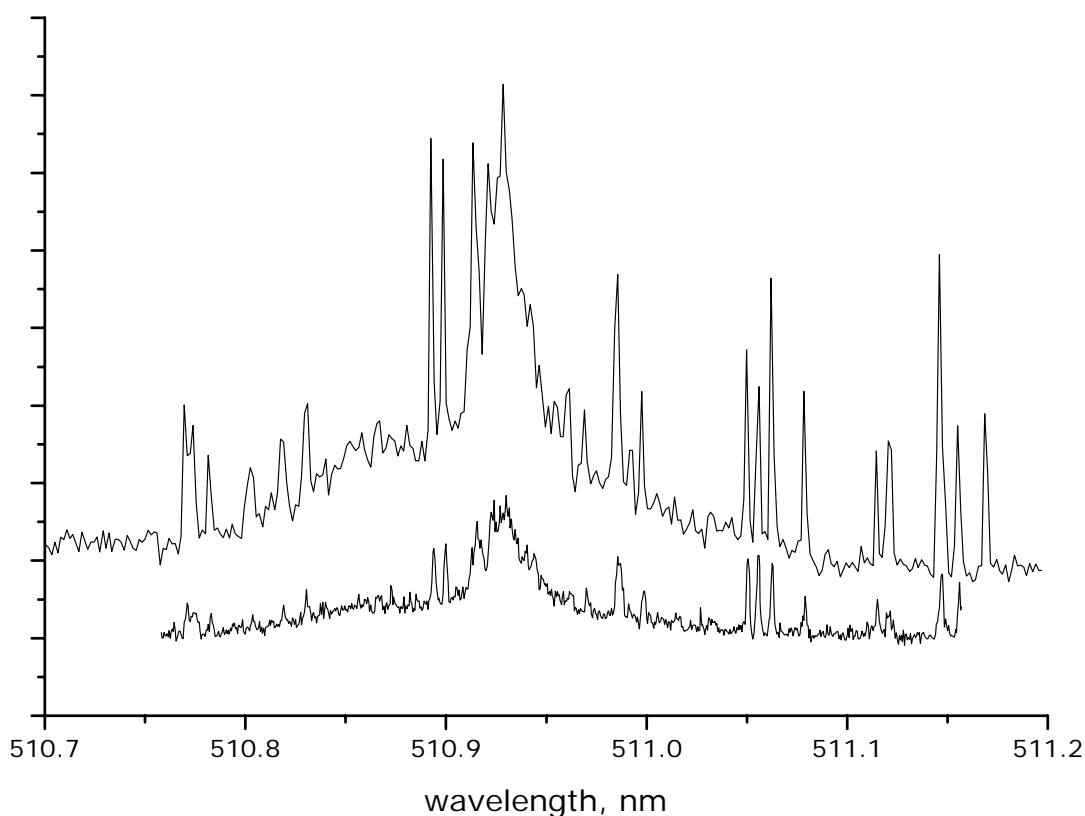


Figure 35. The origin band of the ${}^1\Pi_u \leftarrow X^1\Sigma_g^+$ electronic transition of C_5 recorded with 0.15 cm^{-1} laser bandwidth by new (upper trace) and by previous (lower trace) fitting program.

Compared to previous results, the new fitting method is about three times more sensitive as indicated by the *signal-to-noise* ratio. The higher sensitivity gives the possibility to resolve more details using the intracavity etalon (0.05 cm^{-1}). The resulting spectrum, presented in Figure 36, does not exhibit any regular substructure that could be used for rotational analysis. The sharp peaks belong to C_2 lines as was shown before [87]. The new data, however, suggests that a narrow dip in the absorption spectrum, marked with an asterisk, probably does not arise from an overlap with C_2 lines. If the dip that has a width of 0.07 cm^{-1} is indeed a feature of the C_5 rotational profile, then no significant broadening can be attributed to the spectrum. This, however, would be in contrast to the previous results on the profile analysis when the spectrum could be simulated only if 0.7 cm^{-1} broadening was assumed. *Ab initio* calculations [89] suggest that the excited electronic state of C_5 at 2.4 eV can be nonlinear, which could give rise to the complicated rotational profile of the observed electronic transition.

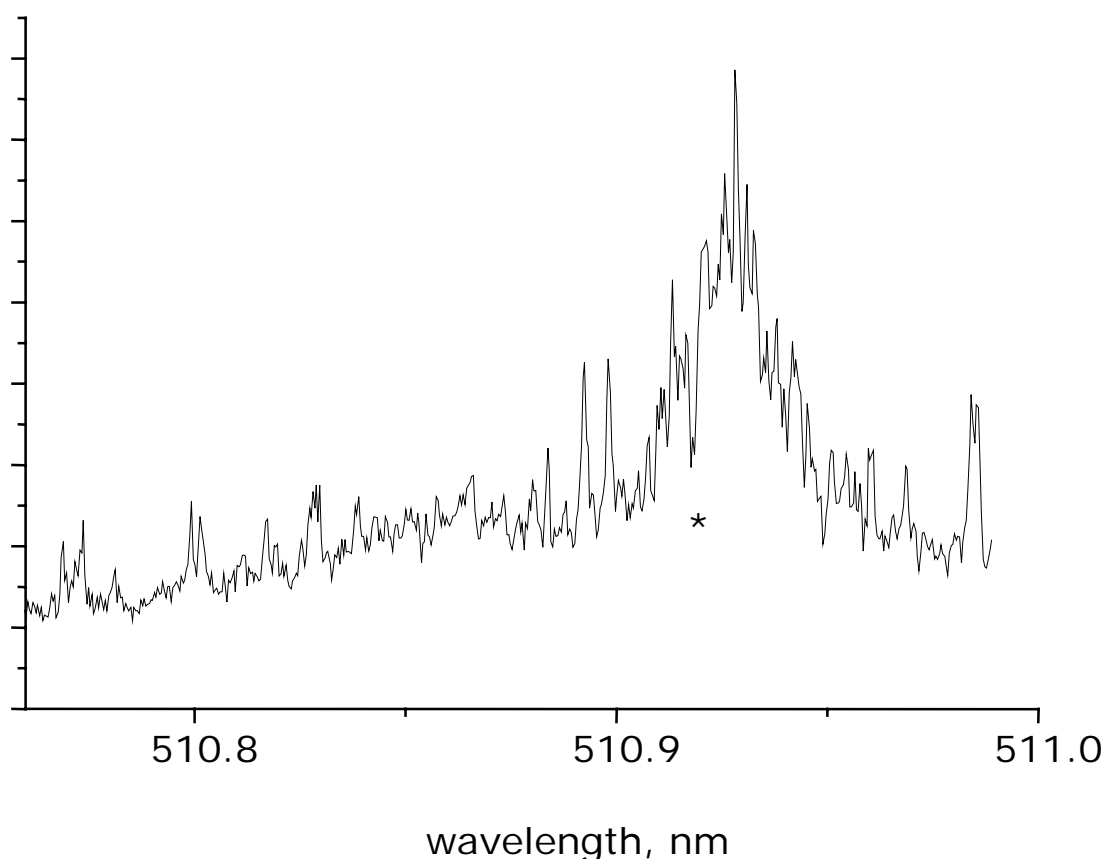


Figure 36. Higher resolution absorption spectrum of ${}^1\Pi_u \leftarrow X^1\Sigma_g^+$ absorption band of C_5 recorded with laser bandwidth of 0.05 cm^{-1} .

Refined position of $C_{10}H$ electronic absorption band

The position of the ${}^2\Pi \leftarrow X^2\Pi$ transition of $C_{10}H$ at 14000 cm^{-1} [78] is close to the broad DIB positioned at 14005.7 cm^{-1} . The absorption spectrum was recorded once again using 0.5% C_2H_2 in neon at a stagnation pressure of 8.5 bar. The pressure in the chamber was maintained at 0.088 mbar and -800 V was applied to the electrodes of the discharge nozzle. The spectrum was calibrated using a Burleigh WA-4500 wavemeter. The precision of the wavemeter was controlled using atomic absorption lines of the noble gases. The absorption band of $C_{10}H$ is homogeneously broadened and was fitted to a Lorentzian shape using Origin® software in order to obtain the exact peak position. The maximum of the fitted band is located at $714.033(3)\text{ nm}$ (14001.1 cm^{-1}) which is 1.1 cm^{-1} blue-shifted from the previously reported position. The FWHM of the band is 7.3 cm^{-1} , which corresponds to a lifetime in the excited electronic state of 0.7 ps.

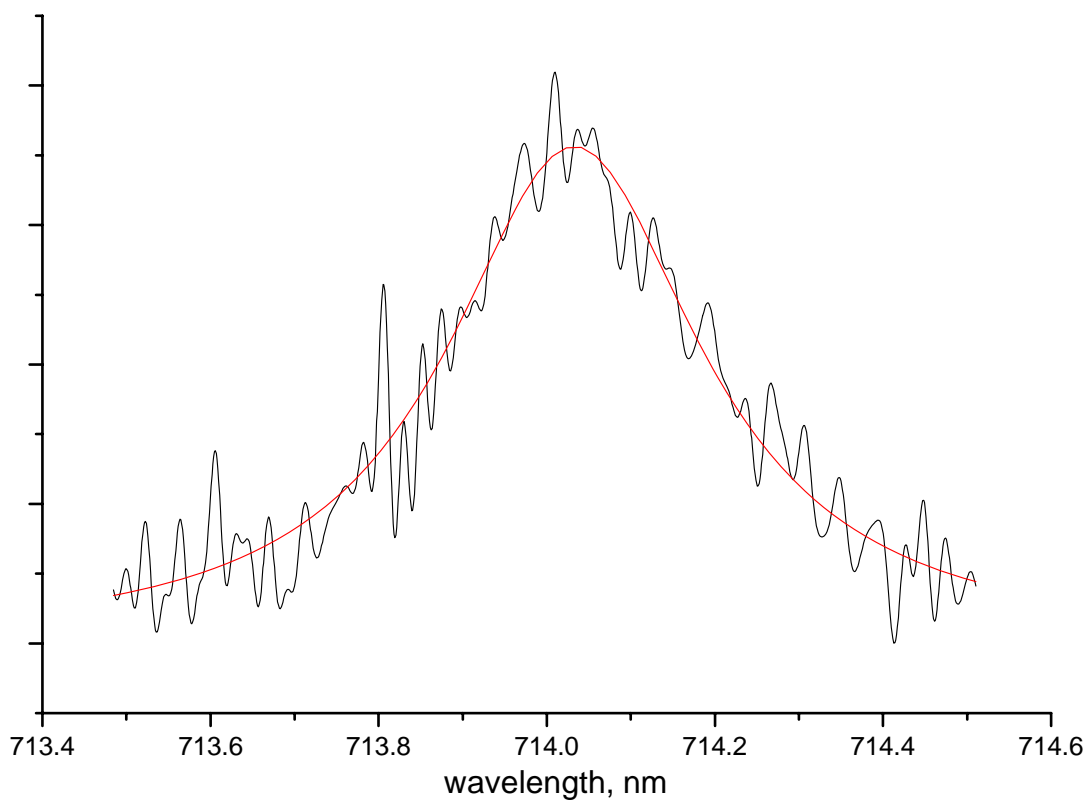


Figure 37. Calibrated spectrum of the ${}^2\Pi\text{-}{}^2\Pi$ electronic transition of C_{10}H recorded with 0.15 cm^{-1} laser bandwidth and the Lorentzian fitted curve.

Table 8. The parameters of the Lorentzian fit of the ${}^2\Pi\leftarrow X\text{ }{}^2\Pi$ electronic absorption band of C_{10}H .

	Value	Uncertainty
λ_{max}	714.033 nm	0.003 nm
w	0.372 nm	0.019 nm

CHAPTER 9. AN APPROACH TO THE GAS-PHASE ABSORPTION SPECTRUM OF C₆₀⁺

The spontaneous formation of the fullerene molecule C₆₀ in carbon-rich environments and its remarkable stability suggests that it could be one of the major forms of carbon in the interstellar space. The ionization potential of the fullerene is 7.58 eV so one can expect that a large fraction of interstellar fullerene would exist in the ionic form. The best electronic absorption spectrum of C₆₀⁺ reported so far [90] was recorded in a neon matrix. The origin band was found at 10368 cm⁻¹ along with a strong satellite peak lying 67 cm⁻¹ to higher energy, presumably corresponding to two slightly different C₆₀⁺ structures trapped by the matrix environment. Subsequently, two diffuse interstellar bands were found at 9577 Å and 9632 Å that were only shifted by 3 and 10 cm⁻¹ compared to laboratory measurements of C₆₀⁺ [91]. The bands were later found to correlate in intensity [92] indicating a possible relation between the carriers of two DIBs. However, because the gas-phase spectrum of C₆₀⁺ can be shifted compared to the one obtained in neon matrices, the identification of these bands remains tentative.

First fullerenes were produced in the gas phase by laser ablation of a carbon disk [93]. However, because of the short laser pulse duration, it is not possible to obtain a stable flow of fullerene molecules for the 100 μs period – the time necessary to record a single ringdown event. This was demonstrated by comparison of the C₅ electronic absorption spectra obtained with pulsed discharge nozzle and with ablation sources [87]. Here an alternative approach is discussed, based on building an effusive source of C₆₀ with subsequent ionization by electron impact.

The vapor pressure of fullerene in the temperature range 723–1096 K is given by Matsumoto et al. [94]

$$\log(P_{\text{atm}}) = 4.91 - \frac{8209.7}{T}$$

At 800 K the pressure of fullerene would be 3.4·10⁻³ torr which is equivalent to the concentration of 4.0·10¹³ cm⁻³.

The total intensity of the effusive source for practical application may be written as

$$I(0) = 1.125 \cdot 10^{22} \frac{p_0}{\sqrt{MT}} \sigma \left[\frac{\text{molecules}}{\text{sr} \cdot \text{s}} \right] \quad [95]$$

where p_0 is the pressure in torr within the source, σ is the area of the source orifice in square centimeters, and M and T are the molecular weight and the absolute temperature of

gas, respectively. Assuming that the source will have a 100 μm slit with a length of 3 cm, the intensity of the fullerene source will be $1.5 \cdot 10^{15}$ molecules $\text{sr}^{-1} \text{s}^{-1}$. The average velocity of fullerene molecules at 800 K is 130 m/s and the concentration of C_{60} near the nozzle opening can reach $3 \cdot 10^{13} \text{ cm}^{-3}$. Afterwards, fullerene molecules can be efficiently ionized by electron impact source. The ionization crosssection σ of C_{60} by electrons with the energy of 70–300 eV exceeds 10^{-15} cm^2 [96]. According to Labmert-Beer's law, the intensity of an electron beam passing through the cloud of fullerene of concentration c and pathlength l is given by

$$J = J_0 \exp(-\sigma cl) \approx J_0(1 - \sigma cl)$$

and the rate of C_{60} ionization $k = J_0 - J = J_0(\sigma cl)$. Taking $l=1$ mm, the width of the volume probed by laser, gives $k = 3 \cdot 10^{-3} J_0$. The electron current density emitted by a heated filament is described by the following expression [97]

$$J = AT^2 \exp\left(\frac{-E_w}{kT}\right)$$

where A is material constant (60 amps/ cm^2K^2 for tungsten) and E_w is thermionic work function (about 4.5 eV for tungsten). According to this formula, a 3 cm long tungsten filament with a diameter of 0.2 mm heated to 2700 K will generate 0.3 A current. Actual emission current, however, is much lower as most of the electrons are stopped by the molybdenum tube acting as a Wehnelt shield. The typical values for thorium-coated tungsten filament (Thorium coating reduces E_w down to 2.6 eV) range from 10 to 80 mA. The current of 10 mA corresponds to $I_0 = 6 \cdot 10^{16} \text{ s}^{-1}$ and thus $k = 2 \cdot 10^{14} \text{ s}^{-1}$. Assuming that the electron beam is focused to 1 mm at the optical axis of the spectrometer and taking into account the fullerene molecules leave the active space at the speed of 130 m/s, the stationary concentration of C_{60}^+ ions can be estimated as $1 \cdot 10^{12} \text{ cm}^{-3}$. Cavity ringdown spectroscopy is capable of detecting moderately absorbing species at concentrations down to 10^{10} cm^{-3} [98] so the described method can indeed provide detectable amounts of C_{60}^+ ions. However, the internal temperature of molecules coming out of the effusive source is equal to the temperature inside the source so the electronic absorption bands of fullerene would be very broad due to the excitation of highly energetic rotational and vibrational movement.

The scheme of the designed source is shown on Figure 38. The one-piece copper body consists of the heating chamber and the slit opening. The oven is wound with a heating wire, which is shielded with a steel cylinder to minimize heat dissipation. An argon flow through the oven brings the fullerene vapor to the slit. The slit is formed by two steel blades placed to make an opening of precisely 100 μm .

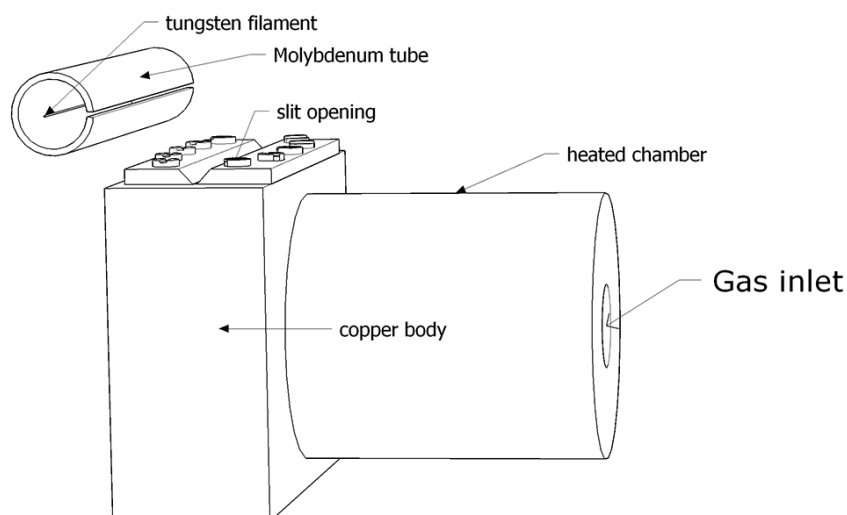


Figure 38. The scheme of the effusive source for producing C_{60}^+ ions.

A thermocouple is mounted near the slit opening to monitor the temperature of the exit orifice. During the initial tests, the source could be heated up to 850 K by applying ~ 110 V to the heating wire. The design of the electron impact source was taken from the work by Ruchti et al. [99] without any alteration. A tungsten filament is placed inside a slotted molybdenum tube, both of them kept as the same potential. Emitting electrons are thus accelerated thorough the slit towards the C_{60} beam. The production of ions is monitored by the mass spectrometer. At the present step, however, no signs of electron impact ionization have been observed due to unresolved technical problems and no further progress has been made yet on gas-phase detection of C_{60}^+ .

BIBLIOGRAPHY

1. Heger, M.L., *Further study of the sodium lines in class B stars; The spectra of certain class B stars in the regions 5630A-6680A and 3280A-3380A; Note on the spectrum of γ Cassiopeiae between 5860A and 6600A*. Lick Observatory bulletin, 1922(337): p. 141-148.
2. Merrill, P.W., *Unidentified interstellar lines*. Publications of the Astronomical Society of the Pacific, 1934. **46**(272): p. 206-207.
3. Herbig, G.H., *The Diffuse Interstellar Bands*. Annual Review of Astronomy and Astrophysics, 1995. **33**: p. 19-73.
4. Snow, T.P. and A.N. Witt, *The interstellar carbon budget and the role of carbon in dust and large molecules*. Science, 1995. **270**(5241): p. 1455-1460.
5. Cardelli, J.A., et al., *The abundance of interstellar carbon*. Astrophysical Journal, 1996. **467**(1): p. 334-340.
6. Wooten, A., *The 129 reported interstellar and circumstellar molecules*. . 2005: <http://www.cv.nrao.edu/~awooten/allmols.html>.
7. Vandishoeck, E.F. and J.H. Black, *Comprehensive models of diffuse interstellar clouds - physical conditions and molecular abundances*. Astrophysical Journal Supplement Series, 1986. **62**(1): p. 109-145.
8. Zsargo, J. and S.R. Federman, *Nonthermal chemistry in diffuse clouds with low molecular abundances*. Astrophysical Journal, 2003. **589**(1): p. 319-337.
9. Lucas, R. and H.S. Liszt, *Comparative chemistry of diffuse clouds - III. Sulfur-bearing molecules*. Astronomy & Astrophysics, 2002. **384**(3): p. 1054-1061.
10. Black, J.H. and A. Dalgarno, *Models of Interstellar clouds .1. ζ -Ophiuchi cloud*. Astrophysical Journal Supplement Series, 1977. **34**(3): p. 405-423.
11. Herbst, E. and Klemperer, W., *Formation and depletion of molecules in dense interstellar clouds*. Astrophysical Journal, 1973. **185**(2): p. 505-533.
12. Stein, S.E. and A. Fahr, *High-temperature stabilities of hydrocarbons*. Journal of Physical Chemistry, 1985. **89**(17): p. 3714-3725.
13. Bell, M.B., et al., *Detection of HC₁₁N in Irc+10-Degrees 216*. Nature, 1982. **295**(5848): p. 389-391.
14. Avery, L.W., et al., *Detection of heavy interstellar molecule cyanodiacetylene*. Astrophysical Journal, 1976. **205**(3): p. L173-L175.

15. Kroto, H.W., et al., *Detection of cyanoacetylene, $H(C\equiv C)_3C_n$, in Heiles Cloud 2*. *Astrophysical Journal*, 1978. **219**(3): p. L133-L137.
16. Broten, N.W., et al., *Detection of HC_9N in interstellar space*. *Astrophysical Journal*, 1978. **223**(2): p. L105-L107.
17. Kroto, H.W., *The chemistry of the interstellar medium*. *Philosophical Transactions of the Royal Society of London Series A. Mathematical Physical and Engineering Sciences*, 1988. **325**(1587): p. 405-421.
18. Duley, W.W., A.P. Jones, and D.A. Williams, *Hydrogenated amorphous carbon-coated silicate particles as a source of interstellar extinction*. *Monthly Notices of the Royal Astronomical Society*, 1989. **236**(3): p. 709-725.
19. Robertson, J. and E.P. Oreilly, *Electronic and atomic structure of amorphous carbon*. *Physical Review B*, 1987. **35**(6): p. 2946-2957.
20. Hall, P. and D.A. Williams, *Polyatomic molecules in diffuse clouds*. *Astrophysics and Space Science*, 1995. **229**(1): p. 49-61.
21. Lepp, S., et al., *Large molecules in diffuse interstellar clouds*. *Astrophysical Journal*, 1988. **329**(1): p. 418-424.
22. Frenklach, M. and E.D. Feigelson, *Formation of polycyclic aromatic-hydrocarbons in circumstellar envelopes*. *Astrophysical Journal*, 1989. **341**(1): p. 372-384.
23. Westmoreland, P.R., et al., *Forming benzene in flames by chemically activated isomerization*. *Journal of Physical Chemistry*, 1989. **93**(25): p. 8171-8180.
24. Thomson, J.J., *Bakerian lecture: Rays of positive electricity*. *Proceedings of the Royal Society of London Series a-Containing Papers of a Mathematical and Physical Character*, 1913. **89**(607): p. 1.
25. Nier, A.O., *A mass spectrometer for isotope and gas analysis*. *Review of Scientific Instruments*, 1947. **18**(6): p. 398-411.
26. Wiley, W.C. and I.H. McLaren, *Time-of-Flight mass spectrometer with improved resolution*. *Review of Scientific Instruments*, 1955. **26**(12): p. 1150-1157.
27. Friedburg, H. and W. Paul, *Optische abbildung mit neutralen atomen*. *Naturwissenschaften*, 1951. **38**(7): p. 159-160.
28. March, R.E., *An introduction to quadrupole ion trap mass spectrometry*. *Journal of Mass Spectrometry*, 1997. **32**(4): p. 351-369.
29. Motylewsky, T., *Cavity ringdown spectroscopy of transient species*, in *Department of Chemistry*. 2001, Basel University: Basel.

30. Okeefe, A. and D.A.G. Deacon, *Cavity Ring-down Optical Spectrometer for Absorption-Measurements Using Pulsed Laser Sources*. Review of Scientific Instruments, 1988. **59**(12): p. 2544-2551.
31. Davis, S., et al., *Jet-cooled molecular radicals in slit supersonic discharges: Sub-Doppler infrared studies of methyl radical*. Journal of Chemical Physics, 1997. **107**(15): p. 5661-5675.
32. *Communication protocol for quadrupole mass spectrometer system QMG 422*, Balzers Instruments.
33. Engelking, P.C., *Corona excited supersonic expansion*. Review of Scientific Instruments, 1986. **57**(9): p. 2274-2277.
34. Motylewski, T. and H. Linnartz, *Cavity ring down spectroscopy on radicals in a supersonic slit nozzle discharge*. Review of Scientific Instruments, 1999. **70**(2): p. 1305-1312.
35. Broks, B.H.P., et al., *Numerical investigation of the discharge characteristics of the pulsed discharge nozzle*. Physical Review E, 2005. **71**(3): p. -.
36. Witkowicz, E., et al., *Mass spectrometric and laser spectroscopic characterization of a supersonic planar plasma expansion*. International Journal of Mass Spectrometry, 2004. **232**(1): p. 25-29.
37. Pfluger, D., et al., *Rotationally resolved electronic absorption spectra of triacetylene cation in a supersonic jet*. Chemical Physics Letters, 1999. **313**(1-2): p. 171-178.
38. Pfluger, D., et al., *Rotationally resolved $A^2\Pi_u \leftarrow X^2\Pi_g$ electronic spectrum of tetraacetylene cation*. Chemical Physics Letters, 2000. **329**(1-2): p. 29-35.
39. Cias, P., et al., *Electronic gas-phase spectrum of the pentaacetylene cation*. Journal of Physical Chemistry A, 2002. **106**(42): p. 9890-9892.
40. Araki, M., et al., *High-resolution electronic spectroscopy of a nonlinear carbon chain radical $C_6H_4^+$* . Journal of Chemical Physics, 2003. **118**(23): p. 10561-10565.
41. Ball, C.D., M.C. McCarthy, and P. Thaddeus, *Laboratory detection of a molecular band at lambda 4429*. Astrophysical Journal, 2000. **529**(1): p. L61-L64.
42. Araki, M., et al., *New laboratory data on a molecular band at 4429 angstrom*. Astrophysical Journal, 2004. **616**(2): p. 1301-1310.
43. Nakajima, M., Y. Sumiyoshi, and Y. Endo, *Laser induced fluorescence spectroscopy of the HC_4S and DC_4S radicals*. Chemical Physics Letters, 2002. **351**(5-6): p. 359-364.
44. Nakajima, M., Y. Sumiyoshi, and Y. Endo, *Laser induced fluorescence spectroscopy of the HC_6S radical*. Chemical Physics Letters, 2002. **355**(1-2): p. 116-122.

45. Nakajima, M., et al., *Laser-induced fluorescence and fluorescence depletion spectroscopy of SCCS*. Journal Of Chemical Physics, 2003. **119**(15): p. 7805-7813.
46. Gordon, V.D., et al., *Rotational spectra of sulfur-carbon chains. II. HC₅S, HC₆S, HC₇S, and HC₈S, and H₂C₄S, H₂C₅S, H₂C₆S, and H₂C₇S*. Astrophysical Journal Supplement Series, 2002. **138**(2): p. 297-303.
47. Hirahara, Y., Y. Ohshima, and Y. Endo, *Pulsed-discharge-nozzle Fourier-transform microwave spectroscopy of HC₃S(²Π_r) and HC₄S(²Π_i)*. Journal Of Chemical Physics, 1994. **101**(9): p. 7342-7349.
48. Gordon, V.D., et al., *Rotational spectra of sulfur-carbon chains. I. The radicals C₄S, C₅S, C₆S, C₇S, C₈S, and C₉S*. Astrophysical Journal Supplement Series, 2001. **134**(2): p. 311-317.
49. Samant, M.G., C.A. Brown, and J.G. Gordon, *Formation of an ordered self-assembled monolayer of docosaneselenol on gold(111) - structure by surface X-ray diffraction*. Langmuir, 1992. **8**(6): p. 1615-1618.
50. Reed, M.A., et al., *Conductance of a molecular junction*. Science, 1997. **278**(5336): p. 252-254.
51. Mujica, V., et al., *Molecular wire junctions: Tuning the conductance*. Journal Of Physical Chemistry B, 2003. **107**(1): p. 91-95.
52. Millar, T.J., J.R. Flores, and A.J. Markwick, *Sulphur-bearing carbon chains in IRC+10216*. Monthly Notices Of The Royal Astronomical Society, 2001. **327**(4): p. 1173-1177.
53. Bell, M.B., L.W. Avery, and P.A. Feldman, *C₃S And C₅S In Irc+10216*. Astrophysical Journal, 1993. **417**(1): p. L37-L40.
54. Cernicharo, J., et al., *Sulfur in Irc+10216*. Astronomy and Astrophysics, 1987. **181**(1): p. L9-L12.
55. Kirkwood, D.A., et al., *Electronic spectra of carbon chain anions: C_{2n}H⁻ (n=5-12)*. Journal Of Chemical Physics, 1999. **111**(20): p. 9280-9286.
56. Pino, T., et al., *Electronic spectra of the chains HC_{2n}H (n=8-13) in the gas phase*. Journal of Chemical Physics, 2001. **114**(5): p. 2208-2212.
57. McCarthy, M.C. and P. Thaddeus, *Microwave and laser spectroscopy of carbon chains and rings*. Chemical Society Reviews, 2001. **30**(3): p. 177-185.
58. Van Orden, A. and R.J. Saykally, *Small carbon clusters: Spectroscopy, structure, and energetics*. Chemical Reviews, 1998. **98**(6): p. 2313-2357.

59. Maier, J.P., *Electronic spectroscopy of carbon chains*. Journal of Physical Chemistry A, 1998. **102**(20): p. 3462-3469.
60. McCarthy, M., et al., *Laboratory detection of the carbon chains HC₁₅N and HC₁₇N*. Astrophysical Journal, 1998. **494**(2): p. L231-L234.
61. Martin, J.M.L., et al., *Structure and infrared-spectroscopy of the C₁₁ molecule*. Chemical physics letters, 1991. **187**(4): p. 367-374.
62. Giesen, T.F., et al., *Infrared-laser spectroscopy of the linear C₁₃ carbon cluster*. Science, 1994. **265**(5173): p. 756-759.
63. Thaddeus, P. and M.C. McCarthy, *Carbon chains and rings in the laboratory and in space*. Spectrochimica Acta Part a-Molecular and Biomolecular Spectroscopy, 2001. **57**(4): p. 757-774.
64. Vanderhart, W.J., et al., *Photodissociation and structures of C₆H₄⁺ ions generated from cyanobenzene and other precursors*. Organic Mass Spectrometry, 1989. **24**(1): p. 59-62.
65. Arrington, C., et al., *Ultraviolet photochemistry of diacetylene with alkynes and alkenes: Spectroscopic characterization of the products*. Journal Of Physical Chemistry A, 1999. **103**(10): p. 1294-1299.
66. Luckhaus, D. and M. Quack, *The far infrared pure rotational spectrum and the coriolis coupling between ν_3 and ν_8 in CH³⁵ClF₂*. Molecular Physics, 1989. **68**(3): p. 745-758.
67. McCarthy, M., et al., *Eight new carbon chain molecules*. Astrophysical Journal Supplement Series, 1997. **113**(1): p. 105-120.
68. Garforth, F.M., C.K. Ingold, and H.G. Poole, *Excited states of benzene. 12. The effect of an electronic excitation on the geometry, elastic properties, and zero-point energy of the benzene molecule and the effect of isotopic substitution on the transition energy*. Journal Of The Chemical Society, 1948(APR): p. 508-517.
69. Stewart, J.J.P., *MOPAC 1990*. p. semiempirical molecular orbital program.
70. Schmidt, M.W., et al., *General atomic and molecular electronic structure system*. Journal Of Computational Chemistry, 1993. **14**(11): p. 1347-1363.
71. Koster, G. and W.J. van der Hart, *Ab initio calculations on the isomerization of C₄H₄ radical cations*. International Journal Of Mass Spectrometry And Ion Processes, 1997. **163**(3): p. 169-175.
72. Freivogel, P., et al., *Absorption spectra of conjugated hydrocarbon cation chains in neon matrices*. Chemical Physics, 1994. **189**(2): p. 335-341.
73. Gottlieb, C., et al., *The rotational spectra of the HCCCNH⁺, NCCNH⁺, and CH₃CNH⁺ ions*. Journal of Chemical Physics, 2000. **113**(5): p. 1910-1915.

74. Jenniskens, P. and F.X. Desert, *A survey of diffuse interstellar bands (3800-8680 Angstrom)*. Astronomy & Astrophysics Supplement Series, 1994. **106**(1): p. 39-78.
75. Tuairisg, S.O., et al., *A deep echelle survey and new analysis of diffuse interstellar bands*. Astronomy & Astrophysics Supplement Series, 2000. **142**(2): p. 225-238.
76. Lecoultre, J., J.P. Maier, and M. Rosslein, *Geometric structure of diacetylene cation in the $X^2\Pi_g$ and $A^2\Pi_u$ electronic states*. Journal Of Chemical Physics, 1988. **89**(10): p. 6081-6085.
77. Sinclair, W.E., et al., *Rotationally resolved $A^2\Pi_g$ - $X^2\Pi_u$ electronic spectrum of triacetylene cation by frequency modulation absorption spectroscopy*. Journal of Chemical Physics, 1999. **110**(1): p. 296-303.
78. Linnartz, H., T. Motylewski, and J.P. Maier, *The $^2\Pi \leftarrow X^2\Pi$ electronic spectra of C_8H and $C_{10}H$ in the gas phase*. Journal of Chemical Physics, 1998. **109**(10): p. 3819-3823.
79. Douglas, A.E., *Origin of diffuse interstellar lines*. Nature, 1977. **269**(5624): p. 130-132.
80. Wrobel, R., et al., *Photochemistry of butatriene - Spectroscopic evidence for the existence of allenylcarbene*. Journal Of Physical Chemistry A, 2000. **104**(16): p. 3819-3825.
81. Maier, J.P., *Electronic spectroscopy of carbon chains*. Chemical Society Reviews, 1997. **26**(1): p. 21-28.
82. Lloyd, G.M. and P. Ewart, *High resolution spectroscopy and spectral simulation of C_2 using degenerate four-wave mixing*. Journal Of Chemical Physics, 1999. **110**(1): p. 385-392.
83. Motylewski, T., et al., *Gas-phase electronic spectra of carbon-chain radicals compared with diffuse interstellar band observations*. Astrophysical Journal, 2000. **531**(1): p. 312-320.
84. Shnitko, I., et al., *$^3\Sigma^- \leftarrow X^3\Sigma^-$ electronic transition of linear C_6H^+ and C_8H^+ in neon matrixes*. Journal of Physical Chemistry A, 2006. **110**(9): p. 2885-2889.
85. Western, C.M., *PGOPHER, a program for simulating rotational structure*, University of Bristol, <http://pgopher.chm.bris.ac.uk>.
86. Linnartz, H., et al., *Electronic ground and excited state spectroscopy of C_6H and C_6D* . Journal of Molecular Spectroscopy, 1999. **197**(1): p. 1-11.
87. Motylewski, T., et al., *The $^1\Pi_u \leftarrow X^1\Sigma^{+g}$ electronic spectrum of C_5 in the gas phase*. Journal of Chemical Physics, 1999. **111**(14): p. 6161-6163.

88. Birza, P., *Development of a cw-cavity ring down spectrometer and electronic spectroscopy of transient species*, in *Department of Chemistry*. 2004, Basel University: Basel.
89. Hanrath, M. and S.D. Peyerimhoff, *The electronic spectrum of C₅*. *Chemical Physics Letters*, 2001. **337**(4-6): p. 368-374.
90. Fulara, J., M. Jakobi, and J.P. Maier, *Electronic and infrared spectra of C₆₀⁺ And C₆₀⁻ in neon and argon matrices*. *Chemical Physics Letters*, 1993. **211**(2-3): p. 227-234.
91. Foing, B.H. and P. Ehrenfreund, *Detection of 2 interstellar absorption bands coincident with spectral features of C₆₀⁺*. *Nature*, 1994. **369**(6478): p. 296-298.
92. Galazutdinov, G.A., et al., *On the identification of the C₆₀⁺ interstellar features*. *Monthly Notices Of The Royal Astronomical Society*, 2000. **317**(4): p. 750-758.
93. Kroto, H.W., et al., *C₆₀ – Buckminsterfullerene*. *Nature*, 1985. **318**(6042): p. 162-163.
94. Matsumoto, K., E. Schonherr, and M. Wojnowski, *Growth of C₆₀ crystals by the Pizzarello method*. *Journal Of Crystal Growth*, 1994. **135**(1-2): p. 154-156.
95. Pauly, H., in *Atomic and Molecular Beam Methods*, H. Scoles, Editor. 1988, Oxford University Press: Oxford. p. 83.
96. Itoh, A., et al., *Ionization cross sections of C₆₀ by fast electron impact*. *Journal Of Physics B-Atomic Molecular And Optical Physics*, 1999. **32**(2): p. 277-286.
97. Ehlers, K.W. and K.N. Leung, *Some characteristics of tungsten filaments operated as cathodes in a gas discharge*. *Review of Scientific Instruments*, 1979. **50**(3): p. 356-361.
98. Berden, G., R. Peeters, and G. Meijer, *Cavity ring-down spectroscopy: Experimental schemes and applications*. *International Reviews in Physical Chemistry*, 2000. **19**(4): p. 565-607.
99. Ruchti, T., et al., *An electron impact ionization slit-jet apparatus for laser absorption spectroscopy*. *Chemical Physics*, 1996. **209**(2-3): p. 169-175.

APPENDIX A. ROTATIONAL LINES ASSIGNMENT

Table 9. Assigned rotational lines of a P-branch of ${}^2A''\text{-}X^2A''$ electronic transition of C_6H_4^+ , the frequencies are given in cm^{-1} . Several rotational transitions can contribute to one line in the spectrum due to limited resolution.

N'	K_a'	K_c'		N''	K_a''	K_c''	Observed	Calculated	Obs-Calc
4	0	4	-	5	0	5	16544.456	16544.475	-0.019
5	0	5	-	6	0	6	16544.355	16544.368	-0.013
5	1	4	-	6	1	5	16544.456	16544.440	0.016
5	1	5	-	6	1	6	16544.456	16544.452	0.005
6	0	6	-	7	0	7	16544.227	16544.258	-0.030
6	1	5	-	7	1	6	16544.355	16544.329	0.027
6	1	6	-	7	1	7	16544.355	16544.342	0.013
7	1	6	-	8	1	7	16544.227	16544.214	0.013
7	1	7	-	8	1	8	16544.227	16544.230	-0.003
7	2	5	-	8	2	6	16544.456	16544.456	0.001
7	2	6	-	8	2	7	16544.456	16544.456	0.000
8	1	7	-	9	1	8	16544.099	16544.097	0.002
8	1	8	-	9	1	9	16544.099	16544.115	-0.016
8	2	6	-	9	2	7	16544.355	16544.339	0.016
8	2	7	-	9	2	8	16544.355	16544.339	0.016
9	1	8	-	10	1	9	16543.968	16543.976	-0.008
9	1	9	-	10	1	10	16543.968	16543.997	-0.029
9	2	7	-	10	2	8	16544.227	16544.220	0.008
9	2	8	-	10	2	9	16544.227	16544.220	0.007
10	1	9	-	11	1	10	16543.837	16543.852	-0.015
10	1	10	-	11	1	11	16543.837	16543.876	-0.038
10	2	8	-	11	2	9	16544.099	16544.097	0.002
10	2	9	-	11	2	10	16544.099	16544.098	0.001
11	0	11	-	12	0	12	16543.660	16543.661	-0.001
11	1	10	-	12	1	11	16543.707	16543.726	-0.018

N'	K_a'	K_c'		N''	K_a''	K_c''	Observed	Calculated	Obs-Calc
11	2	9	-	12	2	10	16543.968	16543.971	-0.004
11	2	10	-	12	2	11	16543.968	16543.972	-0.005
11	3	8	-	12	3	9	16544.355	16544.361	-0.006
11	3	9	-	12	3	10	16544.355	16544.361	-0.006
12	1	11	-	13	1	12	16543.564	16543.596	-0.032
12	2	10	-	13	2	11	16543.837	16543.843	-0.005
12	2	11	-	13	2	12	16543.837	16543.844	-0.006
12	3	9	-	13	3	10	16544.227	16544.233	-0.005
12	3	10	-	13	3	11	16544.227	16544.233	-0.005
13	1	12	-	14	1	13	16543.441	16543.463	-0.022
13	2	11	-	14	2	12	16543.707	16543.711	-0.003
13	2	12	-	14	2	13	16543.707	16543.712	-0.005
13	3	10	-	14	3	11	16544.099	16544.101	-0.002
13	3	11	-	14	3	12	16544.099	16544.101	-0.002
14	0	14	-	15	0	15	16543.263	16543.267	-0.005
14	2	12	-	15	2	13	16543.564	16543.576	-0.012
14	2	13	-	15	2	14	16543.564	16543.577	-0.013
14	3	11	-	15	3	12	16543.968	16543.966	0.001
14	3	12	-	15	3	13	16543.968	16543.966	0.001
15	2	13	-	16	2	14	16543.441	16543.438	0.003
15	2	14	-	16	2	15	16543.441	16543.440	0.001
15	3	12	-	16	3	13	16543.837	16543.829	0.009
15	3	13	-	16	3	14	16543.837	16543.829	0.009
16	0	16	-	17	0	17	16543.017	16542.990	0.027
16	3	13	-	17	3	14	16543.707	16543.688	0.020
16	3	14	-	17	3	15	16543.707	16543.688	0.020
16	4	12	-	17	4	13	16544.227	16544.233	-0.006
16	4	13	-	17	4	14	16544.227	16544.233	-0.006
17	0	17	-	18	0	18	16542.846	16542.846	0.000
17	2	15	-	18	2	16	16543.168	16543.152	0.015
17	2	16	-	18	2	17	16543.168	16543.155	0.012

N'	K_a'	K_c'		N''	K_a''	K_c''	Observed	Calculated	Obs-Calc
17	4	13	-	18	4	14	16544.099	16544.089	0.010
17	4	14	-	18	4	15	16544.099	16544.089	0.010
18	0	18	-	19	0	19	16542.695	16542.700	-0.005
18	2	16	-	19	2	17	16543.017	16543.005	0.012
18	2	17	-	19	2	18	16543.017	16543.009	0.008
18	4	14	-	19	4	15	16543.968	16543.942	0.025
18	4	15	-	19	4	16	16543.968	16543.942	0.025
19	0	19	-	20	0	20	16542.538	16542.551	-0.013
19	2	17	-	20	2	18	16542.846	16542.855	-0.008
19	2	18	-	20	2	19	16542.846	16542.859	-0.013
19	3	16	-	20	3	17	16543.263	16543.247	0.016
19	3	17	-	20	3	18	16543.263	16543.247	0.016
20	0	20	-	21	0	21	16542.386	16542.399	-0.013
20	2	18	-	21	2	19	16542.695	16542.701	-0.006
20	2	19	-	21	2	20	16542.695	16542.706	-0.011
20	4	16	-	21	4	17	16543.660	16543.639	0.021
20	4	17	-	21	4	18	16543.660	16543.639	0.021
21	0	21	-	22	0	22	16542.223	16542.244	-0.021
21	1	20	-	22	1	21	16542.277	16542.289	-0.011
21	2	19	-	22	2	20	16542.538	16542.544	-0.006
21	2	20	-	22	2	21	16542.538	16542.550	-0.012
22	0	22	-	23	0	23	16542.070	16542.085	-0.016
22	2	20	-	23	2	21	16542.386	16542.384	0.001
22	2	21	-	23	2	22	16542.386	16542.391	-0.005
23	0	23	-	24	0	24	16541.894	16541.924	-0.030
23	2	21	-	24	2	22	16542.223	16542.221	0.001
23	2	22	-	24	2	23	16542.223	16542.229	-0.007
24	0	24	-	25	0	25	16541.764	16541.761	0.004
24	2	22	-	25	2	23	16542.070	16542.055	0.014
24	2	23	-	25	2	24	16542.070	16542.064	0.005
25	0	25	-	26	0	26	16541.588	16541.594	-0.005

N'	K_a'	K_c'		N''	K_a''	K_c''	Observed	Calculated	Obs-Calc
25	1	25	-	26	1	26	16541.720	16541.699	0.021
25	2	23	-	26	2	24	16541.894	16541.886	0.008
25	2	24	-	26	2	25	16541.894	16541.896	-0.002
25	3	22	-	26	3	23	16542.277	16542.283	-0.005
25	3	23	-	26	3	24	16542.277	16542.283	-0.006
26	0	26	-	27	0	27	16541.415	16541.424	-0.009
26	2	24	-	27	2	25	16541.720	16541.714	0.006
26	2	25	-	27	2	26	16541.720	16541.726	-0.006
27	1	27	-	28	1	28	16541.387	16541.358	0.029
28	0	28	-	29	0	29	16541.056	16541.076	-0.020
28	1	28	-	29	1	29	16541.195	16541.183	0.011
28	2	26	-	29	2	27	16541.387	16541.359	0.028
28	2	27	-	29	2	28	16541.387	16541.374	0.013
28	3	25	-	29	3	26	16541.764	16541.759	0.005
28	3	26	-	29	3	27	16541.764	16541.760	0.005
29	1	29	-	30	1	30	16541.004	16541.006	-0.001
29	2	27	-	30	2	28	16541.195	16541.177	0.017
29	2	28	-	30	2	29	16541.195	16541.194	0.000
30	1	30	-	31	1	31	16540.826	16540.825	0.002
30	2	28	-	31	2	29	16541.004	16540.992	0.012
30	2	29	-	31	2	30	16541.004	16541.011	-0.007
31	2	29	-	32	2	30	16540.826	16540.804	0.022
31	2	30	-	32	2	31	16540.826	16540.825	0.001
31	3	28	-	32	3	29	16541.195	16541.208	-0.013
31	3	29	-	32	3	30	16541.195	16541.209	-0.014
33	0	33	-	34	0	34	16540.128	16540.154	-0.027
33	1	32	-	34	1	33	16540.128	16540.161	-0.034

Table 10. Measured rotational line frequencies of C₆H.

Branch	J'	J''	Observed	Calculated	$\Delta(\text{Obs-Calc})$
$^2\Pi_{3/2}-^2\Pi_{3/2}$ electronic transition					
Q	3/2	3/2	19424.57	19424.57	0.00
P	3/2	5/2	19424.35	19424.34	0.01
P	5/2	7/2	19424.25	19424.25	0.00
P	7/2	9/2	19424.22	19424.16	0.06
P	9/2	11/2	19424.10	19424.06	0.04
P	11/2	13/2	19423.97	19423.97	0.00
P	17/2	19/2	19423.71	19423.68	0.03
P	19/2	21/2	19423.59	19423.59	0.01
P	21/2	23/2	19423.47	19423.49	-0.02
P	27/2	29/2	19423.26	19423.20	0.05
P	29/2	31/2	19423.15	19423.11	0.05
P	31/2	33/2	19423.04	19423.01	0.03
P	33/2	35/2	19422.94	19422.91	0.03
P	37/2	39/2	19422.75	19422.72	0.03
P	43/2	45/2	19422.45	19422.42	0.03
P	45/2	47/2	19422.35	19422.32	0.02
P	53/2	55/2	19421.98	19421.92	0.05
P	55/2	57/2	19421.86	19421.82	0.04
P	57/2	59/2	19421.74	19421.72	0.02
P	67/2	69/2	19421.24	19421.21	0.03
R	5/2	3/2	19424.79	19424.80	-0.02
R	7/2	5/2	19424.88	19424.90	-0.01
R	15/2	13/2	19425.25	19425.26	-0.01
R	17/2	15/2	19425.31	19425.35	-0.03
R	21/2	19/2	19425.52	19425.53	-0.01
R	23/2	21/2	19425.60	19425.62	-0.02

Branch	J'	J''	Observed	Calculated	$\Delta(\text{Obs-Calc})$
${}^2\Pi_{1/2}-{}^2\Pi_{1/2}$ electronic transition					
P	1/2	3/2	19433.11	19433.08	0.02
P	3/2	5/2	19433.00	19432.99	0.02
P	5/2	7/2	19432.91	19432.89	0.01
P	11/2	13/2	19432.62	19432.61	0.01
P	13/2	15/2	19432.51	19432.51	0.00
P	15/2	17/2	19432.39	19432.41	-0.02
P	19/2	21/2	19432.24	19432.22	0.02
P	21/2	23/2	19432.08	19432.12	-0.04
P	23/2	25/2	19431.97	19432.02	-0.05

APPENDIX B. CONTROLLING THE QUADRUPOLE MASS SPECTROMETER IN LABVIEW

MassSpectr.vi
D:\QMS-operate\MassSpectr.vi
Last modified on 15/06/2006 at 15:58
Printed on 15/06/2006 at 16:21

DESCRIPTION:

This VI operates quadrupole mass spectrometer QMS 422 via standard ASCII RS-232-C protocol. The signal from the detector is counted by NI-TIO 6602 board which counts pulses on SOURCE pin during user-defined externally triggered gate signal.

INSTRUCTIONS:

1. Choose desired mass range and step of the scan.
2. Make your Gate selections, as desired.
3. Optional controls are hidden and can be found on diagram. You can need them for debugging this VI.
4. Run the VI.
5. Press save button to save your scan as XY pairs. The dialog window will appear after the scan is finished or interrupted.

I/O CONNECTIONS:

TTL pulses converter is connected to SOURCE 2 pin;
Discharge trigger pulse is connected to GATE1 pin;
OUT1 is connected to GATE2, this is actual GATE signal.

NOTE: For actual I/O pin numbers, please refer to your hardware user manual.

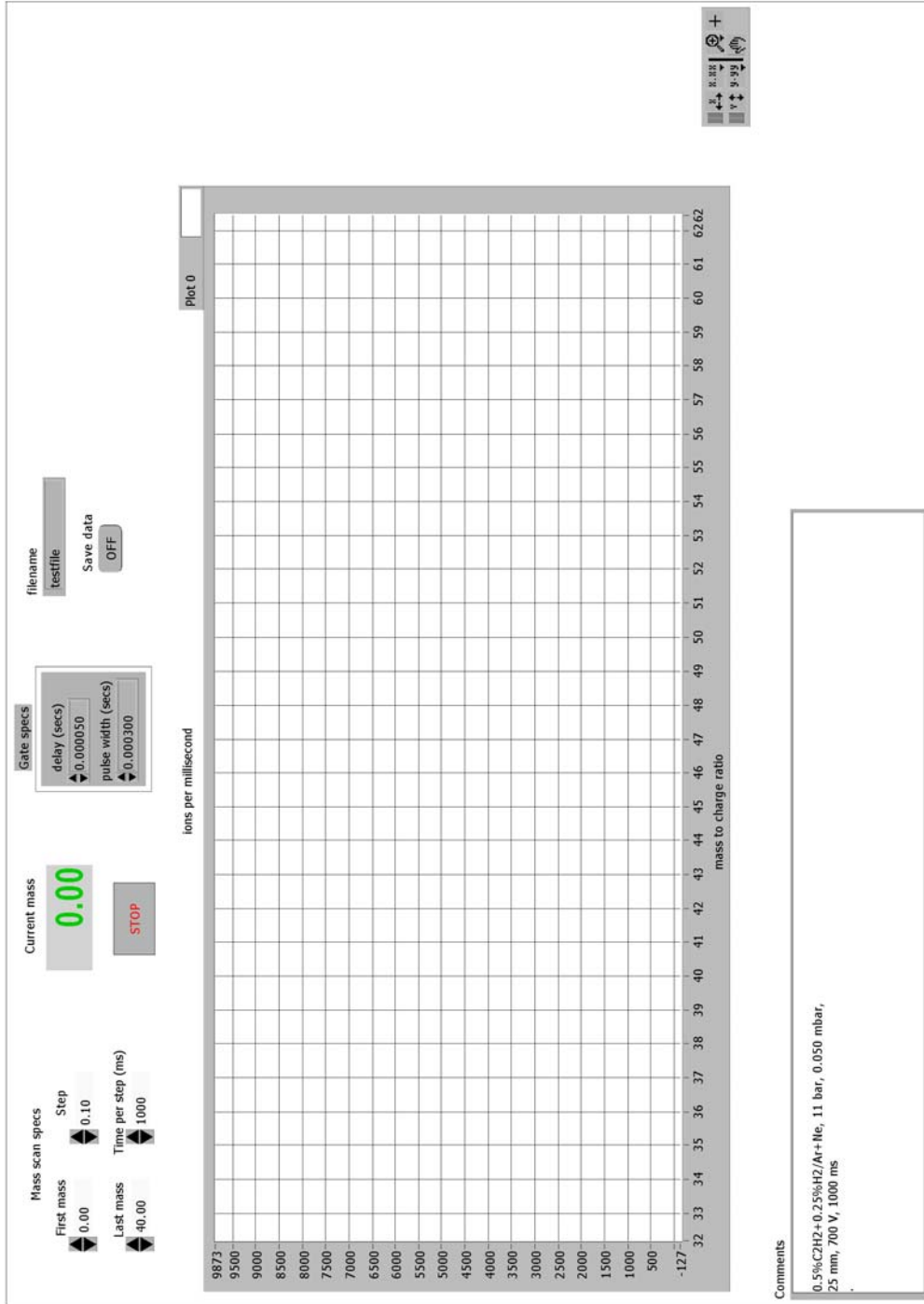
DAQ VIs USED:

Counter Group Config.vi
Counter Source (NI-TIO).vi
Counter Gate (NI-TIO).vi
Counter Get Attribute.vi
Counter Control.vi

Alexey Denisov, 2002
Institute for Physical Chemistry
University of Basel
Switzerland

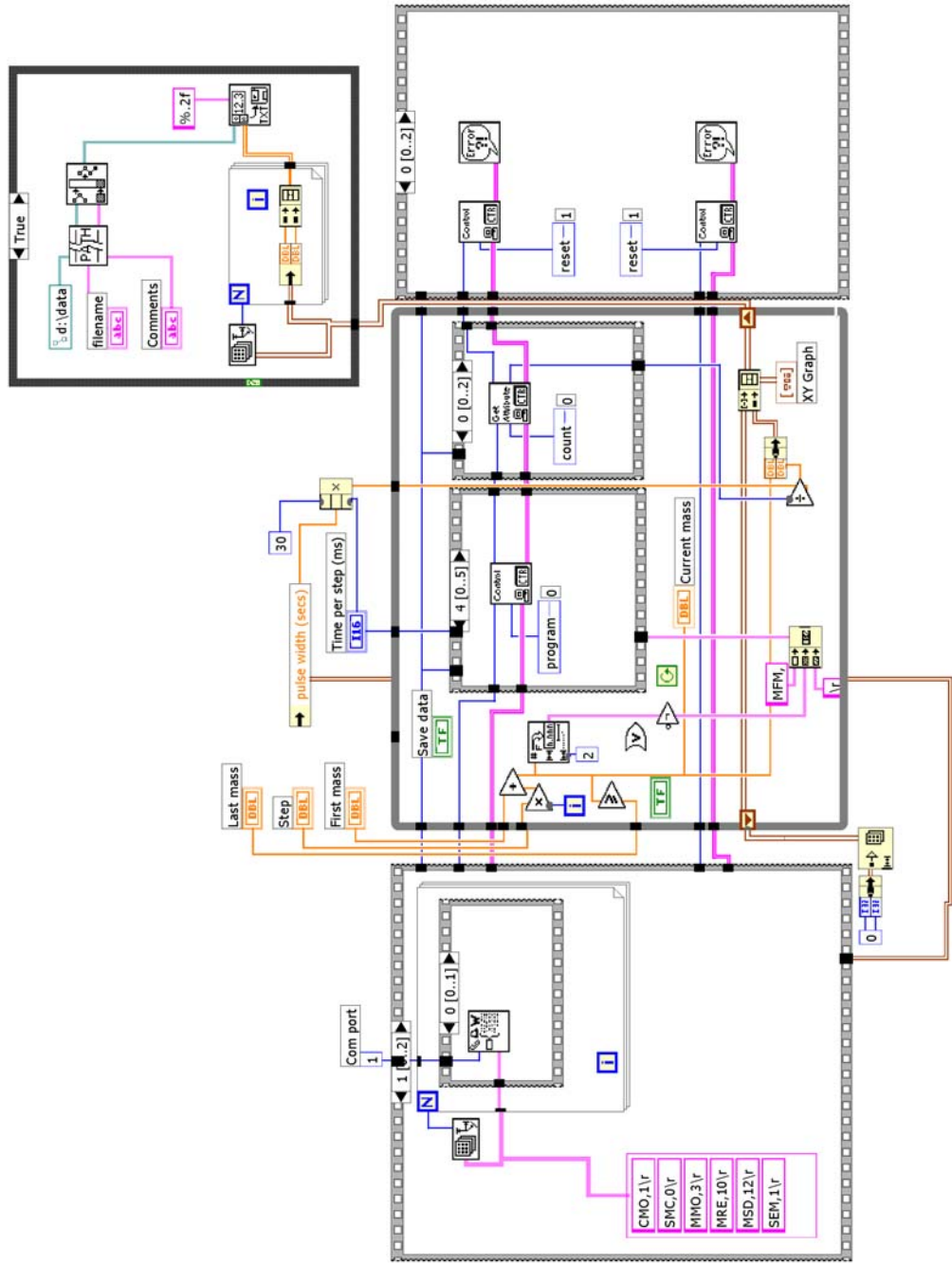
MassSpectr_print_friendly.vi
 D:\QMS-operate\MassSpectr_print_friendly.vi
 Last modified on 15/06/2006 at 15:58
 Printed on 15/06/2006 at 16:21

Front Panel

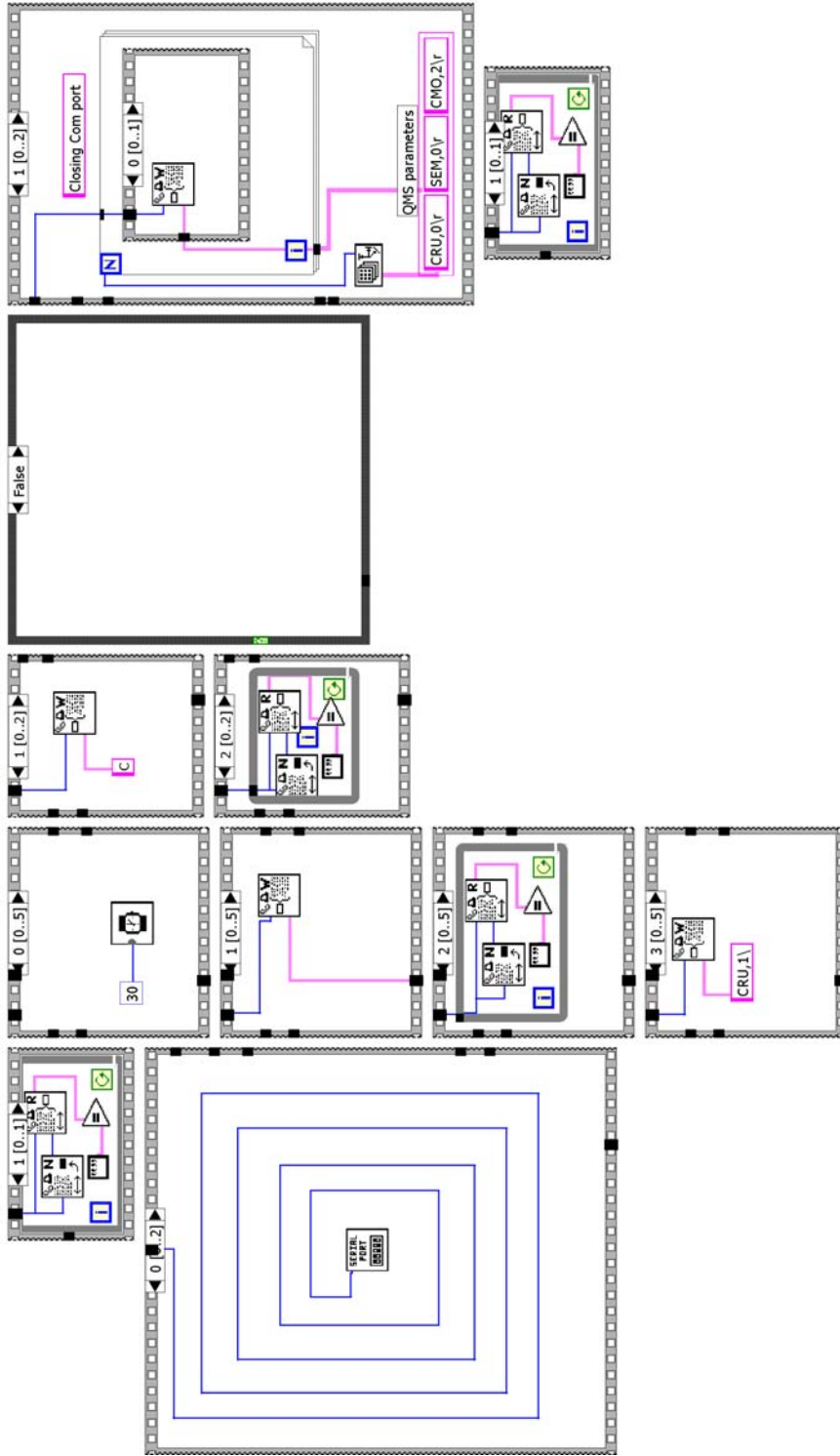


MassSpectr_print_friendly.vi
 D:\QMS-operate\MassSpectr_print_friendly.vi
 Last modified on 15/06/2006 at 15:58
 Printed on 15/06/2006 at 16:21

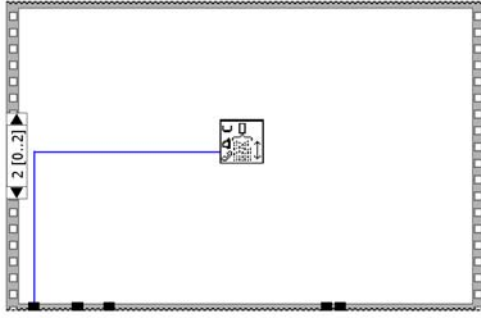
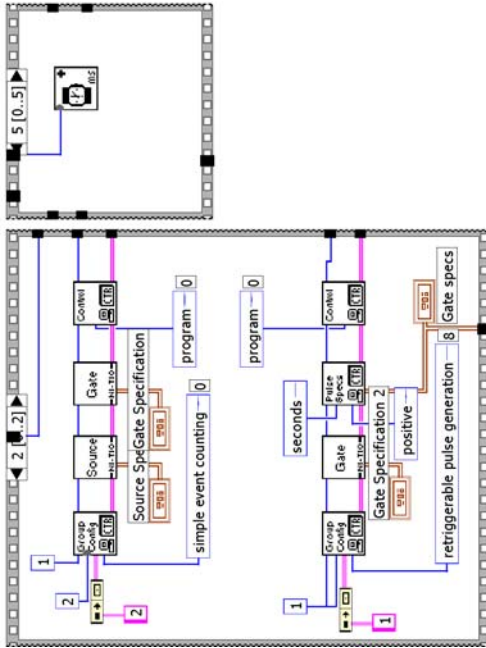
Block Diagram



MassSpectr_print_friendly.vi
D:\QMS-operate\MassSpectr_print_friendly.vi
Last modified on 15/06/2006 at 15:58
Printed on 15/06/2006 at 16:21



MassSpectr_print_friendly.vi
 D:\QMS-operate\MassSpectr_print_friendly.vi
 Last modified on 15/06/2006 at 15:58
 Printed on 15/06/2006 at 16:21



APPENDIX C. PUBLISHED PAPERS

Electronic Gas-Phase Spectrum of the Pentaacetylene Cation[†]

P. Cias, O. Vaizert, A. Denisov, J. Mes,[§] H. Linnartz,[#] and J. P. Maier*

Department of Chemistry, Klingelbergstrasse 80, CH 4056 Basel, Switzerland

Received: February 27, 2002; In Final Form: June 25, 2002

The origin band of the $A^2\Pi_u-X^2\Pi_g$ electronic transition of the linear pentaacetylene cation, $HC_{10}H^+$, and isotopic derivatives, $HC_{10}D^+$ and $DC_{10}D^+$, has been recorded in the gas phase. The absorption spectrum was observed by cavity ring down spectroscopy through a supersonic planar plasma expansion. The spectrum comprises both spin-orbit components with resolved P- and R-branches. Contour fits allow the determination of ground and excited state spectroscopic constants.

Introduction

The polyacetylene cations, HC_nH^+ , are open-shell species with a $^2\Pi$ ground state. The strong electronic transitions have $^2\Pi_u-X^2\Pi_g$ symmetry and shift to the red with increasing number of carbon atoms. Rotationally resolved electronic spectra have been recorded previously in the gas phase for the even members with $n = 2$ at 255.7 nm,¹ $n = 4$ at 507.0 nm,^{2,3} $n = 6$ at 600.4 nm,^{4,5} and $n = 8$ at 707.1 nm.⁶ Little is known on the next member in the series, the pentaacetylene cation $HC_{10}H^+$. Density functional theory calculations⁷ and ion chromatography⁸ predict a linear structure. It was shown that $HC_{10}H^+$ is formed in an ion trap upon collision activated processes on polycyclic aromatic hydrocarbons.⁹ Furthermore, this cation may be of interest from an astrophysical point of view. It has been argued that electronic transitions of carbon chains may be among the carriers of unidentified absorption features in diffuse interstellar clouds.¹⁰ Particularly longer chains are of interest as these are expected to be photo stable.

The first experimental observation of the $A^2\Pi_u-X^2\Pi_g$ electronic spectrum of $HC_{10}H^+$ was in a neon matrix using mass selective deposition;¹¹ the transition was found to comprise a strong origin band around 823.3 nm and a series of weaker bands corresponding to vibrational excitation in the upper electronic state. In the case of the smaller polyacetylene cations, the transitions in the gas phase are typically blue-shifted 100–130 cm^{-1} with respect to the matrix value, that is, the unperturbed origin band of $HC_{10}H^+$ is expected between 814.5 and 816.5 nm.

Experiment

The wavelength range around 815.5 nm was scanned using cavity ring down (CRD) spectroscopy. CRD has become a powerful tool for the study of the structural and dynamical properties of molecules in the gas phase.¹² One of the reasons for this success is the conceptual simplicity of a CRD experiment. A small fraction of laser light is coupled into an optical

cavity of length L consisting of two mirrors with a reflectivity close to unity. The light leaking out of the cavity has an envelope, which is simply a first-order exponential decay, $\exp(-t/\tau)$. The ring down time, τ , reflects the rate of absorption rather than its magnitude, and as such the method is independent of power fluctuations. In addition, very long absorption path lengths are obtained by confining light tens of microseconds to the cavity. A spectrum is recorded by measuring τ as function of the laser frequency.

In the present experiment, a standard pulsed CRD spectrometer with a resolution of 0.15 cm^{-1} is used to sample a pulsed supersonic plasma, generated by discharging a mixture of 0.3% HCCH (or DCCD or both) in He (-600 V, 100 mA) in the throat of a 300 mm \times 300 μm multichannel slit nozzle geometry.¹³ This system combines high molecular densities and relatively large absorption path lengths with an effective adiabatic cooling. The best S/N ratios are found when the CRD beam intersects the expansion 3 mm downstream from the nozzle orifice. The light exiting the optical cavity is focused via a narrow band-pass filter onto a broad band Si photodiode and is monitored by a fast oscilloscope. Typical ring down times amount to $\tau = 50 \mu s$. For a cavity of length $L = 52$ cm, this is equivalent to approximately 29 000 passes through the plasma or an effective absorption path length of 865 m. The present data set is calibrated via the internal reference system of the dye laser, yielding an absolute accuracy on the order of 0.5 cm^{-1} around 815 nm.

Results and Discussion

For an $A^2\Pi_u-X^2\Pi_g$ electronic transition of a linear molecule, one expects to observe two separate bands (each consisting of a P-, Q-, and R-branch) of the two spin-orbit transitions $A^2\Pi_{3/2}-X^2\Pi_{3/2}$ and $A^2\Pi_{1/2}-X^2\Pi_{1/2}$. The intensity ratio of the two bands is determined by the spin-orbit temperature (T_{so}) and the spin-orbit splitting in the ground state (A''). The latter is expected to be close to the value found for the tri- and tetraacetylene cations, $-31 cm^{-1}$. The minus sign indicates that the ground state is inverted—as was observed for the smaller polyacetylene chains^{5,6}—i.e., the $\Omega = 3/2$ component is below $\Omega = 1/2$. The separation between the two bands in the spectrum is given by the difference in spin-orbit constants in excited and ground state ($\Delta A = A' - A''$) and is expected to be on the order of 3 cm^{-1} .

The origin band in the $A^2\Pi_u-X^2\Pi_g$ electronic transition of $HC_{10}H^+$ is shown in the left part of Figure 1. The band contour

[†] Part of the special issue "Jack Beauchamp Festschrift".

* To whom correspondence should be addressed. E-mail: J.P.Maier@unibas.ch.

[§] Visiting scientist, Laser Centre, Department of Physics and Astronomy, Vrije Universiteit, De Boelelaan 1081, NL 1081 HV Amsterdam, The Netherlands

[#] Address from 01/09/2002: Department of Physical Chemistry, Vrije Universiteit, De Boelelaan 1083, NL 1083 HV Amsterdam, The Netherlands.

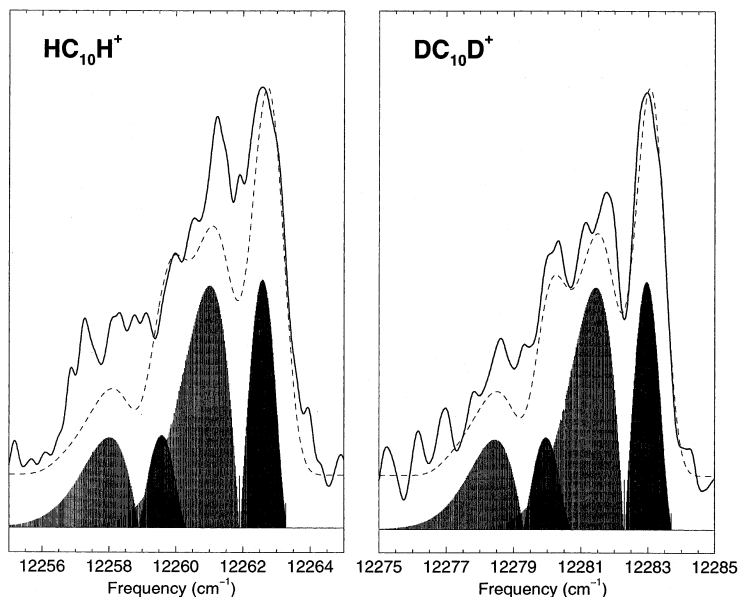


Figure 1. A smoothed laboratory spectrum of the $A^2\Pi_0-X^2\Pi_g$ electronic origin band transition of $HC_{10}H^+$ (left side) and $DC_{10}D^+$ (right side) recorded in absorption using cavity ring down spectroscopy with 0.15 cm^{-1} resolution. Both spin-orbit components are visible, as can be concluded from the stick diagram. The latter shows the simulation for a rotational temperature of $T_{\text{rot}} = 45\text{ K}$ and molecular parameters as listed in Table 1. The dashed line shows the simulation for the unresolved spectrum.

of both spin-orbit components is visible, even though there is some overlap with the absorption lines of another species, presumably C_2 . The band is not rotationally resolved because the rotational constant of $HC_{10}H^+$ is on the order of 0.01 cm^{-1} and the best laser resolution obtained with an internal etalon was 0.035 cm^{-1} . In addition, lifetime broadening might occur as result of intramolecular processes. It is possible, however, to interpret the band contours in terms of unresolved P-, Q- and R-branch contours of the $A^2\Pi_{3/2}-X^2\Pi_{3/2}$ and $A^2\Pi_{1/2}-X^2\Pi_{1/2}$ electronic transitions. This is demonstrated in the figure with stick diagrams.

The observed rotational profiles were simulated to determine the band origin position and to estimate the spectroscopic constants, using PGopher.¹⁴ The ground state spin-orbit splitting is assumed to be similar to that found for the tri- and tetraacetylene cations, -31 cm^{-1} . The intensity ratio of the two spin-orbit bands yields $T_{\text{so}} = 45(5)\text{ K}$, which will be close to the rotational temperature, T_{rot} . This value is higher than that in previous experiments (e.g., ref 15) and a direct consequence of measuring closer to the slit nozzle orifice; further downstream the shoulder at lower energy disappears and only the $A^2\Pi_{3/2}-X^2\Pi_{3/2}$ band is observed. The ground-state rotational constant $B'' = 0.00988\text{ cm}^{-1}$ is calculated from a recent ab initio density functional theory geometry optimization that gives $H-C1 = 1.068\text{ \AA}$, $C1-C2 = 1.219\text{ \AA}$, $C2-C3 = 1.330\text{ \AA}$, $C3-C4 = 1.240\text{ \AA}$, $C4-C5 = 1.311\text{ \AA}$, and $C5-C6 = 1.246\text{ \AA}$,⁷ reflecting a single-triple bond alternation.¹⁶ A good simulation is obtained for an origin band value of $T_0 = 12\,260.4(5)\text{ cm}^{-1}$, blue-shifted 117 cm^{-1} with respect to the matrix value and with excited-state values $A' = -28\text{ cm}^{-1}$ (i.e., $\Delta A = 3\text{ cm}^{-1}$) and $B' = 0.00982\text{ cm}^{-1}$. The latter value is expected to be accurate to within a few percent. The ratio $B''/B' = 1.007$ is close to unity; for a chain as long as $HC_{10}H^+$, only a minor change in molecular geometry is expected upon electronic excitation. For smaller chains, the effect is more pronounced. This can be seen from Table 1 in which the parameters of a number of polyacetylene cations HC_nH^+ are compared.

TABLE 1: Comparison of the Spectroscopic Constants of Linear Chains HC_nH^+ , DC_nD^+ , and HC_nD^+

	HC_nH^+			
	$n = 4^b$	$n = 6^c$	$n = 8^d$	$n = 10^{e,f}$
T_0	19 722.610(2)	16 654.6873(3)	14 143.1815(5)	12 260.4(5)
B''	0.146 888(22)	0.044 594(3)	0.019 078(9)	0.009 88(3)
B'	0.140 083(22)	0.043 792(3)	0.018 867(9)	0.009 82(3)
B''/B'	1.049	1.018	1.011	1.007
A''	-33.5(1.9)	-31.40(28)	(-31)	(-31)
A'	-31.1(2.0)	-28.41(28)	(-28)	(-28)
ΔA			3	3
	HC_nD^+			
	$n = 4^g$	$n = 6^c$	$n = 8^g$	$n = 10^f$
T_0	19 731.725(2)	16 670.6168(3)	14 156.3(3)	12 270.6(5)
B''	0.136 599(30)	0.042 573(8)		
B'	0.130 469(30)	0.041 815(8)		
B''/B'	1.047	1.018		
A''	(-33.3)	-32.37(56)		
A'	(-31.1)	-29.42(56)		
ΔA	2.2			
	DC_nD^+			
	$n = 4^b$	$n = 6^c$	$n = 8^d$	$n = 10^f$
T_0	19 740.683(2)	16 686.5100(3)	14 169.5243(3)	12 280.8(5)
B''	0.127 403(24)	0.040 701(9)	0.017 648(6)	0.009 23(5)
B'	0.121 831(25)	0.039 980(9)	0.017 452(6)	0.009 17(5)
B''/B'	1.046	1.018	1.011	1.007
A''	-33.3(2.0)	-31.31(49)	(-31)	(-31)
A'	-31.1(2.0)	-28.40(49)	(-28)	(-28)
ΔA			3	3

^a All values are in cm^{-1} . ^b Reference 2. ^c Reference 3. ^d Reference 4. ^e Reference 6. ^f This work. ^g Reference 19.

For larger n , the rotational constants B decrease, the ratio B''/B' decreases as well, and there is a monotonic shift of the origin band to the red. The oscillator strength increases with n , which holds promise for the extension of the experimental approach to measure the electronic spectrum of even longer species.

A confirmation of the assignment of the observed 815.5 nm band to the pentaacetylene cation is provided by the detection of this transition in the partially (HC_{10}D^+) and fully deuterated (DC_{10}D^+) species. The latter is shown in the right part of Figure 1, approximately 20 cm^{-1} blue-shifted with respect to the HC_{10}H^+ band. A good simulation of the observed spectrum is obtained for $B'' = 0.009\ 23(5)\text{ cm}^{-1}$, $B' = 0.009\ 17(5)\text{ cm}^{-1}$, and $T_0 = 12\ 280.8(5)\text{ cm}^{-1}$ (Figure 1). The corresponding stick diagram is shown as well. The spectrum of the monodeuterated chain, HC_{10}D^+ , has been observed at $12\ 270.6(5)\text{ cm}^{-1}$ but is rather weak, and a contour simulation is not possible. Table 1 summarizes the determined spectroscopic constants for chains HC_nD^+ and DC_nD^+ , with $n = 4, 6, 8,$ and 10 .

This work presents the electronic spectrum of the largest polyacetylene cation measured in the gas phase so far. Nevertheless, a comparison with the hitherto reported diffuse interstellar bands in the near infrared^{17,18} shows that there is no absorption apparent at the position of the origin band in the electronic spectrum of HC_{10}H^+ .

Acknowledgment. This work has been supported by the Swiss National Science Foundation, Project 20.63459.00, and the Bundesamt für Bildung und Wissenschaft, Project 01.0299. H.L. thanks support of FOM (Fundamental Onderzoek der Materie).

References and Notes

- (1) Cha, C.; Weinkauff, R.; Boesl, U. *J. Chem. Phys.* **1995**, *103*, 5224.
- (2) Callomon, J. H. *Can. J. Phys.* **1956**, *34*, 1046.
- (3) Lecoultrre, J.; Maier, J. P.; Rösslein, M. *J. Chem. Phys.* **1988**, *89*, 6081.
- (4) Sinclair, W. E.; Pfluger, D.; Linnartz, H.; Maier, J. P. *J. Chem. Phys.* **1999**, *110*, 296.
- (5) Pfluger, D.; Motylewski, T.; Linnartz, H.; Sinclair, W. E.; Maier, J. P. *Chem. Phys. Lett.* **2000**, *329*, 29.
- (6) Pfluger, D.; Sinclair, W. E.; Linnartz, H.; Maier, J. P. *Chem. Phys. Lett.* **1999**, *313*, 171.
- (7) Betowski, L. D.; Winnik, W.; Marcus, A. B.; Pyle, S. M. *Int. J. Mass Spectrosc.* **1998**, *173*, 27.
- (8) Lee, S.; Gotts, N.; von Helden, G.; Bowers, M. T. *J. Phys. Chem. A* **1997**, *101*, 2096.
- (9) Pyle, S. M.; Betowski, L. D.; Marcus, A. B.; Winnik, W.; Brittain, R. D. *J. Am. Soc. Mass. Spectrom.* **1997**, *8*, 183.
- (10) Tielens, A. G. G. M.; Snow, T. P., Eds. Laboratory studies of proposed carriers. *The diffuse interstellar bands*; Kluwer Academic Publishers: Dordrecht, Netherlands, 1995; pp 175–238.
- (11) Freivogel, P.; Fulara, J.; Lessen, D.; Forney, D.; Maier, J. P. *Chem. Phys.* **1994**, *189*, 335.
- (12) O'Keefe, A.; Deacon, D. A. G. *Rev. Sci. Instrum.* **1988**, *59*, 2544.
- (13) Motylewski, T.; Linnartz, H. *Rev. Sci. Instrum.* **1999**, *70*, 1305.
- (14) Western, C. M. *PGOPHER*; School of Chemistry, University of Bristol: Bristol, U.K., 1994 and 1998.
- (15) Linnartz, H.; Motylewski, T.; Vaizert, O.; Maier, J. P.; Apponi, A. J.; McCarthy, M. C.; Gottlieb, C. A.; Thaddeus, P. *J. Mol. Spectrosc.* **1999**, *197*, 1.
- (16) A nearly identical value is found when extrapolating the values available for the rotational constants of the di-, tri- and tetraacetylene cations.
- (17) Jenniskens, P.; Desert, F.-X. *Astron. Astrophys.* **1994**, *106*, 39.
- (18) Galazutdinov, G. A.; Musaeu, F. A.; Krelowski, J.; Walker, G. A. H. *Publ. Astron. Soc. Pac.* **2000**, *112*, 648.
- (19) Vaizert, O.; Furrer, P.; Cias, P.; Linnartz, H.; Maier, J. P. *J. Mol. Spectrosc.* **2002**, *214*, 94.

Gas phase detection of cyclic B_3 : $2^2E' \leftarrow X^2A'_1$ electronic origin band

P. Cias, M. Araki, A. Denisov, and J. P. Maier^{a)}

Department of Chemistry, University of Basel, Klingelbergstrasse 80, CH-4056 Basel, Switzerland

(Received 29 January 2004; accepted 19 July 2004)

The rotationally resolved origin band in the $2^2E' \leftarrow X^2A'_1$ electronic spectrum of cyclic B_3 has been observed by cavity ring down spectroscopy in the gas phase. The B_3 molecule was generated in a supersonic planar plasma containing decaborane ($B_{10}H_{14}$) and neon as a carrier gas. The rotational structure pattern is that of a cyclic molecule. It is analyzed assuming an equilateral triangle in both electronic states. The band origin is determined to be $21\,853.52\text{ cm}^{-1}$, and the bond lengths $1.603\,77(106)\text{ \AA}$ in the ground and $1.619\,07(96)\text{ \AA}$ in the excited electronic state are inferred from analysis of the rotational structure. © 2004 American Institute of Physics.

[DOI: 10.1063/1.1791153]

I. INTRODUCTION

Well resolved absorption and emission spectra of cyclic trimers have been reported only for few species, including, Al_3 ,¹ Li_3 ,² Cu_3 ,³ H_3^+ ,⁴ and Na_3 .⁵ As the small boron molecules have applications in industry as chemical insulators, explosives, semiconductors, and high energy density materials, their structure is of relevance.^{6,7} The boron trimer has been investigated only in rare gas matrices. First came the electron-spin-resonance observation which showed that B_3 contains an unpaired electron and that the three nuclei are equivalent.⁸ The infrared spectrum of B_3 was also observed,¹ and recently the $2^2E' \leftarrow X^2A'_1$ electronic transition of B_3 in a neon matrix was identified using a mass selective approach.⁹ However, there is no spectroscopic information on the boron trimer B_3 in the gas phase.

There is interest in the spectrum of cyclic B_3 because several of the excited electronic states are degenerate in D_{3h} symmetry. According to the Jahn-Teller theorem, there exists at least one vibrational mode that removes the electronic degeneracy and results in the stabilization of the lowest component by lowering the symmetry of the equilibrium structure. Most recent theoretical calculations on B_3 predicted an equilateral structure (D_{3h}) with an $^2A'_1$ electronic symmetry in the electronic ground state and an obtuse triangle (C_{2v}) with an apex angle $\geq 60^\circ$ for the $2^2E'$ excited electronic state.^{8,10,11} However, a low stabilization energy (difference between the conical intersection and the minima) compared with zero point energy for the $2^2E'$ state is reported.⁹ Therefore the B_3 molecule can be considered to have D_{3h} symmetry in the $2^2E'$ state as an effective structure and the $2^2E' \leftarrow X^2A'_1$ electronic system can be considered as a quasi " D_{3h} - D_{3h} " transition.

In the present work we report the observation of the rotationally resolved origin band of the $2^2E' \leftarrow X^2A'_1$ electronic spectrum of B_3 . The analysis of the spectrum gives an estimate of the molecular geometry; the first gas phase structural determination.

II. EXPERIMENT

This consists of a standard cavity ring down setup sampling a plasma generated in a pulsed supersonic slit jet expansion.¹² A small fraction of pulsed laser light from a tunable dye laser is coupled into an optical cavity consisting of two highly reflective mirrors ($R > 99.99\%$). The fraction of light leaking out of the cavity has an envelope which is a first-order exponential decay, $\exp(-t/\tau)$. The ring down time τ reflects the absorption coefficient. A spectrum is recorded by measuring τ as function of the wavelength of the laser (running at 30 Hz). Forty-five ring down events are averaged at each wavelength before the digitized data are downloaded to a workstation. The $\sim 0.05\text{ cm}^{-1}$ linewidth of the laser was attenuated with an internal etalon.

The pulsed slit jet system is located in a vacuum chamber evacuated by a roots blower. The plasma is produced in a nozzle incorporating a discharge in the high pressure expansion. The orifice comprises a metal plate anode and two sharp stainless steel cathodes that form the actual slit ($30\text{ mm} \times 300\text{ }\mu\text{m}$). A pulsed negative voltage ($-800\text{ V}/100\text{ mA}$ and $100\text{ }\mu\text{s}$ in duration) is applied. The geometry of the orifice is such that the discharge is confined upstream of the supersonic expansion. To produce B_3 , solid $B_{10}H_{14}$ is heated in the oven to $70 \pm 10^\circ\text{C}$ with neon as a carrier gas at a backing pressure of 10 bars. In order to avoid condensation inside the source, the valve and body of the nozzle are heated as shown in Fig. 1. The B_3 molecules are efficiently produced at a distance 5 mm down stream from the slit. The spectrum is calibrated via the neon atomic lines that are observed in the jet expansion.

III. RESULTS

The $2^2E' \leftarrow X^2A'_1$ electronic spectrum of B_3 was initially identified in absorption in a 6 K neon matrix using mass selection with origin band located at $21\,828\text{ cm}^{-1}$.⁹ Based on this the band was sought in the gas phase. The absorption signal was subsequently found near $21\,900\text{ cm}^{-1}$ (Fig. 2) and the observed profile of the band, $\sim 25\text{ cm}^{-1}$ in width, was in a good agreement with preliminary simulations. No other signal could be detected within $\pm 300\text{ cm}^{-1}$

^{a)} Author to whom correspondence should be addressed; Fax: +41-61-2673855. Electronic mail: J.P.Maier@unibas.ch

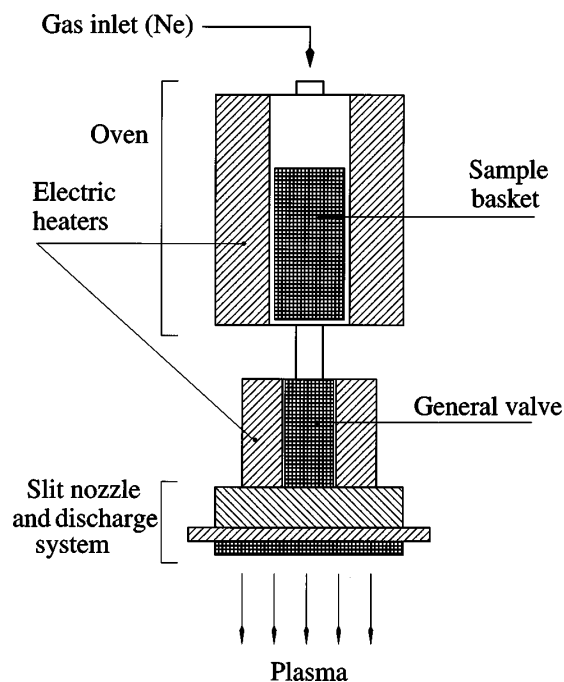


FIG. 1. Schematic diagram of the source used to produce B₃. Decaborane was heated up to 70±10 °C in the oven. Neon at a backing pressure of 10 bars was used as a carrier gas. The pulsed plasma was produced by a slit nozzle to which the high voltage was applied.

from the observed band. Though the spectrum visually appears “noisy” (typical *S/N* of at least 5) all the peaks are genuine. This is shown by the top trace which is an independent recording of this part of the band. Corresponding traces were obtained for other regions proving that all the lines given in Tables I and III are real.

The spectrum exhibits rotationally resolved *P* and *R* branches slightly blended with strong neon atomic lines. The *Q* branch is not visible due to a complex splitting and blending with an intense neon line. Actually, it is a composition of four spectra, as two boron isotopes are present. Because the natural isotopic abundance of ¹¹B:¹⁰B in the precursor is 4:1, the relative concentration of the two isotopomers ³³B₃:³²B₃ (two equivalent structures of ¹⁰B¹¹B₂) should be 4:3. The peaks in the spectra of ³¹B₃ and ³⁰B₃ could not be assigned due to their small abundance. As a result, the observed spectrum is essentially an overlap of the two isotopomers ³³B₃ and ³²B₃.

The B₃ cyclic molecule in the excited degenerate state should undergo a deformation due to the Jahn-Teller effect, however, the distortion from an equilateral triangle can be neglected as a result of low stabilization energy [merely 39 cm⁻¹ compared with a zero-point energy (1522 cm⁻¹) in the 2²E'' state⁹]. A similar situation was encountered for the cyclic C₃H radical, where deformations of the C_{2v} structure were neglected due to small energy differences between the C_s and C_{2v} forms.¹³ Therefore, it is reasonable to assume that the effective symmetry of the 2²E' state is D_{3h} for the analysis of the rotational structure in the observed spectrum.

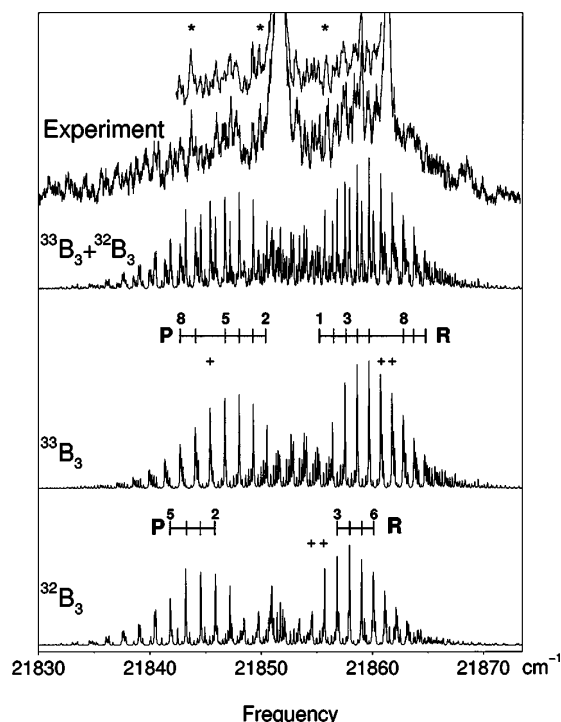


FIG. 2. Rotationally resolved 2²E'←X²A₁ electronic origin band of B₃ in the gas phase measured by cavity ring down spectroscopy through a super-sonic planar plasma. The two upper traces are independent recordings to show that the peaks are real and not noise. The three bottom traces are the simulated patterns ³³B₃+³²B₃ (in ratio 4:3), ³²B₃ and ³³B₃. The two strong lines off scale belong to neon. Bands marked with* are unassigned. Lines in the simulation for which counterparts in the spectrum could not be found are marked with “+.”

The measured positions of the ³³B₃ lines are given in Table I. The spectral line frequencies were analyzed using a conventional Hamiltonian for a symmetric top molecule. In order to analyze the imperfectly resolved rotational spectrum it was assumed that the structure of the B₃ molecule has D_{3h} symmetry in both states. This way the number of spectro-

TABLE I. Frequencies (in cm⁻¹) and assignments in the 2²E'←X²A₁ absorption spectrum of ³³B₃.

<i>N_K</i>	<i>ν</i> _{obs}	<i>ν</i> _{calc}	<i>ν</i> _{obs} − <i>ν</i> _{calc}
1 ₁ -2 ₂	21 850.374	21 850.543	−0.169 ^a
2 ₂ -3 ₃	21 849.223	21 849.296	−0.073
3 ₃ -4 ₄	21 848.070	21 848.027	0.043
4 ₄ -5 ₅	21 846.731	21 846.736	−0.005
6 ₆ -7 ₇	21 844.118	21 844.086	0.032
7 ₇ -8 ₈	21 842.710	21 842.727	−0.017
1 ₁ -0 ₀	21 855.230	21 855.305	−0.075
2 ₂ -1 ₁	21 856.499	21 856.440	0.059
3 ₃ -2 ₂	21 857.600	21 857.552	0.048
4 ₄ -3 ₃	21 858.629	21 858.642	−0.013
5 ₅ -4 ₄	21 859.690	21 859.710	−0.020
8 ₈ -7 ₇	21 862.770	21 862.778	−0.008
9 ₉ -8 ₈	21 863.713	21 863.756	−0.043
10 ₁₀ -9 ₉	21 864.749	21 864.712	0.037

^aNot included in the least-squares fit.

TABLE II. Bond lengths and spectroscopic constants of the $^{33}\text{B}_3$ molecule inferred from the partial rotational analysis of the $2^2E' \leftarrow X^2A_1'$ electronic origin band.^a

	$^2A_1'$		$2^2E'$	
	Obs.	Calc. ^b	Obs.	Calc. ^b
r_0 (Å)	1.603 77(106)		1.619 07(96)	
θ_0 (deg)	60.0 ^c		60.0 ^c	
r_e (Å)		1.5706		1.5955
θ_e (deg)		60.0		60.8
T_{00} (cm ⁻¹)			21 853.52 ^d	22 723
B (cm ⁻¹)	1.190 64(157) ^e		1.168 25(138) ^e	
C (cm ⁻¹)	0.595 32(79) ^e		0.584 12(69) ^e	

^aThe numbers in parentheses represent the one standard deviation derived from the least square fitting. A rms of the fitting is 0.043 cm⁻¹.

^bReference 9.

^cFixed.

^dError of calibration is around 0.01 cm⁻¹.

^eThe rotational constants were calculated from the determined molecular structures.

scopic parameters could be reduced to 3; the bond lengths r' , r'' and band origin T_{00} were then determined directly from a least-squares fit to the line positions.

The results for the $^{33}\text{B}_3$ molecule are listed in Table II. The determined bond lengths (r_0) are 2% longer than the calculated ones (r_e) (Ref. 9) in both the ground and excited states. In the ground state this is because of zero-point vibrations as the analysis assumes a negligible inertial defect. The difference in the excited state is additionally caused by imperfections of the simple model used (assuming an equilateral triangle $\theta=60^\circ$ and ignoring the Jahn-Teller effect) and anharmonicity of the potential.

The observed rotational profile was also simulated with the obtained molecular constants using the program WANG.¹⁴ The simulated spectrum of $^{33}\text{B}_3$ is shown in Fig. 2. Best agreement with the experiment was attained with a rotational temperature of 30 K. A linewidth of 0.05 cm⁻¹ was used for the simulation, though in the observed spectrum it is larger due to Doppler and/or lifetime broadening.

In the case of the $^{32}\text{B}_3$ isotopomer the simulation was based on the same geometry and temperature parameters as inferred for $^{33}\text{B}_3$ but using a conventional Hamiltonian of an asymmetric top molecule. It was also assumed that only the B_2-A_1 transition, which is a type, occurs. The rotational constants used for the $^{32}\text{B}_3$ molecule were $A:B:C=1.2696:1.1906:0.6144$ cm⁻¹ for the ground, and $1.2457:1.1682:0.6029$ cm⁻¹ for the excited state. The spectrum of $^{32}\text{B}_3$ was then shifted by -1.94 cm⁻¹ (from T_{00} of $^{33}\text{B}_3$) to get the best agreement with the observation (Fig. 2). The isotopic shift of -1.94 cm⁻¹ is reasonable for an origin band.

In all, 34 rotational transitions were assigned; 14 of them are attributed to the $^{33}\text{B}_3$ molecule and the rest to $^{32}\text{B}_3$ (Table III). The presented rotational assignment and molecular structure of the B_3 molecule should be considered as tentative, because the insufficient S/N ratio of the spectrum decreases the accuracy of the molecular structure determina-

TABLE III. Frequencies (in cm⁻¹) and assignments in the $2^2E' \leftarrow X^2A_1'$ absorption spectrum of $^{32}\text{B}_3$.^a

$N_{K_a K_c}$	ν_{obs}	ν_{calc}	$\nu_{\text{obs}} - \nu_{\text{calc}}$
2 ₁₂ -3 ₁₃	21 847.174	21 847.197	-0.023
2 ₀₂ -3 ₀₃		21 847.183	-0.009
3 ₁₃ -4 ₁₄	21 845.859	21 845.877	-0.018
3 ₀₃ -4 ₀₄		21 845.876	-0.017
4 ₁₄ -5 ₁₅	21 844.525	21 844.544	-0.019
4 ₀₄ -5 ₀₅			
5 ₁₅ -6 ₁₆	21 843.220	21 843.188	0.032
5 ₀₅ -6 ₀₆			
6 ₁₆ -7 ₁₇	21 841.821	21 841.809	0.012
6 ₀₆ -7 ₀₇			
7 ₁₇ -8 ₁₈	21 840.420	21 840.407	0.013
7 ₀₇ -8 ₀₈			
4 ₁₄ -3 ₁₃	21 856.843	21 856.832	0.011
4 ₀₄ -3 ₀₃		21 856.833	0.010
5 ₁₅ -4 ₁₄	21 857.952	21 857.934	0.018
5 ₀₅ -4 ₀₄			
6 ₁₆ -5 ₁₅	21 859.041	21 859.013	0.028
6 ₀₆ -5 ₀₅			
7 ₁₇ -6 ₁₆	21 860.125	21 860.068	0.057
7 ₀₇ -6 ₀₆			

^aThe assignment and calculated frequencies were derived on the assumption that the bond lengths of $^{32}\text{B}_3$ and $^{33}\text{B}_3$ are equal, and the isotopic shift is -1.94 cm⁻¹.

tion. Lines of $^{31}\text{B}_3$ ($\approx 19\%$ of the $^{33}\text{B}_3$ intensity) disturb the line profiles of $^{32}\text{B}_3$ and $^{33}\text{B}_3$ transitions. There are few unassigned lines, few missing ones, and some are obscured by intense neon atomic lines (Fig. 2). However, the consistency of the whole analysis is sufficient to conclude that the observed rotationally resolved spectrum is indeed the $2^2E' \leftarrow X^2A_1'$ transition of the cyclic B_3 molecule, and leads to the first structural information in the gas phase.

ACKNOWLEDGMENTS

This work has been supported by the Office of Aerospace Research and Development and the Swiss National Science Foundation (Project No. 200020-100019).

- S. Li, R. J. Van Zee, and W. Weltner, Chem. Phys. Lett. **262**, 298 (1996).
- M. Keil, H.-G. Kraemer, A. Kudell, M. A. Baig, J. Zhu, W. Demtroeder, and W. Meyer, J. Chem. Phys. **113**, 7414 (2000).
- A. O'Keffe, J. J. Scherer, A. L. Cooksy, R. Sheeks, J. Heath, and R. J. Saykally, Chem. Phys. Lett. **172**, 214 (1990).
- A. R. W. McKellar and J. K. G. Watson, J. Mol. Spectrosc. **191**, 215 (1998).
- H. A. Eckel, J. M. Gress, J. Biele, and W. Demtroeder, J. Chem. Phys. **98**, 135 (1993).
- L. Hanley, J. L. Whitten, and S. L. Anderson, J. Phys. Chem. **92**, 5803 (1988).
- J. D. Presilla-Marquez, C. W. Larson, and P. G. Carrick, J. Chem. Phys. **105**, 3398 (1996).
- Y. M. Hamrick, R. J. Van Zee, and W. Weltner, J. Chem. Phys. **96**, 1767 (1992).
- M. Wyss, E. Riaplov, A. Batalov, J. P. Maier, T. Weber, W. Meyer, and P. Rosmus, J. Chem. Phys. **119**, 9703 (2003).
- R. Hernandez and J. Simons, J. Chem. Phys. **94**, 2961 (1991).
- J. M. L. Martin, J. P. Francois, and R. Gijbels, J. Chem. Phys. **90**, 6469 (1989).
- H. Linnartz, T. Motylewski, and J. P. Maier, J. Chem. Phys. **109**, 3819 (1998).
- S. Yamamoto and S. Saito, J. Chem. Phys. **101**, 5484 (1994).
- D. Luckhaus and M. Quack, Mol. Phys. **63**, 745 (1989).

NEW LABORATORY DATA ON A MOLECULAR BAND AT 4429 Å

M. ARAKI, H. LINNARTZ,¹ P. KOLEK, H. DING, A. BOGUSLAVSKIY, A. DENISOV, T. W. SCHMIDT,
T. MOTYLEWSKI, P. CIAS, AND J. P. MAIER

Department of Chemistry, University of Basel, Klingelbergstrasse 80, CH-4056 Basel, Switzerland; mitsunori.araki@unibas.ch,
linnartz@few.vu.nl, p.kolek@unibas.ch, hongbin.ding@unibas.ch, a.boguslav@unibas.ch, alexey.denisov@unibas.ch,
t.schmidt@chem.usyd.edu.au, t.motylewski@bfad.de, pawel@stan.chemie.unibas.ch, j.p.maier@unibas.ch

Received 2004 April 13; accepted 2004 July 30

ABSTRACT

New laboratory data are presented for the previously reported molecular absorption band at 4429 Å observed in a benzene plasma matching the strongest diffuse interstellar band (DIB) at 4428.9 Å. Gas-phase absorption spectra are presented for rotational temperatures of ~ 15 and 200 K. The observations indicate that it is unlikely that the laboratory band and the 4429 Å DIB are related. Eleven isomers of $C_5H_5^{(+)}$ and $C_6H_5^{(+)}$, both neutral and cationic, were considered as possible carriers of the laboratory band in view of the observed rotational profiles and deuterium isotope shifts. The experimental data and theoretical calculations (CASPT3, MRCI) indicate that the HCCHCHCH radical, a planar but nonlinear chain with one hydrogen on each carbon, is the most probable candidate causing the 4429 Å laboratory absorption.

Subject headings: ISM: lines and bands — ISM: molecules — line: identification — methods: laboratory — molecular data

1. INTRODUCTION

Recent progress with sensitive optical spectroscopic techniques allows the detection of gas-phase spectra of molecules that have been considered as potential carriers of diffuse interstellar bands (DIBs). The DIBs are observed as absorption features toward reddened stars (Herbig 1975). Up to now over 200 such features have been reported (Jenniskens & Désert 1994; Tuairisg et al. 2000), varying in width and intensity. It is a long-standing problem to explain their origin. Various forms of matter have been proposed, but none have resulted in an unambiguous assignment (Tielens & Snow 1995). The report in this journal (Ball et al. 2000) of a striking match between a laboratory band at 4429 Å measured through an expanding benzene plasma and the strongest DIB, centered at 4428.9(1.4) Å, has attracted attention, initiating a discussion on whether radical fragments of aromatic rings might be present in the diffuse interstellar medium (Thaddeus & McCarthy 2001).

In their thorough spectroscopic study of a hydrocarbon plasma, Ball et al. find a strong molecular band at 4429.27(4) Å consisting of an unresolved P -, an unresolved Q -, and an unresolved R -branch, matching in wavelength to a few parts in 10^4 the 4429 DIB. They conclude from partial and complete deuteration of the precursor gas benzene that the laboratory carrier is a hydrocarbon of the form $C_nH_5^{(+)}$ with two pairs of equivalent hydrogen atoms plus a single hydrogen. They discuss a series of possible radicals and propose as most likely candidates the quasi-linear benzene fragments $C_3H_5^+$ and C_5H_5 , for which optical data have not been reported.

While the match in wavelength between the laboratory and astronomical spectra is striking, there is no agreement in their line widths; the 4429 DIB feature is about 17 times wider than the band observed in the jet. In two recent studies of the intrinsic profile of the 4429 DIB (Snow 2002; Snow et al. 2002), the lack of fine structure is attributed to an electronic transition of a

gaseous molecule with the upper state undergoing a rapid internal conversion, or alternatively a system consisting of overlapping rotational lines. The first explanation implies that the laboratory and astronomical spectra are identical both in wavelength and in line width, which is not the case. The second explanation leaves space for the proposition by Ball et al. that the mismatch in line width may be due to a substantial difference in rotational temperature of the carrier in a supersonic beam (a few K), where collisional cooling is the main relaxation mechanism, and in interstellar space (a few hundred K), where radiative cooling might be very inefficient for weakly polar species. Hence measuring the same spectrum at different temperatures will give additional information on the astrophysical relevance of the 4429 Å molecular band. Moreover, the discussion will benefit from the identification of the carrier of the laboratory spectrum.

2. EXPERIMENT

The results of two complementary laboratory experiments are described. The first is similar to that reported by Ball et al. (2000); the 4429 Å band has been recorded through a benzene plasma generated in a planar supersonic jet at rotational temperatures of 15–40 K. In the second a hollow cathode discharge cell is used instead, resulting in a substantially higher rotational temperature of about 200 K. In both experiments, cavity ring-down (CRD) spectroscopy is used as a sensitive detection technique to observe signals in direct absorption (O’Keefe & Deacon 1988). Very long absorption path lengths are obtained by confining the light tens of microseconds in the cavity.

In the first experiment a cooled planar plasma is generated by applying a 500 μ s voltage pulse (-700 to -900 V) to a 1 ms gas pulse of a 0.3% C_6H_6/Ar (C_6D_6/Ar) mixture that is expanded through a $3\text{ cm} \times 300\ \mu\text{m}$ slit with a backing pressure of about 10 bars. This setup has been used in the study of over 20 hydrocarbon radicals and cations up to now (see, e.g., Motylewski et al. 2000) and combines high molecular densities with an effective adiabatic cooling. The resolution is increased

¹ Current address: Laser Centre and Department of Physical Chemistry, De Boelelaan 1083, NL-1081 HV, Amsterdam, Netherlands.

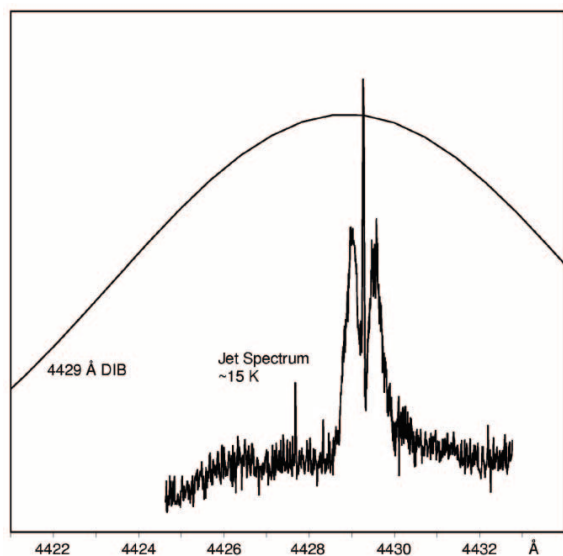


FIG. 1.—The 4429 Å absorption band observed through a planar benzene plasma expansion using a CRD approach. The band coincides in wavelength with the 4429 Å DIB (taken from Jenniskens & Désert 1994 as shown in part above), but the line widths of the laboratory and astronomical spectra differ significantly.

compared to pinhole expansions as used by Ball et al. (2000) because of reduced Doppler broadening parallel to the slit that allows spectroscopy at the limit of the laser resolution. Rotational temperatures are slightly higher, typically 15–40 K.

A much warmer plasma is obtained in the second experiment by applying a 500 μ s voltage pulse (-1000 V) to gas mixtures identical to those used in the jet, but in an 84 cm long hollow cathode discharge cell, running at a pressure of a few mbar. The spectroscopy is not Doppler-free, and with liquid nitrogen cooling, rotational temperatures are typically 150–200 K (Kotterer et al. 1996).

3. RESULTS AND DISCUSSION

3.1. Comparison between the 4429 Å DIB and Laboratory Bands

Figure 1 shows the CRD spectrum obtained through the supersonic planar plasma. Although the signal-to-noise ratio is good, no rotational structure is observed that could provide structural information that is necessary to identify the carrier. This indicates either that the separation between adjacent lines is smaller than 0.03 cm^{-1} or that a lifetime broadening exists. The absorption profile is in the middle of the strong 4429 Å DIB as seen from the synthetic spectrum shown in Figure 1. As discussed by Ball et al. (2000), there is a clear difference in spectral width of both features, and this has to be explained before a correlation between the laboratory and astronomical spectra can be established. Ball et al. correctly argue that for the proposed nearly symmetric prolate top molecules, a spectrum consisting of a P -, a Q -, and an R -branch is expected similar to the one observed, under the explicit condition that only the lowest K ladder in the ground state is populated. The many subbands from the higher K ladders of the ground state may fill out the contour at higher temperatures, causing the observed spectrum to broaden symmetrically, as observed recently for the nonlinear carbon chain C_6H_4^+ (Araki et al.

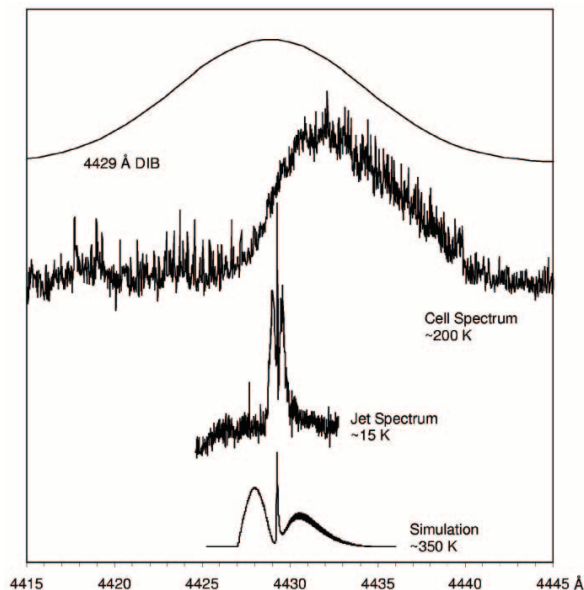


FIG. 2.—The 4429 Å absorption band measured in a jet and liquid nitrogen cooled hollow cathode discharge cell and compared to the 4429 Å DIB (taken from Jenniskens & Désert 1994). At the higher temperature a clear broadening is observed. A simulated rotational profile at 350 K, using the same constants as in Fig. 3, is clearly different from the observed cell spectrum.

2003). Therefore the same spectrum was recorded under warmer conditions than in the jet expansion. Decreasing the backing pressure, increasing the benzene/mixing ratio, measuring closer to the jet, and using higher discharge voltages generally increases the rotational temperature from 15 to 30–40 K. Indeed, we observed a small shift in the Boltzmann maximum to higher J -values, but no broadening could be observed. Consequently, a cell discharge was then used to obtain a much higher temperature.

In Figure 2 the absorption spectrum recorded in a liquid nitrogen cooled hollow cathode cell is shown. The rotational temperature under these conditions is about 200 K. A band broadened asymmetrically to the red is now observed (Fig. 2, with the jet spectrum shown as a reference). Such a broadening is typical for a hot-band progression and quite possible at the high ambient temperatures in the cell. Nevertheless, the spectrum does not fill up the 4429 Å DIB. In order to be sure that the cell and jet spectra are due to the same carrier, the experiment was repeated with fully deuterated benzene as precursor; the absorption feature shifts $123(1)$ cm^{-1} to higher energy, which is identical to the shift observed in the jet study: 122.8 cm^{-1} (Ball et al. 2000). These observations seem to indicate that the laboratory band and the 4429 Å DIB originate from different carriers.

In order to compare the laboratory and astronomical spectra it would be helpful to know more about the vibrational temperature (T_{vib}) in the cell plasma, but without the detection of a resolved transition from a vibrationally excited level in the ground state it is hard to determine this value. Generally, vibrational temperatures in a cooled cell discharge vary from a few hundred to a thousand kelvins according to similar discharge systems (Zelinger et al. 2003; Greenberg & Hargis 1990). The determination of rotational temperatures (T_{rot}), e.g., 200 K for N_2^+ (Kotterer et al. 1996) and 500–600 K for D_3O^+ (Araki et al. 1999) put a lower limit to T_{vib} . Such values are indeed

sufficiently high to excite low-frequency vibrational modes in molecules the size of C_5H_5 . A broadening due to a series of hot-band progressions is therefore reasonable to assume.

On the other hand, in the plasma jet expansion such bands are not expected. It has been shown that these low rotational temperatures at high vibrational temperatures are obtained for small (diatomic) molecules (Bazalgette Courrèges-Lacoste et al. 2001), but for larger species with smaller vibrational spacings, rotational and vibrational temperatures will be more similar. As a consequence, hot-band progressions are not observed. Nevertheless, because the cooling and heating mechanisms in space are completely different from those in the laboratory, care has to be taken when comparing the CRD spectrum with the 4429 Å DIB.

3.2. Comparison between the 4429 Å DIB and the Simulated Spectrum

We have made a substantial effort to identify the carrier of the laboratory band by combining experimental and theoretical information. The 4429 Å absorption band has been reproduced using the program WANG (Luckhaus & Quack 1989). It is found that an “*a*-type transition” of a nearly prolate top with rotational constants $A \sim 1$ and $B \approx C \sim 0.1 \text{ cm}^{-1}$ reproduces the observed spectrum under the assumption that the molecular geometry change upon electronic excitation is small and that differences of rotational constants in the two electronic states are less than 1%. A simulated spectrum for 15 K is shown in Figure 3. For B and C values larger than 0.1 cm^{-1} , a resolved rotational profile is expected, which is not the observation. As a consequence, molecules with less than five carbon atoms are not considered. Furthermore, the production of molecules with more than six carbon atoms or with a four-membered ring is not favored in the benzene discharge. Additional information is available from the observation of deuterium isotope shifts by Ball et al. (2000) that indicates that the carrier contains five hydrogen atoms, including two pairs of equivalent ones. These considerations result in 11 isomers of $C_5H_5^{(+)}$ and $C_6H_5^{(+)}$ (Fig. 4), both neutral and cationic, as the most probable carriers of the laboratory spectrum. Anions are not considered since their production is not favored under the conditions used in the CRD experiment.

We have simulated the profile with $T_{\text{rot}} = 350 \text{ K}$ (Fig. 2). This indicates that our cell spectrum cannot be reproduced by a rotational profile of the origin-band alone. This is consistent with the proposed explanation that the cell spectrum is the result of overlap of such rotational profiles for various vibrational hot-band transitions. Furthermore, the simulation at $T_{\text{rot}} = 350 \text{ K}$ indicates the profile of the 4429 Å DIB cannot be reproduced by a rotational profile of the origin-band alone. In the jet spectrum the intensity of the *R*-branch is stronger than that of *P*, because the ground-state rotational constant $(B + C)/2$ is larger than in the excited state. At high temperatures the intensity difference between the *R*- and *P*-branches increases and the rotational profile becomes asymmetric, although the 4429 Å DIB has a symmetric Lorentzian profile (Snow et al. 2002).

As vibrational frequencies in excited electronic states are generally lower than in the ground state, the hot-band transitions are usually to the red of the origin band. This is as seen in the cell spectrum at $T_{\text{vib}} = 200 \text{ K}$, where the profile extends asymmetrically to the red. Thus it does not seem realistic that the profile to the blue of the origin band could be filled by hot-band transitions even at very high values of T_{vib} . Our conclusion is that the laboratory band and the 4429 Å DIB are unlikely to originate from the same carrier.

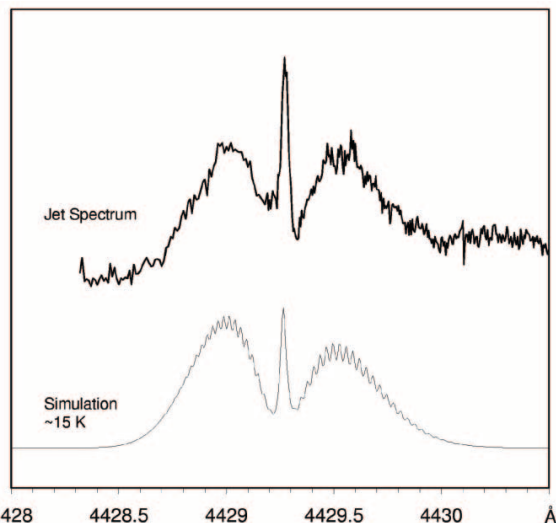


FIG. 3.—Simulated *a*-type rotational profile of the 4429 Å electronic transition for a prolate molecule at 15 K compared to the laboratory absorption spectrum.

3.3. Identification of the 4429 Å Laboratory Band

Calculations of vertical excitation energies and transition moments were carried out for various C_5H_5 and C_6H_5 species (Fig. 4) using the TD-DFT (B3LYP) method with the Gaussian program (Frisch et al. 2003). For selected molecules, higher accuracy excitation energies (vertical and adiabatic) and rotational constants in the ground and excited states were computed with the CASSCF, CASPT3, and MRCI methods, with the MOLPRO 2002.3 package (Werner & Knowles 2003); see Appendix for the computational details. The cc-pVDZ basis set was used in all calculations.

The electronic transition must fulfill four conditions for the molecule to be regarded as a possible carrier for the laboratory band: (1) it must have excitation energy close to the experimental value of 2.80 eV, (2) it must have a nonzero oscillator strength, (3) the transition dipole moment must be predominantly along the *a*-axis ($|\mu_a| \gg |\mu_b|$ and $|\mu_a| \gg |\mu_c|$), and (4) it must have small differences of rotational constants between the ground and excited states. At the TD-DFT stage of calculations, a vertical excitation energy around 2.8–3.1 eV is required. Conditions 1–3 are fulfilled by the neutral radical $5a^N$ and the cation $5b^+$, but they are not fulfilled by any of the C_6H_5 species, either neutral or cationic (Table 1). The TD-DFT method was found useful because it gives vertical excitation energies with a reasonable accuracy (including dynamical correlation) at relatively low computational cost. However, this method is not applicable for $5d$ and $5e$ because of the complicated electronic structures (§ A2). CASSCF calculations for the $5d$ species [doublet $5d^N(D)$ and quartet $5d^N(Q)$ for neutral and singlet $5d^+(S)$ and triplet $5d^+(T)$ for cation] are presented in the Appendix. Calculated electronic structures and spectroscopic parameters of $5d$ and $5e$ are almost the same.

In order to judge whether the carrier of the 4429 Å band is a neutral or a cation, an additional experiment has been carried out. In this the 4429 Å transition was searched for in a benzene plasma with a resonant two-color two-photon ionization (R2C2PI) approach (Ding et al. 2003), capable of measuring the masses of the neutral radicals selectively. The discharge systems used in the R2C2PI and CRD setups are

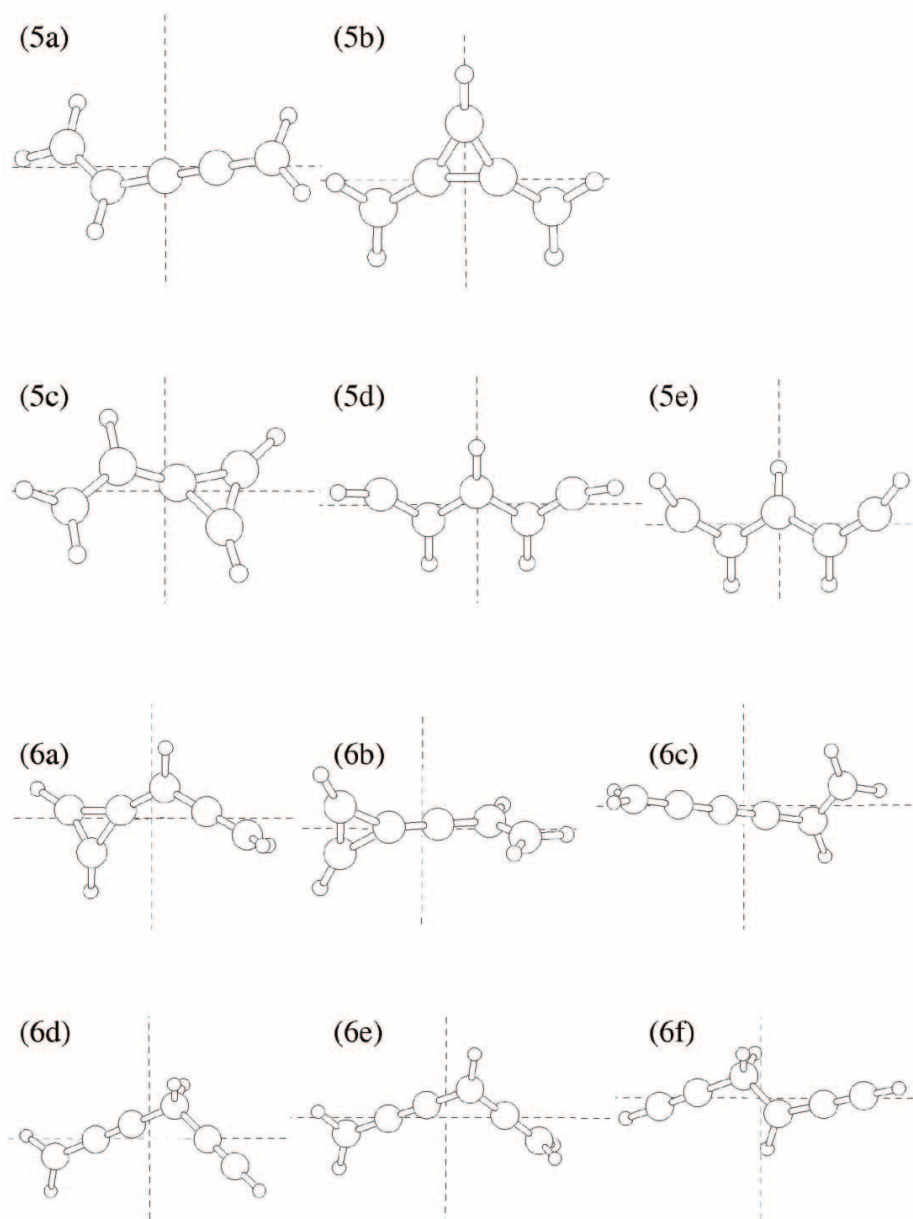


FIG. 4.—Eleven possible C_5H_5 and C_6H_5 isomers with two pairs of equivalent hydrogen atoms and a prolate structure. The horizontal dashed line indicates the a -axis, the vertical one the b -axis; the c -axis is perpendicular to the plane formed by a and b .

comparable, and experiments have been performed using similar conditions. A 0.4% C_6H_6/Ar mixture (backing pressure 5 bars) was discharged between two stainless steel electrodes mounted in the ceramic body of a pinhole source. The excitation laser was scanned around 4429 Å, and intense radiation from an F_2 laser (157 nm) or Nd:YAG (212.5 nm) was used for the ionization. Neutral species with an ionization potential of less than 10.7 eV are detected in this way. All species with a mass of less than 200 amu have been monitored simultaneously.

A weak band of neutral C_5H_5 was observed at 4435 Å, but no band at 4429 Å could be seen (Fig. 5). This suggests

that the carrier of the 4429 Å laboratory band either is a charged species, or a neutral one with an ionization potential higher than 10.7 eV, or has a very short upper electronic state lifetime. It is also possible that the species is destroyed by chemical reactions before reaching the mass spectrometer because in the R2C2PI experiment the molecular beam is probed 30 cm downstream, but only 2 mm downstream in the CRD experiment.

The profiles of the 4429 Å CRD absorption (Fig. 1) and the R2C2PI C_5H_5 band (Fig. 5) are similar, indicating that the molecules probably have similar geometries. The R2C2PI band can be reproduced by a simulation of the rotational profile based

TABLE I
VERTICAL ELECTRONIC TRANSITIONS OF C₅H₅ AND C₆H₅ CALCULATED USING TD-DFT METHOD

ISOMER ^a	NEUTRAL					CATION				
	ΔE^b (eV)	f^c	Transition Moment (D)			ΔE^b (eV)	f^c	Transition Moment (D)		
			μ_a	μ_b	μ_c			μ_a	μ_b	μ_c
5a.....	2.93	0.000	0.000	0.000	0.012	2.36	0.000	0.000	0.000	0.022
	2.98 ^d	0.003	-0.514	-0.016	0.000	4.37	0.498	5.475	0.281	0.000
5b.....	2.22	0.073	2.948	0.000	0.000	3.09 ^d	0.190	-4.032	0.106	0.000
	3.86	0.000	0.000	0.000	-0.065	3.36	0.000	0.000	0.000	-0.105
5c.....	1.57	0.002	-0.097	0.576	0.000	5.62	0.102	-1.861	-1.145	0.000
	3.94	0.001	0.065	-0.272	0.000	5.86	0.391	-4.071	-1.019	0.000
6a.....	1.35	0.002	0.260	0.557	0.000	4.05	0.000	0.000	0.000	-0.007
	2.72	0.000	0.000	0.000	-0.004	5.35	0.000	0.001	0.000	0.007
6b.....	2.34	0.000	0.000	-0.019	0.000	1.89	0.000	0.000	0.027	0.000
	2.93	0.000	-0.008	0.000	-0.069	5.03	0.430	4.692	0.000	-0.729
6c.....	2.38	0.000	-0.002	0.000	-0.008	2.05	0.000	0.008	-0.002	-0.014
	2.70	0.000	0.002	-0.001	0.017	4.07	0.245	3.943	-0.568	0.000
6d.....	3.15	0.000	0.000	-0.001	0.036	1.39	0.000	0.002	0.001	0.121
	4.16	0.041	-1.547	0.483	0.000	1.72	0.068	3.226	-0.004	-0.001
6e.....	3.05	0.000	0.001	0.000	-0.001	2.56	0.000	0.000	0.000	0.005
	3.07	0.001	0.271	-0.184	0.000	2.98	0.000	0.000	0.000	-0.045
6f.....	3.35	0.000	0.000	0.000	-0.004	1.40	0.000	0.007	-0.002	-0.124
	4.02	0.028	-1.353	-0.081	0.000	1.73	0.070	3.235	-0.379	0.001

NOTE.—B3LYP hybrid functional and the cc-pVDZ basis set were used.

^a See Fig. 4.

^b The observed adiabatic transition energy is 2.80 eV (=4429 Å).

^c Oscillator strength.

^d For higher level calculations see Tables 2 and 3.

on the assumptions that the transition is *a*-type and that the carrier is a nearly prolate C₅H₅ molecule at 7 K, a typical temperature of the molecules produced in this apparatus. Simulation at 15 K with the same molecular constants can reproduce the profile of the 4429 Å CRD band. Thus it appears that both the carrier of the 4429 Å CRD and the 4435 Å resonance-

enhanced multiphoton ionization (REMPI) band have five carbon atoms, but are different isomers.

The *5e* isomer cannot convert to cyclic pentadienyl radical as easily as *5d* because additional cis-trans isomerizations are difficult. The isomer does not decay as fast and may be one of the possible candidates for the REMPI band. For the same reason production of *5d* should be favored and a larger abundance of this isomer could be expected immediately after the discharge through benzene. Therefore *5d* would be a better candidate for the carrier of the CRD band.

Higher level theoretical calculations were carried out for the *5a^N*, *5b⁺*, *5d^N(D)*, *5d^N(Q)*, *5d⁺(T)*, *5e^N(D)*, *5e^N(Q)*, and *5e⁺(T)* species with the CASPT3 (Werner 1996; Celani & Werner 2000) and MRCI methods (Werner & Knowles 1988; Knowles & Werner 1988). The *5d⁺(S)* and *5e⁺(S)* isomers were not considered at this stage because the CASSCF results indicate too-high excitation energies of 4.6 eV for the lowest *a*-type transitions (see § A1). The active space, including seven orbitals (five π -orbitals perpendicular to the molecular plane, and two in-plane orbitals), was used with seven electrons for a neutral radical and six for a cation. The vertical and adiabatic transition energies are given in Table 2. The transitions $2^2A_2 \leftarrow 2^2B_1$ of *5d^N(D)* and $3^1A_1 \leftarrow 3^1B_2$ of *5d⁺(T)* (both in *C_{2v}* symmetry) have adiabatic excitation energies of 2.72 and 2.75 eV, respectively, at the CASPT3 level of theory, which are close to the experimental value of 2.80 eV. The same transitions of *5e^N(D)* are 0.02 eV lower than those of *5d^N(D)* (CASPT3). This is an additional reason for the assignment of the 4429 Å CRD band. The smallest differences between vertical and adiabatic excitation energies predicted for *5d^N(D)*, *5e^N(D)*, *5d⁺(T)*, and *5e⁺(T)* are consistent with the analysis of the rotational profile and may suggest a small geometry change upon electronic excitation. We searched for a transition up to 2400 cm⁻¹ to the blue

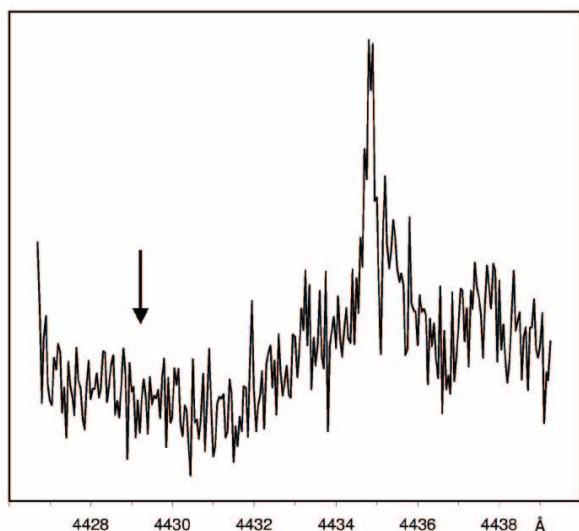


FIG. 5.—Absorption spectrum recorded through a benzene plasma at mass 65 amu (C₅H₅) in the 4429 Å region using a two-laser photon excitation scheme. A 2125 Å laser was used for the ionization step. The 4435 Å band detected has a profile similar to that of the 4429 Å band in the CRD spectrum of Fig. 1. Position of the 4429 Å band in the CRD spectrum is indicated by the arrow.

TABLE 2
ELECTRONIC TRANSITION ENERGY CALCULATED AT THE MRCI AND CASPT3 LEVEL OF THEORY FOR THE A-TYPE TRANSITION

Isomer ^a	Transition	Method	Adiabatic ^b (eV)	Vertical (eV)	(Vertical) – (Adiabatic) (eV)
Observed	2.80
$5a^N$	${}^2A''-{}^2A''$	CASPT3	2.39	2.64	0.25
		MRCI	2.42	2.69	0.27
		MRCI+D	2.40	2.66	0.26
$5d^N(D)$	$2^2A_2-{}^2B_1$	CASPT3	2.72	2.87	0.15
		MRCI	2.68	2.84	0.16
		MRCI+D	2.65	2.84	0.19
$5d^N(Q)$	${}^4B_1-{}^4A_2$	CASPT3	2.62	2.84	0.22
		MRCI	2.61	2.83	0.22
		MRCI+D	2.62	2.84	0.22
$5d^+(T)$	${}^3A_1-{}^3B_2$	CASPT3	2.75	2.93	0.18
		MRCI	2.86	3.06	0.20
		MRCI+D	2.81	2.98	0.17
$5e^N(D)$	$2^2A_2-{}^2B_1$	CASPT3	2.70	2.87	0.17
		MRCI	2.64	2.81	0.17
		MRCI+D	2.62	2.81	0.21
$5e^N(Q)$	${}^4B_1-{}^4A_2$	CASPT3	2.63	2.85	0.22
		MRCI	2.63	2.85	0.22
		MRCI+D	2.63	2.86	0.23
$5e^+(T)$	${}^3A_1-{}^3B_2$	CASPT3	2.72	2.89	0.17
		MRCI	2.82	2.97	0.15
		MRCI+D	2.78	2.95	0.17
$5b^+$	${}^1B_2-{}^1A_1$	CASPT3	3.06	3.39	0.33
		MRCI	3.20	3.51	0.31
		MRCI+D	3.02	3.31	0.29

NOTE.—The geometries are optimized at the CASPT3 level of theory. For computational details see Appendix.

^a See Fig. 4.

^b Adiabatic transition energies without zero vibrational level correction.

of the 4429 Å band using the CRD spectrometer. However, no band that would correspond to vibrational excitation in the upper electronic state was observed in this region either by us or in the study of Ball et al. (2000). Thus the origin band dominates the transition, and the geometry change appears to be small.

Rotational constants in the ground and excited states were calculated at the CASPT3 level of theory by numerical geometry optimization and are given in Table 3. The simulation of the rotational profile of the 4429 Å band suggests that the rotational constants change less than 1% between the two states. The calculated differences in the cases of $5d^N(D)$, $5e^N(D)$ and $5d^N(Q)$, $5e^N(Q)$ agree with the simulation within the errors, and the

values of ΔA in the cases of $5a^N$, $5b^+$, $5d^+(T)$, and $5e^+(T)$ are too large.

Good agreement with the experimental data of the 4429 Å CRD band is predicted for the $2^2A_2 \leftarrow {}^2B_1$ transitions of $5d^N(D)$ and $5e^N(D)$, although it is slightly better for the first one with all considered criteria. From the candidates discussed we conclude that the $5d^N(D)$ isomer, “planar W structure” with five carbons in C_{2v} symmetry (Fig. 4), a doublet radical, is the most likely carrier of the 4429 Å laboratory band.

This work has been supported by the Swiss National Science Foundation (project 200020-100019).

TABLE 3
ROTATIONAL CONSTANTS CALCULATED AT THE CASPT3 LEVEL OF THEORY

Isomer ^a	Transition	A (cm^{-1})	B (cm^{-1})	C (cm^{-1})	ΔA^b (%)	ΔB^b (%)	ΔC^b (%)
$5a^N$	${}^2A''-{}^2A''$	1.235	0.0742	0.0700	–16	1	0
$5d^N(D)$	$2^2A_2-{}^2B_1$	1.381	0.0792	0.0749	–5	–2	–2
$5d^N(Q)$	${}^4B_1-{}^4A_2$	1.378	0.0793	0.0750	–4	–3	–3
$5d^+(T)$	${}^3A_1-{}^3B_2$	1.201	0.0828	0.0775	11	–4	–5
$5e^N(D)$	$2^2A_2-{}^2B_1$	1.079	0.0827	0.0768	–4	–2	–2
$5e^N(Q)$	${}^4B_1-{}^4A_2$	1.082	0.0827	0.0768	–4	–2	–2
$5e^+(T)$	${}^3A_1-{}^3B_2$	0.963	0.0865	0.0794	13	–6	–4
$5b^+$	${}^1B_2-{}^1A_1$	0.452	0.1288	0.1003	–21	2	11

NOTE.—For computational details see Appendix. Rotational constants A , B , and C are in the ground state.

^a See Fig. 4.

^b Differences of rotational constants between the ground and excited states.

APPENDIX

COMPUTATIONAL RESULTS AND DETAILS

DFT (B3LYP) geometry optimization and frequency calculation were carried out for the ground state of all molecules, and no imaginary vibrational frequencies were obtained for the investigated ground states. Thus time-dependent perturbation treatment (TD-DFT) was used to calculate vertical excitation energies and transition dipole moments to the first and second electronically excited states (Table 1), although the TD-DFT method is not applicable if the ground state is not characterized by a single configuration and/or if there is a significant contribution of double excitations in the excited state configuration. Therefore the $5d^N(D)$, $5d^N(Q)$, $5d^+(S)$, $5d^+(T)$, and relevant $5e$ isomers were considered separately using the CASSCF method (see §§ A1 and A2). All calculations were done with a cc-pVDZ basis set.

In the CASSCF, CASPT3, and MRCI calculations the active space included five π -orbitals perpendicular to the molecular plane and two in-plane orbitals, with seven electrons for neutral radicals and six electrons for cations. In the case of $5a^N$ the two in-plane orbitals are π and π^* orbitals of the C3≡C4 triple bond; for $5b^+$ the two in-plane orbitals are the σ_{HOMO} and σ^*_{LUMO} orbitals localized on the three-membered ring. The two in-plane orbitals of the $5d$ isomers are symmetric and antisymmetric combination of two carbon lone-pair orbitals of C1 and C5 carbon atoms. The above choice was preceded by the CASSCF calculations with larger active space, since other orbitals are inactive for the states of interest (the corresponding CI coefficients are smaller than 0.05). In the CASPT3 and MRCI calculations the core orbitals were not correlated. For $5b^+$, $5d$, and $5e$, calculations were executed in a C_{2v} symmetry point group.

The results of CASSCF calculations for manifold excited states of $5d^N$ and $5d^+$ are presented in § A1. These allowed us to identify the excited states of the required adiabatic excitation energies and orientations of the transition dipole moments. The electronic configuration of the ground and excited states of interests are discussed in § A2. The electronic structures and spectroscopic parameters of $5d$ and $5e$ are very similar. The total energy of the $5e^N(D)$, 2B_1 , is 0.02 eV higher than that of $5d^N(D)$, and the two excitation energies differ by not more than ± 0.04 eV. Therefore only the data of $5d$ are listed here. The vertical and adiabatic excitation energies (Table 3) were calculated using CASPT3, MRCI, and MRCI with Davidson correction (MRCI+D) methods for geometries optimized numerically using the CASPT3 method.

A1. ELECTRONICALLY EXCITED STATES OF THE $5D$ MOLECULES

The CASSCF calculations of vertical and adiabatic excitation energies (without ZPE correction) were performed for two states from each irreducible representation of the C_{2v} point group, for each form of the $5d$ molecules: $5d^N(D)$, $5d^N(Q)$, $5d^+(S)$, and $5d^+(T)$. That states cover the energy range up to 4–5 eV. The transition of interest should possess an excitation energy close to the experimental value of 2.80 eV, the required b_2 symmetry (a -type transition), and a significant intensity.

The only relevant transition of $5d^N(D)$ is the $2^2A_2 \leftarrow {}^2B_1$ excitation at 2.67 eV (Table A1). A significant transition moment is predicted also for the excitations to the 2A_1 and 2^2A_1 states (excitation energies 1.29 and 4.16 eV). For the $5d^N(Q)$ isomer only the ${}^4B_1 \leftarrow X^4A_2$ excitation is at 2.53 eV (Table A2). A noticeable transition moment is predicted also for the excitations to the 4B_2 state (3.40 eV). In the case of $5d^+(S)$, all allowed transitions shown in Table A3 possess rather large transition moments, but the excitation energy of the transitions of the required symmetry (${}^1B_2 \leftarrow X^1A_1$ and $2^1B_2 \leftarrow X^1A_1$) is too high. All allowed transitions for $5d^+(T)$ shown in Table A4 have rather large transition moments, except for $2^3A_1 \leftarrow {}^3B_2$. Among them the ${}^3A_1 \leftarrow {}^3B_2$ transition has the required symmetry and excitation energy of 2.93 eV. Both the 3A_1 and 3B_2 states are energetically well separated from other triplet states.

A2. ELECTRONIC STRUCTURE OF THE SELECTED MOLECULES

A2.1. $5a^N$ and $5b^+$ Isomers

The main configuration of $5a^N$ in the ground state is 22+00 (0.93), where we show the occupations of the five $\pi a''$ active orbitals, with the coefficient given in parentheses, and for the excited state the configurations are 2+200 (0.54), 220+0 (0.49), and 2+-+0 (0.32).

TABLE A1
CASSCF EXCITATION ENERGIES AND TRANSITION MOMENTS FOR THE DOUBLET RADICAL $5d^N(D)$

STATE	EXCITATION ENERGY		TRANSITION MOMENT	
	Vertical (eV)	Adiabatic ^a (eV)	Direction	Value (D)
2B_1
2A_2	0.64	0.62	<i>a</i>	-0.025
2B_2	1.46	1.19	...	Forbidden
2A_1	1.58	1.29	<i>c</i>	-0.241
2^2A_2	2.84	2.67	<i>a</i>	0.263
2^2B_1	3.44	3.27	<i>b</i>	0.046
2^2A_1	4.42	4.16	<i>c</i>	-0.625
2^2B_2	4.51	4.21	...	Forbidden

^a Adiabatic transition energies without ZPE correction.

TABLE A2
CASSCF EXCITATION ENERGIES AND TRANSITION MOMENTS FOR QUARTET RADICAL $5d^N(Q)$

STATE	EXCITATION ENERGY		TRANSITION MOMENT	
	Vertical (eV)	Adiabatic ^a (eV)	Direction	Value (D)
X^4A_2
4B_1	2.79	2.53	<i>a</i>	-0.218
4A_1	3.76	3.33	...	Forbidden
4B_2	3.88	3.40	<i>c</i>	-0.263
2^4A_2	4.43	4.17	<i>b</i>	0.017
2^4B_1	5.18	4.71	<i>a</i>	-0.049
2^4B_2	6.03	5.49	<i>c</i>	-0.102
2^4A_1	6.13	5.55	...	Forbidden

^a Adiabatic transition energies without ZPE correction.

TABLE A3
CASSCF EXCITATION ENERGIES AND TRANSITION MOMENTS FOR SINGLET CATION $5d^+(S)$

STATE	EXCITATION ENERGY		TRANSITION MOMENT	
	Vertical (eV)	Adiabatic ^a (eV)	Direction	Value (D)
X^1A_1
1B_1	3.28	2.27	<i>c</i>	-0.473
1A_2	3.49	2.73	...	Forbidden
2^1A_1	3.80	3.61	<i>b</i>	-0.625
2^1B_1	4.66	4.58	<i>c</i>	0.533
1B_2	4.79	4.61	<i>a</i>	6.774
2^1A_2	4.83	4.67	...	Forbidden
2^1B_2	5.34	5.25	<i>a</i>	0.529

^a Adiabatic transition energies without ZPE correction.

TABLE A4
CASSCF EXCITATION ENERGIES AND TRANSITION MOMENTS FOR TRIPLET CATION $5d^+(T)$

STATE	EXCITATION ENERGY		TRANSITION MOMENT	
	Vertical (eV)	Adiabatic ^a (eV)	Direction	Value (D)
3B_2
2^3B_2	2.55	2.34	<i>b</i>	-0.360
3B_1	2.62	1.67	...	Forbidden
3A_2	2.87	2.16	<i>c</i>	0.438
3A_1	3.14	2.93	<i>a</i>	0.518
2^3B_1	4.18	4.06	...	Forbidden
2^3A_1	4.37	4.16	<i>a</i>	0.012
2^3A_2	4.42	4.21	<i>c</i>	-0.546

^a Adiabatic transition energies without ZPE correction.

TABLE A5
 TOTAL ENERGY DIFFERENCE FOR THE LOWEST STATES OF $5d$

METHOD	ΔE^a (eV)	
	Neutral Radical ${}^2B_1-X^4A_2$	Cation $X^1A_1-{}^3B_2$
CASSCF ^b	0.26	-0.05
CASPT3 ^c	0.22	-0.05
MRCI ^c	0.23	-0.07
MRCI+D ^c	0.21	-0.06

^a Energies without ZPE correction.

^b Geometry optimized with the CASSCF method.

^c Geometry optimized numerically with the CASPT3 method.

In the case of $5b^+$ in the ground state, these are 200 20 (0.88) and the doubly excited configuration 220 00 (0.39), where we show the occupation of the π -orbitals (three b_1 and two a_2 orbitals), and in the excited state the configurations are 2+0 -0 (+0.64) and 2-0 +0 (-0.64).

A2.2. $5d^N$ and $5d^+$ Isomers

The electronic structure of $5d^N$ and $5d^+$ is more complicated because of the presence of two lone-pair orbitals of carbon atoms C1 and C5 occupied by two electrons. The symmetric and antisymmetric combinations of these orbitals are almost degenerate. The energy difference between the triplet 3B_2 and singlet X^1A_1 states of the $5d^+$ cation is small, 0.05–0.07 eV with all methods (Table A5). The energy of the b_2 excitation (a -type transition) of the singlet cation $5d^+(S)$ is rather high, about 4.8 eV vertical and 4.6 eV adiabatic at the CASSCF level, and therefore this molecule was excluded from investigation with the CASPT3 and MRCI methods. The quartet X^4A_2 state is the lowest energy form of the $5d^N$ radical; the energy of the lowest doublet state 2B_1 is 0.21–0.26 eV higher with all methods (Table A5).

The ground-state wavefunctions of the high-spin forms, $5d^N(Q)$ and $5d^+(T)$, are dominated by a single electronic configuration: + 2+0 + 20 (0.94), where we show the occupations of the a_1 carbon lone pair, three b_1 π -orbitals, the b_2 carbon lone pair, and two a_2 π -orbitals, for the quartet radical, and + 200 + 20 (0.94) for the triplet cation. In case of the low-spin forms there are two main configurations of the ground-state wavefunction: 2 200 0 20 (+0.71) and 0 200 2 20 (-0.61) for the singlet cation, and 2 2+0 0 20 (0.66) and 0 2+0 2 20 (0.62) for the doublet radical.

The excited states of interests represent essentially $\pi-\pi^*$ transitions of b_2 symmetry, although the contribution of the promotion of electrons between the carbon lone-pair orbitals a_1 and b_2 is noticeable, except for the $5d^+(T)$ molecule. The wavefunction of the latter molecule in the excited state 3A_1 is mainly a combination of four configurations 1 210 1 10 with all possible spin directions with absolute values of coefficients 0.42–0.50.

The excited-state wavefunction for $5d^N(Q)$ consists of two main configurations: + 220 + +0 (0.60) and + 200 + 2+ (0.57), which represent a $\pi-\pi$ transition. Two other configurations, 2 2+0 0 ++ (-0.25) and 0 2+2 2 ++ (+0.25) indicate the contribution of the excitation between the carbon lone-pair orbitals.

The first excitation $1^2A_2 \leftarrow {}^2B_1$ of the $5d^N(D)$ doublet radical has an energy of only 0.61 eV (adiabatic transition, CASPT3). That excitation is mainly a promotion of one electron between the carbon lone-pair orbitals a_1 and b_2 . The $2^2A_2 \leftarrow {}^2B_1$ transition

 TABLE A6
 GEOMETRY AND ROTATIONAL CONSTANTS COMPUTED WITH CASSCF FOR THE $5d$ ISOMER

PARAMETER	$5d^N(D)$		$5d^N(Q)$		$5d^+(T)$	
	2B_1	2^2A_2	4A_2	4B_1	3B_2	3A_1
Bond length (Å)						
C1-C2.....	1.362	1.420	1.365	1.443	1.353	1.405
C2-C3.....	1.422	1.418	1.417	1.404	1.413	1.402
C1-H1.....	1.080	1.079	1.080	1.080	1.081	1.080
C2-H2.....	1.088	1.086	1.088	1.086	1.085	1.087
C3-H3.....	1.082	1.083	1.083	1.084	1.084	1.082
Angle (deg)						
C1-C2-C3.....	124.594	124.175	124.463	123.813	118.811	123.568
C2-C3-C4.....	122.991	123.462	123.243	124.068	124.156	120.548
H1-C1-C2.....	132.317	132.263	131.727	130.056	134.829	134.303
H2-C2-C3.....	117.699	118.644	117.841	119.009	120.314	119.277
H3-C3-C2.....	118.505	118.269	118.378	117.966	117.922	119.726
Rotational constant (GHz)						
A	41.601	40.175	41.487	39.440	36.686	40.457
B	2.397	2.333	2.403	2.334	2.517	2.406
C	2.266	2.205	2.272	2.203	2.356	2.271

TABLE A7
 GEOMETRY AND ROTATIONAL CONSTANTS COMPUTED WITH CASPT3 FOR THE $5d$ ISOMER

PARAMETER	$5d^N(D)$		$5d^N(Q)$		$5d^+(T)$	
	2B_1	2^2A_2	4A_2	4B_1	3B_2	3A_1
Bond length (Å)						
C1-C2.....	1.365	1.442	1.368	1.443	1.364	1.413
C2-C3.....	1.429	1.408	1.425	1.411	1.422	1.417
C1-H1.....	1.092	1.090	1.092	1.092	1.096	1.095
C2-H2.....	1.104	1.096	1.103	1.099	1.100	1.103
C3-H3.....	1.094	1.089	1.095	1.095	1.098	1.094
Angle (deg)						
C1-C2-C3.....	124.972	123.803	124.853	124.262	118.802	123.766
C2-C3-C4.....	122.567	122.887	122.884	123.960	123.754	119.731
H1-C1-C2.....	134.705	134.863	134.210	132.500	137.062	135.728
H2-C2-C3.....	117.307	119.027	117.484	118.577	120.464	119.073
H3-C3-C2.....	118.717	118.556	118.558	118.020	118.123	120.134
Rotational constant (GHz)						
<i>A</i>	41.406	39.410	41.304	39.489	36.015	39.873
<i>B</i>	2.374	2.327	2.377	2.310	2.482	2.365
<i>C</i>	2.245	2.197	2.248	2.182	2.322	2.233

has an excitation energy of 2.72 eV (adiabatic transition, CASPT3), which is close to the experimental value of 2.80 eV and is a promotion of an electron within the π -system from two main configurations of the ground state. The wavefunction of the excited state 2^2A_2 is primarily a combination of four configurations: $2\ 220\ 0\ +0$, $0\ 220\ 2\ +0$, $2\ 200\ 0\ 2+$, and $0\ 200\ 2\ 2+$, with absolute values of coefficients 0.34–0.39.

A3. EQUILIBRIUM GEOMETRIES OF $5d^N(D)$, $5d^N(Q)$, AND $5d^+(T)$

The geometry parameters and rotational constants were optimized with the CASSCF and CASPT3 methods (Tables A6 and A7, respectively) in C_{2v} symmetry. The vibrational frequencies of the initial states (the lowest state for each multiplicity) were calculated numerically with the CASSCF methods in reduced C_1 symmetry. No imaginary frequencies are present. Efforts were made to calculate the vibrational frequencies of the excited states, but these were not successful because of numerical and convergence problems. Nevertheless, the geometry optimization of the excited states within C_{2v} symmetry seems to be justified, since the excited states of interest are energetically well separated from the neighbor states (Tables A1–A4).

REFERENCES

- Araki, M., Linnartz, H., Cias, P., Denisov, A., Fulara, J., Batalov, A., Shnitko, I., & Maier, J. P. 2003, *J. Chem. Phys.*, 118, 10561
- Araki, M., Ozeki, H., & Saito, S. 1999, *Mol. Phys.*, 97, 177
- Ball, C. D., McCarthy, M. C., & Thaddeus, P. 2000, *ApJ*, 529, L61
- Bazalgette Courrèges-Lacoste, G., Sprengers, J. P., Bulthuis, J., Stolte, S., Motylewski, T., & Linnartz, H. 2001, *Chem. Phys. Lett.*, 335, 209
- Celani, P., & Werner, H.-J. 2000, *J. Chem. Phys.*, 112, 5546
- Ding, H., Schmidt, T. W., Pino, T., Boguslavskiy, A. E., Güthe, F., & Maier, J. P. 2003, *J. Chem. Phys.*, 119, 814
- Frisch, M. J., et al. 2003, *Gaussian 03* (rev. A.1; Pittsburgh: Gaussian, Inc.)
- Greenberg, K. E., & Hargis, P. J., Jr. 1990, *J. Appl. Phys.*, 68, 505
- Herbig, G. H. 1975, *ApJ*, 196, 129
- Jenniskens, P., & Désert, F.-X. 1994, *A&AS*, 106, 39
- Knowles, P. J., & Werner, H.-J. 1988, *Chem. Phys. Lett.*, 145, 514
- Kotterer, M., Conceicao, J., & Maier, J. P. 1996, *Chem. Phys. Lett.*, 259, 233
- Luckhaus, D., & Quack, M. 1989, *Mol. Phys.*, 63, 745
- Motylewski, T., et al. 2000, *ApJ*, 531, 312
- O’Keefe, A., & Deacon, D. A. G. 1988, *Rev. Sci. Instrum.*, 59, 2544
- Snow, T. P. 2002, *ApJ*, 567, 407
- Snow, T. P., Zukowski, D., & Massey, P. 2002, *ApJ*, 578, 877
- Thaddeus, P., & McCarthy, M. C. 2001, *Spectrochim. Acta A*, 57, 757
- Tielens, A. G. G. M., & Snow, T. P., eds. 1995, *The Diffuse Interstellar Bands* (Dordrecht: Kluwer)
- Tuairisg, S. Ó., Cami, J., Foing, B. H., Sonnentrucker, P., & Ehrenfreund, P. 2000, *A&AS*, 142, 225
- Werner, H.-J. 1996, *Mol. Phys.*, 89, 645
- Werner, H.-J., & Knowles, P. J. 1988, *J. Chem. Phys.*, 89, 5803
- . 2003, *MOLPRO* (Birmingham: Univ. Birmingham)
- Zelinger, Z., Amano, T., Ahrens, V., Brünken, S., Lewen, F., Müller, H. S. P., & Winnenwiser, G. 2003, *J. Mol. Spectrosc.*, 220, 223

Rotational analysis of the $\tilde{A}^2B_1 \leftarrow \tilde{X}^2A_2$ electronic spectrum of the allyl radical

ELENA ACHKASOVA, MITSUNORI ARAKI, ALEXEY DENISOV and JOHN P. MAIER*

Department of Chemistry, University of Basel
Klingelbergstrasse 80, CH-4056 Basel, Switzerland

(Received 19 October 2004; in final form 25 November 2004)

The rotationally resolved $\tilde{A}^2B_1 \leftarrow \tilde{X}^2A_2$ electronic spectra of the allyl radical C_3H_5 and its isotopic derivative C_3D_5 have been recorded in the gas phase by cavity ring down spectroscopy through a supersonic planar plasma. A rotational analysis yields accurate molecular constants for the first excited electronic state with $T_{00} = 24491.2292(80)$ for C_3H_5 . A C_{2v} planar structure in the zero-point level is indicated. The obtained rotational constants were employed to determine the C–C bond length 1.48 Å and the CCC bond angle 123° in the 2B_1 electronic state. Two other bands observed are assigned to the excitation of the ν_7 (339 cm^{-1}) and ν_9 (101 cm^{-1}) vibrational modes in the upper electronic state.

Introduction

The allyl radical is the simplest π -alternant hydrocarbon system and a prototype for more complex conjugated molecules with an odd number of electrons. Further interest comes from its abundance in reactive processes such as those involving combustion [1] and photochemistry [2]. In this context detailed knowledge of the molecular structure and vibrational behaviour of this radical is important and thus a subject for study by high resolution spectroscopy.

Electronic states of C_3H_5 have been studied experimentally and theoretically over the past four decades. The first experimental data were obtained by Currie and Ramsay who observed diffuse absorption bands in the 370–410 nm range during flash photolysis of some allylic compounds [3]. The system was assigned to the $\tilde{A}^2B_1 \leftarrow \tilde{X}^2A_2$ electronic transition with band origin at 408.3 nm. This transition was also observed in an argon matrix [4]. Fessenden and Schuler showed by electron spin resonance that the allyl radical has C_{2v} symmetry in the ground state [5]. Geometrical parameters in the ground state were calculated using different theoretical models [6–10]. A rotational analysis of the ν_{11} vibrational band in the infrared (IR) spectrum yielded experimental values of the geometrical parameters [11]. The spectral properties of states lying above the first excited state A have been studied by resonant Raman and resonance-enhanced multiphoton ionization

spectroscopies [12–18]. Recently Tonokura and Koshi remeasured the electronic absorption spectrum of the $\tilde{A}^2B_1 \leftarrow \tilde{X}^2A_2$ transition by a cavity ring down method resolving well the vibrational structure [6]. They also carried out CASSCF calculations with a TZV(d,p) basis set and reported a C_{2v} structure for the first excited state with one imaginary frequency. This anomaly was rationalized by suggesting that in the first excited state the structure has a twisted C_2 symmetry leading to additional interactions. They measured several vibronic bands which were rotationally not resolved in the $\tilde{A}^2B_1 \leftarrow \tilde{X}^2A_2$ transition and tentatively assigned some of them. Despite the observation of many strong vibronic bands, no progressions were evident.

In the present work the rotationally resolved $\tilde{A}^2B_1 \leftarrow \tilde{X}^2A_2$ electronic spectra of C_3H_5 and C_3D_5 in the gas phase have been measured by cavity ring down spectroscopy using a supersonic planar plasma for the radical generation. The rotational analysis of the origin band allowed accurate molecular constants for the first excited state to be obtained, indicating an effective structure with C_{2v} symmetry. Geometrical parameters of the allyl radical in the 2B_1 state were determined from the inferred constants. Two vibronic bands were also observed in high resolution and assigned to the ν_7 and ν_9 vibrational modes.

2. Experimental

The experiment consisted of a cavity ring down set-up sampling a plasma generated in a pulsed supersonic slit

*Corresponding author. Email: j.p.maier@unibas.ch

jet with dimensions of $3\text{ cm} \times 300\text{ }\mu\text{m}$ [19]. The source was located in a vacuum chamber evacuated by a roots blower. The C_3H_5 (C_3D_5) radicals were synthesized in the discharge of a gas pulse (30 Hz repetition rate, 10 bar backing pressure, 100 mA at -600 V applied voltage) of 0.3% C_2H_2 (C_2D_2) in an Ar mixture. The radicals are cooled in the supersonic expansion to about 40 K at 2 mm downstream from the slit.

The excimer pumped dye laser system used had $\sim 0.06\text{ cm}^{-1}$ linewidth with an etalon, or 0.15 cm^{-1} without it. The light leaking out of the ring down cavity was detected by a photodiode. The spectra were calibrated using a wavemeter.

3. Results and discussion

The origin band of the $\tilde{\text{A}}^2\text{B}_1 \leftarrow \tilde{\text{X}}^2\text{A}_2$ electronic transition of the allyl radical lies at 408.2 nm. The rotational structure could be reasonably resolved using a laser linewidth of 0.06 cm^{-1} and is shown in figure 1 (trace c). The rotational pattern shows that it corresponds to an a-type transition. The spectrum shows P- and R-branches, but the lines are partially blended by absorption features of other carbon molecules produced in the discharge. In order to identify the interfering lines, the spectrum was recorded using a 0.5% mixture of C_3H_4 in neon which does not favour C_3H_5 formation (trace d in figure 1). Subtraction of the spectra obtained under such conditions (trace c minus d in figure 2) simplified the identification of the rotational lines belonging to the allyl radical.

Initially a rough rotational analysis was carried out using *ab initio* calculated geometries of the excited state (both in C_2 and C_{2v} symmetry) [6]. These constants are listed in table 1 and were then used to simulate the rotational profile using the program called ‘Wang’ [20]. The resulting spectra with *ab initio* C_2 and C_{2v} geometries in the excited state of C_3H_5 at a rotational temperature 40 K are shown in traces a and b of figure 1. As can be seen no agreement with the experimental spectrum is obtained for C_2 symmetry in the excited state. On the other hand the spectrum predicted with C_{2v} geometry in the upper state matches reasonably.

In the next step a more detailed rotational assignment was made with C_{2v} upper state symmetry. P-branch lines with $K_a = 0$ and 2 were assigned. Except in the $K_a = 0$ ladder, all rotational lines show asymmetry splitting (see inset in figure 2) which increases with the quantum number N . A least-squares fit to the frequencies of the 16 lines listed in table 2 was made with a conventional rotational Hamiltonian for an asymmetric top molecule without centrifugal distortion terms using the program ‘Wang’ [20]. Spectroscopic constants for the excited state and transition energy determined from the analysis are listed in table 1. The simulated spectrum (trace e in figure 2) with the obtained molecular constants agrees well with the observed spectrum.

The successful rotational analysis suggests that the allyl radical has a planar C_{2v} structure in the zero-point level of the $\tilde{\text{A}}$ state because the obtained constants are close to those predicted by *ab initio* calculations for C_{2v} rather than C_2 symmetry. The inertial defect,

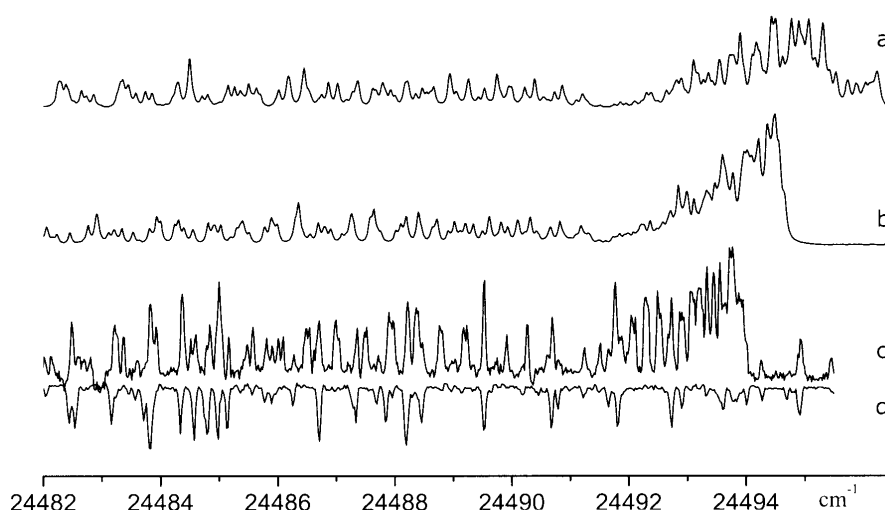


Figure 1. Rotationally resolved electronic absorption spectrum (0.06 cm^{-1} resolution) of the origin band in the $\tilde{\text{A}}^2\text{B}_1\text{-}\tilde{\text{X}}^2\text{A}_1$ transition of C_3H_5 measured by CRD spectroscopy using acetylene as precursor (trace c), or allene (trace d) in the plasma discharge. Traces a and b are the simulated rotational profiles within C_2 and C_{2v} symmetries, respectively, at 40 K.

$\Delta = I_C - I_A - I_B$, in the ground state is small, 0.0539 amu \AA^2 , indicating a planar structure [11]. For the excited state it is $-0.048 \pm 0.434 \text{ amu \AA}^2$, where the error is derived from the uncertainty in the determined rotational constants. The similarity of the inertial defect for the ground and excited state, and both being close to zero, leads to the conclusion that the molecule has an effective planar structure in the \tilde{A} state. This result is consistent with the *ab initio* results that the equilibrium structure in the excited state of this molecule has

C_2 symmetry [6], but the zero-point level may be energetically higher than the potential barrier of 371 cm^{-1} , sandwiching the C_{2v} structure between the C_2 structures. The difference between the zero-point and equilibrium structures is due to the vibrations and anharmonicity of the potential.

The rotational constants obtained were used to determine the C–C distance and CCC angle in the excited state of the allyl radical. Five structural parameters involving hydrogens were fixed to the *ab initio*

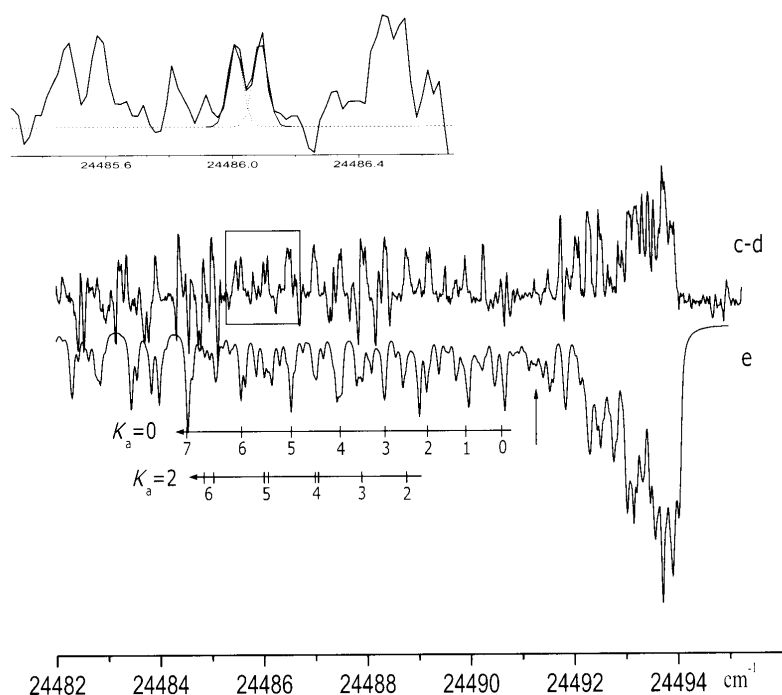


Figure 2. Rotationally resolved electronic absorption spectrum of the origin band in the $\tilde{A}^2B_1\text{--}\tilde{X}^2A_1$ transition of C_3H_5 after subtraction of the spectrum observed using an allene plasma (i.e. trace c minus d) and the simulation (trace e) at 40 K. The inset demonstrates the asymmetric splitting of the line with $K_a = 5$ and $N = 5$. The arrow indicates the determined band origin.

Table 1. Molecular constants for C_3H_5 (cm^{-1}).^a

	This work	IR ^b	<i>Ab initio</i> ^c		
			\tilde{X}^2A_2	$\tilde{A}^2B_1(C_{2v})$	$\tilde{A}^2B(C_2)$
A''	1.80189 ^d	1.80189(92)	1.831		
B''	0.346320 ^d	0.346320(26)	0.3457		
C''	0.290219 ^d	0.290219(27)	0.2908		
$(B'' + C'')/2$		0.318270(27)			
A'	1.6688(22)			1.706	1.713
$(B' + C')/2$	0.28624(101)			0.2912	0.2966
$(B' - C')/2$	0.02426(101)			0.0247	0.0206
T_{00}	24491.2292(80) ^e				

^aValues in parentheses denote the standard deviation and apply to the last digits of the constants.

^bFrom [11].

^cFrom [6].

^dFixed.

^eThe error from the least-squares fit only.

Table 2. Observed and calculated frequencies (cm^{-1}) of the rovibronic lines for the origin band in the $\tilde{A}^2B_1 - \tilde{X}^2A_1$ electronic transition of C_3H_5 .

$N_{K_a K_c}$	ν_{obs}	ν_{calc}	$\nu_{\text{obs}} - \nu_{\text{calc}}$
$1_{01} - 0_{00}$	24490.605	24490.624	-0.015
$2_{02} - 1_{01}$	24489.911	24489.925	-0.009
$3_{03} - 2_{02}$	24489.170	24489.164	0.010
$3_{22} - 2_{21}$	24488.761	24488.747	0.011
$3_{21} - 2_{20}$	24488.761	24488.741	0.021
$4_{04} - 3_{03}$	24488.349	24488.345	-0.001
$4_{23} - 3_{22}$	24487.898	24487.919	-0.022
$4_{22} - 3_{21}$	24487.898	24487.902	-0.002
$5_{05} - 4_{04}$	24487.480	24487.469	0.010
$5_{24} - 4_{23}$	24487.042	24487.027	0.012
$5_{23} - 4_{22}$	24486.981	24486.992	-0.009
$6_{06} - 5_{05}$	24486.537	24486.539	-0.003
$6_{25} - 5_{24}$	24486.090	24486.073	0.020
$6_{24} - 5_{23}$	24486.009	24486.009	-0.001
$7_{07} - 6_{06}$	24485.577	24485.556	0.017
$7_{26} - 6_{25}$	24485.036	24485.057	-0.024
$7_{25} - 6_{24}$	24484.847	24484.953	-0.103
$8_{08} - 7_{07}$	24484.516	24484.523	-0.004

Table 3. Observed and calculated molecular constants of C_3D_5 .

	Obs.	Calc. ^a	Calc. ^b
A''			1.1108
B''			0.2753
C''			0.2206
$(B'' + C'')/2$			0.2480
A'	1.043	1.043	
$(B' + C')/2$	0.214 ^c	0.225	
T_{00}	24550.60		

^aFrom the obtained structure parameters for C_3H_5 .

^bFrom [11].

^cDetermined by manual fitting.

with previous experimental data [3] which predicted it to be at 404.0 nm, implying a 260 cm^{-1} isotopic shift. In our measurements no band was detected at 404.0 nm. Isotopic shifts of the origin transitions to higher electronic states were reported to be ~ 40 and $\sim 19 \text{ cm}^{-1}$ for the \tilde{B} and \tilde{C} states, respectively [15, 16], consistent with the 59 cm^{-1} value for the origin band of the $\tilde{A}^2B_1 \leftarrow \tilde{X}^2A_2$ system determined in this work. In order to simulate the band profile in the electronic spectrum of C_3D_5 , the rotational constants for the ground state were estimated from the geometric parameters reported for C_3H_5 [11] and those for the \tilde{A}^2B_1 state were from the excited state geometry of C_3H_5 inferred above. These constants produce a rotational profile similar to that observed. Slight variation of the estimated rotational constant $(B' + C')/2$ results in even better agreement. The constants are listed in table 3 and the simulated spectrum is shown in figure 3 (upper trace).

Two bands in the $\tilde{A}^2B_1 \leftarrow \tilde{X}^2A_2$ spectrum corresponding to vibrational excitation in the electronic upper state were detected previously at 24597 and 24838 cm^{-1} [6]. However, these were not rotationally resolved and therefore recorded anew (figures 4 and 5, lower traces). The rotational pattern in the spectra is again of an a-type transition, indicating excitation of a vibrational mode of an a_1 (a) symmetry C_{2v} (C_2) structure. The interpretation that these are transitions from the zeroth level of the \tilde{X}^2A_2 state is supported because the relative intensity of the origin and these two bands is independent of the temperature in the discharge (changed by varying the distance between the nozzle and laser beam).

In order to obtain the frequency ratio ω_D/ω_H for the vibrations in the \tilde{A} state, *ab initio* calculation of the allyl radical was carried out using the CASSCF(3,3) method and a 6-31G(d,p) basis set with the Gaussian program [21]. The calculation was in C_2 symmetry to avoid an imaginary frequency (table 4). Although the basis set is simple, the frequencies of C_3H_5 agree well, within rms

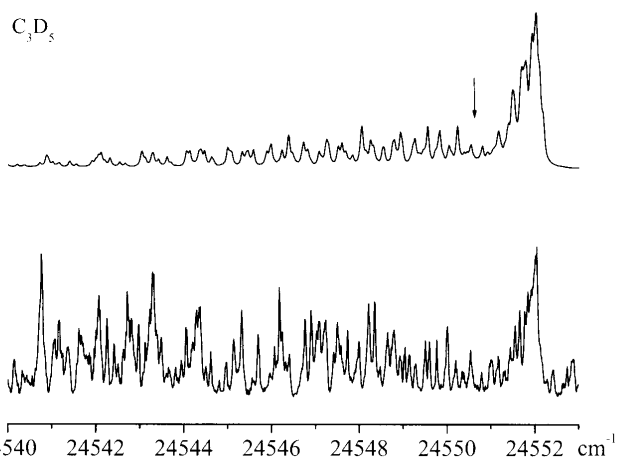


Figure 3. Rotationally resolved electronic absorption spectrum (0.06 cm^{-1} resolution) of the origin band in the $\tilde{A}^2B_1 - \tilde{X}^2A_1$ transition of C_3D_5 (lower trace) and the simulated rotational profile with C_{2v} symmetry at 40 K (upper trace). The arrow indicates the determined band origin.

values [6] in C_{2v} symmetry, $r(C_1H_1) = 1.072 \text{ \AA}$, $r(C_2H_2) = 1.073 \text{ \AA}$, $r(C_2H_3) = 1.071 \text{ \AA}$, $\theta(H_2C_2C_1) = 120.4^\circ$ and $\theta(H_3C_2C_1) = 120.8^\circ$. This leads to the values $r(C_1C_2) = 1.4839 \pm 0.0087 \text{ \AA}$ and $\theta(C_1C_2C_3) = 122.67 \pm 1.21^\circ$.

The origin band in the $\tilde{A}^2B_1 \leftarrow \tilde{X}^2A_2$ electronic transition of the deuterated species C_3D_5 was detected at 407.2 nm , $\sim 59 \text{ cm}^{-1}$ blue shifted with respect to C_3H_5 . The observed rotational profile is shown in figure 3 (lower trace). However, its position is inconsistent

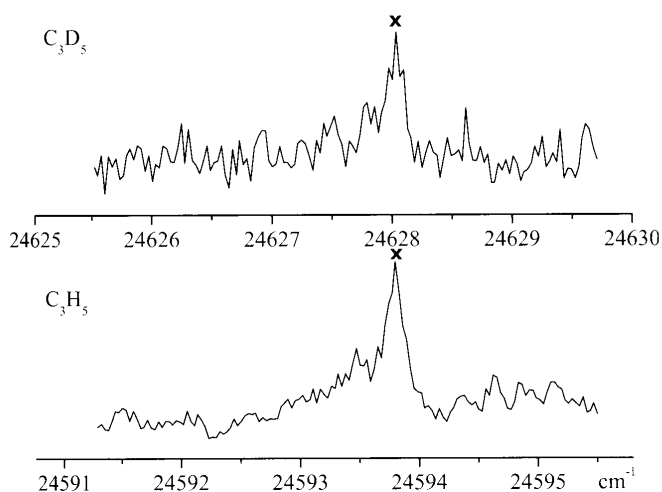


Figure 4. The 9_0^1 band in the $\tilde{A}^2B_1\text{--}\tilde{X}^2A_1$ transition of C_3H_5 and C_3D_5 measured by CRD spectroscopy (0.15 cm^{-1} resolution) using C_2H_2 or C_2D_2 as precursors in the discharge. Band heads of the R-branch are marked with \times .

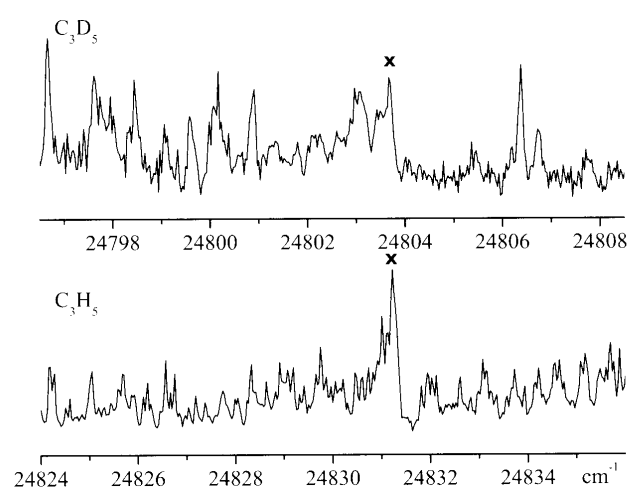


Figure 5. The 7_0^1 band in the $\tilde{A}^2B_1\text{--}\tilde{X}^2A_1$ transition of C_3H_5 and C_3D_5 measured by CRD spectroscopy (0.15 cm^{-1} resolution) using C_2H_2 or C_2D_2 as precursors in the discharge. Band heads of the R-branch are marked with \times .

Table 4. Vibrational frequencies (cm^{-1}) in the \tilde{A}^2B_1 and \tilde{X}^2A_2 states of C_3H_5 and C_3D_5 .

		C_3H_5			C_3D_5		ω_H	ω_H/ω_D	
		ν_{obs}^a	$\Delta\nu$	$\Delta\nu^b$	ν_{obs}^a	$\Delta\nu$	cal	obs	cal ^c
\tilde{A}^2B_1	ν_9	24 592	101	108	24627	76	180 ^c	1.43	1.32
	ν_7	24 830	339	349	24803	252	447 ^c	1.37	1.34
\tilde{X}^2A_2	ν_9		549 ^d			372 ^c	582 ^f	1.48	
	ν_7		427 ^d			350 ^e	448 ^f	1.22	

^aPosition of band origin was extrapolated from the band head of the R-branch.

^bObserved vibrational frequencies in [6].

^cCalculated in C_2 geometry.

^dFrom [17].

^eFrom [22].

^fFrom [10].

of 27 cm^{-1} , with the high-level CASSCF (3,3)/TZV(d,p) calculation [6]. The frequency ratio does not depend on the force constants but only on the reduced mass. Thus the theory with the simpler basis set is sufficient to help the assignment. The theoretical frequency ratios were then used to estimate the positions for the C_3D_5 bands. Two bands were experimentally detected at 24628 and 24804 cm^{-1} (figures 4 and 5, upper traces), in agreement with the *ab initio* prediction. The calculated 447 cm^{-1} frequency of the ν_7 mode in C_2 geometry is higher than the observed one 339 cm^{-1} , but agrees well with 356 cm^{-1} in C_{2v} geometry [6], which is consistent with the C_{2v} planar structure in the zero-point level. The ν_9 mode has the frequency of 101 cm^{-1} in the excited electronic state, although the calculated frequency in C_2 geometry is 180 cm^{-1} . The variation between the calculated and observed values is due to the difference in molecular structure between the zero-point and the equilibrium levels. Therefore the two

vibrational bands in both C_3H_5 and C_3D_5 are assigned to the excitation of the ν_7 and ν_9 vibrational modes in the upper electronic state.

Acknowledgement

This work has been supported by the Swiss National Science Foundation (project 200020-100019/1).

References

- [1] See, for example, K.M. Leung, R.P. Lindstedt. *Combust. Flame.*, **102**, 129 (1995).
- [2] J.M. Tulloch, M.T. Macpherson, C.A. Morgan, M.J. Pilling. *J. phys. Chem.*, **86**, 3812 (1982) and references therein.
- [3] L. Currie, D.A. Ramsay. *J. chem. Phys.*, **45**, 488 (1966).
- [4] G. Maier, H.P. Reisenauer, B. Rohde, K. Dehnicke. *Chem. Ber.*, **116**, 732 (1983).

- [5] R.W. Fessenden, R.H. Schuler. *J. chem. Phys.*, **39**, 2147 (1963).
- [6] K. Tonokura, M. Koshi. *J. phys. Chem. A*, **104**, 8456 (2000).
- [7] O. Kikuchi. *Chem. Phys. Lett.*, **72**, 487 (1980).
- [8] P.G. Szalay, A.G. Csaszar, G. Fogarasi, A. Karpfen, H. Lischka. *J. chem. Phys.*, **93**, 1246 (1990).
- [9] T. Takada, M. Dupuis. *J. Am. chem. Soc.*, **105**, 1713 (1983).
- [10] M. Yamaguchi. *J. molec. Struct. (THEOCHEM)*, **365**, 143 (1996).
- [11] E. Hirota, C. Yamada, M. Okunishi. *J. chem. Phys.*, **97**, 2963 (1992).
- [12] J.W. Hudgens, C.S. Dulcey. *J. phys. Chem.*, **89**, 1505 (1985).
- [13] A.D. Sappay, J.C. Weisshaar. *J. phys. Chem.*, **91**, 3731 (1987).
- [14] D.W. Minsek, J.A. Blush, P. Chen. *J. phys. Chem.*, **96**, 2025 (1992).
- [15] J.A. Blush, D.W. Minsek, P. Chen. *J. phys. Chem.*, **96**, 10150 (1992).
- [16] D.W. Minsek, P. Chen. *J. phys. Chem.*, **97**, 13375 (1993).
- [17] J.D. Getty, X. Liu, P.B. Kelly. *J. phys. Chem.*, **96**, 10155 (1992).
- [18] C.-W. Liang, C.-C. Chen, C.-Y. Wei, Y.-T. Chen. *J. chem. Phys.*, **116**, 4162 (2002).
- [19] H. Linnartz, T. Motylewski, J.P. Maier. *J. chem. Phys.*, **109**, 3819 (1998).
- [20] D. Luckhaus, M. Quack. *Molec. Phys.*, **63**, 745 (1989).
- [21] M.J. Frisch, G.W. Trucks, H.B. Schlegel, G.E. Scuseria, M.A. Robb, J.R. Cheeseman, J.A. Montgomery Jr, T. Vreven, K.N. Kudin, J.C. Burant, J.M. Millam, S.S. Iyengar, J. Tomasi, V. Barone, B. Mennucci, M. Cossi, G. Scalmani, N. Rega, G.A. Petersson, H. Nakatsuji, M. Hada, M. Ehara, K. Toyota, R. Fukuda, J. Hasegawa, M. Ishida, T. Nakajima, Y. Honda, O. Kitao, H. Nakai, M. Klene, X. Li, J.E. Knox, H.P. Hratchian, J.B. Cross, C. Adamo, J. Jaramillo, R. Gomperts, R.E. Stratmann, O. Yazyev, A.J. Austin, R. Cammi, C. Pomelli, J.W. Ochterski, P.Y. Ayala, K. Morokuma, G.A. Voth, P. Salvador, J.J. Dannenberg, V.G. Zakrzewski, S. Dapprich, A.D. Daniels, M.C. Strain, O. Farkas, D.K. Malick, A.D. Rabuck, K. Raghavachari, J.B. Foresman, J.V. Ortiz, Q. Cui, A.G. Baboul, S. Clifford, J. Cioslowski, B.B. Stefanov, G. Liu, A. Liashenko, P. Piskorz, I. Komaromi, R.L. Martin, D.J. Fox, T. Keith, M.A. Al-Laham, C.Y. Peng, A. Nanayakkara, M. Challacombe, P.M.W. Gill, B. Johnson, W. Chen, M.W. Wong, C. Gonzalez, J.A. Pople. Gaussian 03, revision A.1, Gaussian, Inc., Pittsburgh PA (2003).
- [22] X. Liu, J.D. Getty, P.B. Kelly. *J. chem. Phys.*, **99**, 1522 (1993).



Gas phase electronic spectrum of propadienyldiene C₃H₂

Elena Achkasova, Mitsunori Araki, Alexey Denisov, John P. Maier *

Department of Chemistry, University of Basel, Klingelbergstrasse 80, CH-4056, Basel, Switzerland

Received 4 December 2005; in revised form 17 February 2006

Available online 6 March 2006

Abstract

The rotationally resolved vibronic bands in the forbidden $\tilde{A}^1A_2-\tilde{X}^1A_1$ electronic transition of the cumulene carbene C₃H₂ have been observed in the gas phase by cavity ring down absorption spectroscopy through a supersonic planar plasma with allene as precursor. The band detected in the 16223 cm⁻¹ region is a result of vibronic interaction and is assigned to a combination of *a*₁ and *b*₂ vibrations with a frequency around 2250 cm⁻¹. Another vibronic band near 15810 cm⁻¹ has an unusual rotational structure because the *K*_a = 0–1 sub-band is absent. It is assigned to a combination of *a*₁ and *b*₁ vibrations, ~1850 cm⁻¹, which borrow intensity from the near lying \tilde{B}^1B_1 state due to *a*-type Coriolis coupling. A rotational analysis using a conventional Hamiltonian for an asymmetric top molecule yields molecular constants for the vibrational excited levels of the \tilde{A}^1A_2 state, which were used for the determination of the geometry. The stronger $\tilde{B}^1B_1-\tilde{X}^1A_1$ transition of C₃H₂, measured in a neon matrix in the 16161–24802 cm⁻¹ range, was not detected. The reason for this is a short lifetime of the \tilde{B} state, leading to line broadening.

© 2006 Elsevier Inc. All rights reserved.

Keywords: Propadienyldiene C₃H₂; Cavity ring down spectroscopy; Electronic transition; Coriolis coupling

1. Introduction

Interest in investigation of hydrocarbon families like the cumulene carbenes (H₂C(=C)_{*n*}) arises from their relevance in combustion [1] and photochemistry [2,3] processes as well as their detection in the interstellar medium. Several members with *n* = 2–8 have been detected in the laboratory by microwave spectroscopy and *n* = 2, 3, and 5 in dark molecular clouds [4]. In the literature cumulene carbenes have also been suggested as possible diffuse interstellar bands (DIBs) carriers [5]. Consequently, the electronic spectra of these species in the gas phase are required.

The first electronic spectrum of propadienyldiene H₂C=C=C: was recorded in an argon matrix [3] and later on the vibrationally resolved spectrum was observed in solid neon [6]. Three electronic transitions were observed: a strong $\tilde{C}-\tilde{X}$ band system in the 39051–47156 cm⁻¹ range, weaker $\tilde{B}-\tilde{X}$ transition in the 16161–24802 cm⁻¹ region, and the hardly detectable forbidden $\tilde{A}-\tilde{X}$ one at 13885–

16389 cm⁻¹. Based on these observations one can search for these absorptions in the gas phase.

The measured millimetre-wave spectrum of propadienyldiene indicated that the structure in the ground state is a near prolate top with *C*_{2*v*} symmetry [7]. Geometrical parameters were determined from the obtained rotational constants. A vibrational band in the $\tilde{A}^1A_2-\tilde{X}^1A_1$ electronic transition of propadienyldiene (denoted in this work as *b*-band) was detected using a cw cavity ring down technique [8]. The rotational analysis provided geometrical parameters of H₂CCC in the excited ¹*A*₂ state. Because the measured transition is forbidden and occurs on account of vibronic interactions a corresponding DIB would be weak. To have a reliable comparison with DIBs, gas phase measurements of the stronger transition of this molecule are necessary.

In this work, the electronic spectrum of propadienyldiene has been measured using cavity ring down (CRD) spectroscopy. The stronger $\tilde{B}^1B_1-\tilde{X}^1A_1$ transition has not been observed presumably because the short lifetime of the \tilde{B} state leads to broad absorptions which are difficult to detect. Two forbidden vibrational bands in the

* Corresponding author. Fax: +41 61 267 38 55.
E-mail address: j.p.maier@unibas.ch (J.P. Maier).

$\tilde{A}^1A_2-\tilde{X}^1A_1$ system are however seen. The transition at 15813 cm^{-1} gains intensity through *a*-type Coriolis coupling in the excited state, and the one at 16233 cm^{-1} borrows intensity by vibronic coupling with the nearby states of appropriate symmetry. The rotational analysis carried out gives the molecular constants for the excited state, which can be used to calculate a geometrical structure.

2. Experiment

The setup consists of a standard CRD unit which samples the plasma generated in a pulsed supersonic slit jet expansion [9]. The experimental conditions were optimized using the 15982 cm^{-1} vibronic band [8]. Both acetylene and allene seeded in helium or argon were used as a precursor. The highest concentration of propadienylidene was obtained by a discharge through a high pressure gas pulse (30 Hz repetition rate, 10 bar backing pressure, 100 mA at -800 V applied voltage) of a 0.3% $\text{C}_3\text{H}_4/\text{Ar}$ mixture in the throat of a $3\text{-cm} \times 300\text{ }\mu\text{m}$ multilayer slit nozzle. The species are efficiently produced 2 mm down stream from the

slit. The molecules were cooled to about 20 K by the supersonic expansion. An excimer pumped pulsed dye laser with $\sim 0.05\text{ cm}^{-1}$ linewidth with an etalon was used. The spectra were calibrated by using a wavemeter.

3. Results and discussion

3.1. Non-detection of the $\tilde{B}^1B_1-\tilde{X}^1A_1$ transition

The stronger $\tilde{B}^1B_1-\tilde{X}^1A_1$ transition of propadienylidene was observed in a neon matrix in the $16161\text{--}24802\text{ cm}^{-1}$ range [6]. Its origin and vibronic bands between 14877 and 21453 cm^{-1} were searched for in the gas phase by the CRD method. However none were detected. This is attributed to a lifetime broadening in the \tilde{B} state. The intensity of the 3_0^1 band in the $\tilde{B}^1B_1-\tilde{X}^1A_1$ system is about three times stronger than that of the *b*-band at 15982 cm^{-1} . If the 3_0^1 band had a linewidth $>50\text{ cm}^{-1}$ it would not be detected with the absorption method used. This in turn implies that the lifetime is $\leq 50\text{ fs}$. There are several processes which may shorten the lifetime of the \tilde{B} state giving rise to line broadening.

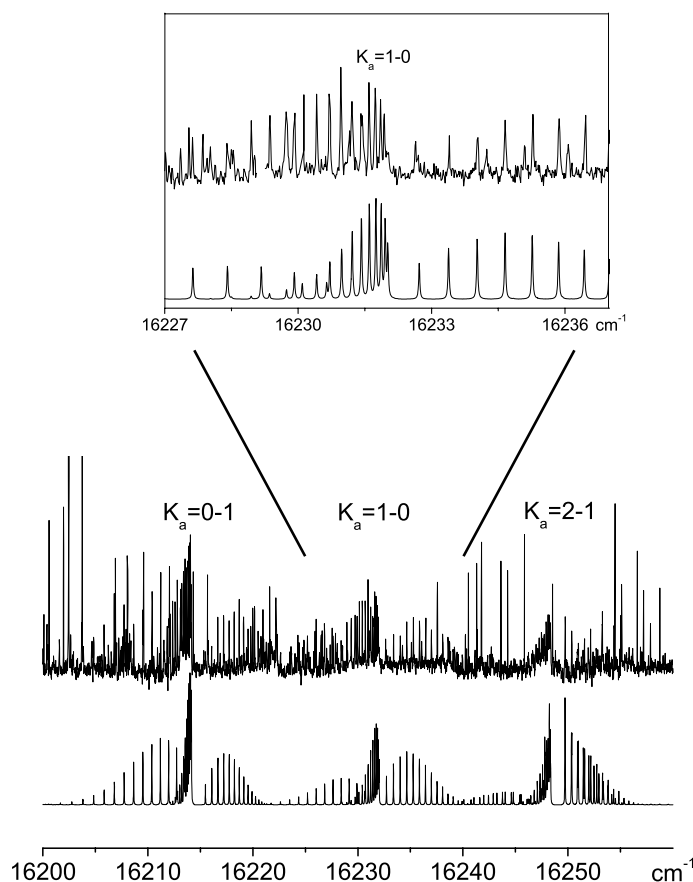


Fig. 1. Rotationally resolved electronic absorption spectrum of the *c*-band in the $\tilde{A}^1A_2-\tilde{X}^1A_1$ transition of H_2CCC (upper trace) and the simulation (lower trace) at 20 K, using a single Boltzmann population model for the two nuclear spin isomers (spin statistical weights *ee:eo:oe:oo* = 1:1:3:3). A small gap at 16229.15 cm^{-1} is an experimental artefact.

Table 1

Frequencies of the observed rovibronic lines for the c -band in the $\tilde{A}^1A_2-\tilde{X}^1A_1$ electronic transition of H_2CCC

J''_{KaKc}	J''_{KaKc}	v_{obs} (cm $^{-1}$)	$o - c$ (cm $^{-1}$)
10 ₀₁₀	—	16204.843	0.000
9 ₀₉	—	16205.833	-0.006
8 ₀₈	—	16206.797	0.008
7 ₀₇	—	16207.738	0.004
6 ₀₆	—	16208.655	0.006
5 ₀₅	—	16209.546	0.020
16 ₀₁₆	—	16211.837	-0.021
15 ₀₁₅	—	16212.111	-0.022
14 ₀₁₄	—	16212.363	-0.028
13 ₀₁₃	—	16212.599	-0.031
12 ₀₁₂	—	16212.835	-0.017
10 ₀₁₀	—	16213.227	-0.015
9 ₀₉	—	16213.396	-0.015
8 ₀₈	—	16213.544	-0.020
7 ₀₇	—	16213.676	-0.022
5 ₀₅	—	16213.898	-0.019
4 ₀₄	—	16213.990	-0.010
3 ₀₃	—	16214.054	-0.014
2 ₀₂	—	16214.104	-0.014
1 ₀₁	—	16214.138	-0.013
2 ₀₂	—	16215.471	-0.009
3 ₀₃	—	16216.074	-0.017
4 ₀₄	—	16216.662	-0.012
5 ₀₅	—	16217.218	-0.008
6 ₀₆	—	16217.741	-0.007
7 ₀₇	—	16218.224	-0.018
8 ₀₈	—	16218.701	-0.005
9 ₀₉	—	16219.120	-0.019
10 ₀₁₀	—	16219.548	0.006
11 ₀₁₀	—	16222.634	0.011
10 ₀₁₀	—	16223.522	0.026
8 ₁₇	—	16225.196	0.002
7 ₁₆	—	16226.026	0.007
6 ₁₅	—	16226.820	-0.007
5 ₁₄	—	16227.627	0.008
4 ₁₃	—	16228.405	0.009
2 ₁₁	—	16229.915	0.017
18 ₁₁₈	—	16227.020	0.012
17 ₁₁₇	—	16227.548	0.015
16 ₁₁₆	—	16228.026	-0.002
15 ₁₁₅	—	16228.504	0.008
14 ₁₁₄	—	16228.950	0.015
13 ₁₁₃	—	16229.366	0.021
10 ₁₁₀	—	16230.421	0.016
9 ₁₀₉	—	16230.706	0.007
8 ₁₀₈	—	16230.964	0.000
7 ₁₀₇	—	16231.211	0.010
6 ₁₀₆	—	16231.414	0.007
5 ₁₀₅	—	16231.597	0.013
4 ₁₀₄	—	16231.733	0.000
3 ₁₀₃	—	16231.855	0.004
2 ₁₀₂	—	16231.935	-0.005
1 ₁₀₁	—	16232.009	0.010
2 ₁₀₁	—	16233.397	0.031
3 ₁₀₂	—	16234.031	0.021
4 ₁₀₃	—	16234.655	0.017
5 ₁₀₄	—	16235.279	0.030
6 ₁₀₅	—	16235.870	0.026
7 ₁₀₆	—	16236.458	0.037
8 ₁₀₇	—	16236.998	0.015
9 ₁₀₈	—	16237.568	0.039
10 ₁₀₉	—	16238.082	0.024
11 ₁₁₀	—	16238.585	0.015

Table 1 (continued)

J''_{KaKc}	J''_{KaKc}	v_{obs} (cm $^{-1}$)	$o - c$ (cm $^{-1}$)
3 ₂₂	—	16248.225	-0.016
4 ₂₁	—	16248.225	-0.026
3 ₂₁	—	16248.331	0.013
2 ₂₁	—	16248.331	0.001
2 ₂₀	—	16249.742	0.012
2 ₂₁	—	16249.742	-0.001
3 ₂₁	—	16250.349	0.007
3 ₂₂	—	16250.392	0.012
4 ₂₂	—	16250.914	-0.010
4 ₂₃	—	16250.990	-0.010
5 ₂₃	—	16251.444	-0.034
5 ₂₄	—	16251.578	-0.026
6 ₂₅	—	16252.156	-0.036

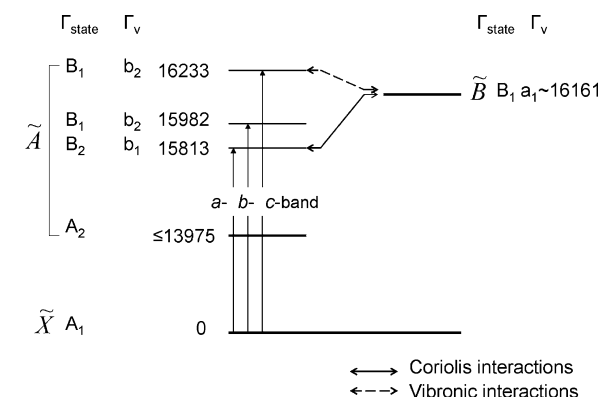


Fig. 2. Vibronic energy level diagram (cm $^{-1}$) of propadienyliidene. The possible vibronic and Coriolis interactions are indicated by dotted and thick arrows respectively. Three observed transitions are shown by solid arrows. Vibrational ground state in the \tilde{X}^1A_1 , \tilde{A}^1A_2 electronic states are denoted by thick bars and vibrational excited states in the \tilde{A}^1A_2 electronic state are by thin bars. The capital letter stands for the symmetry of the electronic state; lowercase letter—vibronic symmetry.

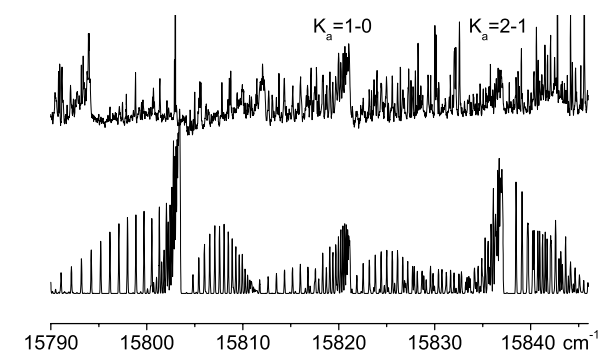


Fig. 3. Rotationally resolved electronic absorption spectrum of the a -band in the $\tilde{A}^1A_2-\tilde{X}^1A_1$ transition of H_2CCC (upper trace) and the simulation (lower trace) at 20 K, using a single Boltzmann population model for the two nuclear spin isomers (spin statistical weights $ee:eo:oe:oo = 1:1:3:3$). The $K_a = 0-1$ structure is missing due to a -type Coriolis perturbation.

Table 2
Molecular constants (cm^{-1})^a of H₂CCC

State	Constant	<i>a</i> -band		<i>b</i> -band ^b	<i>c</i> -band		Microwave ^c
		Fit I	Fit II	Fit II	Fit I	Fit II	
\tilde{X}^1A_1	<i>A</i> ''	9.6451 ^d	9.6451 ^d	9.6451(17)	9.6688(28)	9.6451 ^d	9.6328(11)
	<i>B</i> ''	0.35326(22) ^e	0.353198 ^f	0.353198 ^f	0.35315(14) ^e	0.353198 ^f	0.353198(67)
	<i>C</i> ''	0.34043(22) ^e	0.340367 ^f	0.340367 ^f	0.34075(14) ^e	0.340367 ^f	0.340367(67)
	1/2(<i>B</i> '' + <i>C</i> '')	0.34681(22)			0.34695(14)		0.346783(67)
\tilde{A}^1A_2	<i>A</i> '	8.7525(39) ^g	8.7526(37) ^g	9.83717(46)	8.8987(10)	8.8977(16)	
	<i>B</i> '	0.34076(46)	0.34070(22)	0.341217(86)	0.34204(15)	0.341750(91)	
	<i>C</i> '	0.33046(46)	0.33039(15)	0.328764(91)	0.32883(14)	0.328695(49)	
	<i>T</i> ₀₀ ^h	15812.792(10)	15812.7913(95)	15982.0367(16)	16223.4777(32)	16223.4673(40)	

^a Values in parentheses denote the standard deviation.

^b Ref. [8].

^c Ref. [7].

^d Fixed to the value of [8].

^e Ratio between *B* and *C* constants is fixed to that of [7].

^f Fixed to the value of [7].

^g Accurate determination of this value is hindered by the Coriolis interaction.

^h Error arises from the least-squares fitting and 0.05 cm^{-1} uncertainty of the calibration.

A number of different C₃H₂ isomers were studied both theoretically [10] and experimentally [11] during the past decades. The most stable isomer is a singlet cyclopropenylidene: H₂CCC lies 0.59 eV higher in energy than cyclopropenylidene (see Fig. 7 in [2]). An activation barrier between propadienylidene and cyclopropenylidene is 1.81 eV [2], that is lower than the 2.0 eV excitation energy for the \tilde{B}^1B_1 – \tilde{X}^1A_1 transition. However in all three states \tilde{X} , \tilde{A} , and \tilde{B} propadienylidene has C_{2v} symmetry, i.e., there are but small geometry differences [8]. Thus, upon excitation the C_{2v} structure does not rearrange to a cyclic one and excludes this isomerization pathway as a possible reason for the shortened lifetime. Rearrangement to the quasi-linear HCCCCH is unlikely because high barriers are present [2].

Predissociation processes can also decrease the lifetime of an electronic state. There are several pathways of C₃H₂ dissociation discussed in the literature [2,12]. The major channel is expected to be an elimination of H₂ because it has the lowest activation barrier calculated to be 3.71 eV [2]. Another possible dissociation pathway, C₃H₂ → C₃H + H, has slightly higher activation energy (3.87 eV) [2]. Both of these values are too high for these processes to play a role in the shortening of the \tilde{B}^1B_1 state lifetime.

The short lifetime of the \tilde{B}^1B_1 state can be also attributed to intersystem crossing to the triplet states, ³A₂ and ³B₁, lying 0.44 and 0.77 eV lower in energy than \tilde{B}^1B_1 state [13], and/or internal conversion to the nearby \tilde{A}^1A_2 state (energy gap of ~0.16 eV [8]) via a conical intersection. It will require a detailed theoretical study to get an insight as to the relaxation pathway.

While searching for the \tilde{B}^1B_1 – \tilde{X}^1A_1 transitions in the 15768–16282 cm^{-1} region two similar groups of lines were found near 15812.8 and 16223.5 cm^{-1} , denoted as the *a*- and *c*-bands, respectively. Their rotational structure could be resolved with a laser linewidth of 0.05 cm^{-1} .

3.2. *c*-band

The transition around 16233 cm^{-1} was detected at first. Under jet-cooled conditions it consists of three subbands $K_a = 0 \leftarrow 1$, $K_a = 1 \leftarrow 0$, and $K_a = 2 \leftarrow 1$ as shown in Fig. 1. Based on the rotational profile and the position of the transition, the carrier is H₂CCC.

Initially the *P*, *Q*, and *R* branches of the three subbands were fitted to a polynomial. A least-squares fit to the frequencies of 76 lines was made with a conventional rotational Hamiltonian for an asymmetric top molecule without centrifugal distortion terms using the program WANG. The obtained rotational constant 1/2(*B*'' + *C*'') for the ground state matched with the microwave value within error in the initial fitting (Fit I in Table 2). The agreement of rotational constants confirmed that the observed transition is due to the H₂CCC species. It is assigned to the forbidden electronic transition \tilde{A}^1A_2 – \tilde{X}^1A_1 because of its weak intensity. In the next step the ground state *B*'' and *C*'' constants were fixed to the microwave values [7]. The *A*'' constant was taken from [8], where it was determined from the separations of the subbands using high resolution cw-CRD spectroscopy. The result of this is Fit II in Table 2 and the line frequencies are listed in Table 1.

The simulated spectrum with the constants from Fit II and a single Boltzmann population for the two nuclear spin isomers is shown in Fig. 1. The intensity distribution of the *K*-structure is in agreement with the observation. An independent Boltzmann population model fails because (i) the laser beam crossed the supersonic jet 2 mm downstream from the slit nozzle, where the collisions between H₂CCC and the rare gas are still occurring. Thus full collisional equilibration has not been attained. (ii) The observed transition is vibronically induced (see following section), and hence the intensities are affected by vibronic interaction with the nearby ¹B₁ state.

Table 3
Frequencies of the observed rovibronic lines for the a -band in the $\tilde{A}^1A_2-\tilde{X}^1A_1$ electronic transition of H₂CCC

J''_{KaKc}		J''_{KaKc}	ν_{obs} (cm ⁻¹)	$o - c$ (cm ⁻¹)
8 ₁₇	—	9 ₀₉	15814.323	-0.023
7 ₁₆	—	8 ₀₈	15815.207	0.030
6 ₁₅	—	7 ₀₇	15816.015	0.023
5 ₁₄	—	6 ₀₆	15816.755	-0.033
3 ₁₂	—	4 ₀₄	15818.317	-0.014
11 ₁₁₁	—	11 ₀₁₁	15819.381	-0.012
10 ₁₁₀	—	10 ₀₁₀	15819.692	-0.002
9 ₁₉	—	9 ₀₉	15819.980	0.011
8 ₁₈	—	8 ₀₈	15820.216	0.000
7 ₁₇	—	7 ₀₇	15820.451	0.015
6 ₁₆	—	6 ₀₆	15820.644	0.015
5 ₁₅	—	5 ₀₅	15820.778	-0.016
4 ₁₄	—	4 ₀₄	15820.918	-0.014
3 ₁₃	—	3 ₀₃	15821.060	0.017
1 ₁₀	—	0 ₀₀	15821.901	0.016
2 ₁₁	—	1 ₀₁	15822.540	-0.004
3 ₁₂	—	2 ₀₂	15823.176	-0.009
4 ₁₃	—	3 ₀₃	15823.828	0.019
6 ₁₅	—	5 ₀₅	15824.978	-0.029
7 ₁₆	—	6 ₀₆	15825.575	-0.004
8 ₁₇	—	7 ₀₇	15826.138	0.004
9 ₁₈	—	8 ₀₈	15826.685	0.012
2 ₂₀	—	1 ₁₀	15838.478	0.004
2 ₂₁	—	1 ₁₁	15838.478	-0.009
3 ₂₁	—	2 ₁₁	15839.109	0.022
3 ₂₂	—	2 ₁₂	15839.109	-0.017

As the detected band is a c -type transition, the vibrational component in the upper state belongs to b_2 symmetry and the vibronic symmetry is B_1 .

The calculated potential energy surface indicates that the \tilde{B} and \tilde{A} states intersect ~ 115 – 155 cm⁻¹ above the minimum of the 1B_1 energy surface [8]. Thus state mixing is probable and the intensity of the c -band could come from this. Although the \tilde{B}^1B_1 state has a short lifetime no line broadening in the c -band is observed. There are at least two possible causes: 1. because the intensity of the c -band is much weaker than of the $\tilde{B}^1B_1-\tilde{X}^1A_1$ transition, the lifetime of the \tilde{A}^1A_2 state is only slightly shortened and the broadening of the $\tilde{A}^1A_2-\tilde{X}^1A_1$ transition is not detected in the present experiment 2; the molecule is non-planar in the A state, i.e., the symmetry is lowered from C_{2v} to C_s ,

and the transition is therefore not dipole forbidden. Observation of the transition to the $\nu = 0$ level of the \tilde{A}^1A_2 state and determination of the inertial defect could give an indication of this.

In a previous work ab initio calculations of the vibrational frequencies for the 1A_2 state were carried out using the CASSCF method [8]. From these results the investigated band can not be uniquely identified. The lowest energy peak in the $\tilde{A}^1A_2-\tilde{X}^1A_1$ transition in the neon matrix spectrum is at 13975 cm⁻¹ [6]. Thus the vibrational frequency of the c -band should be ≥ 2000 cm⁻¹, even taking into account a matrix-gas shift of around 100 cm⁻¹. According to symmetry and frequency the following combinations of vibrational modes are possible: (i) $\omega_4(a_1) + \omega_8(b_2)$: 1983 cm⁻¹ (the same combination of modes is mentioned as a tentative assignment for b -band in ref [8]), (ii) $\omega_3(a_1) + \omega_8(b_2)$: 2377 cm⁻¹, (iii) $\omega_2(a_1) + \omega_8(b_2)$: 2648 cm⁻¹.

3.3. a -band

The second transition observed at 15813 cm⁻¹ has an unusual rotational structure: the $K_a = 0 \leftarrow 1$ subband is missing (Fig. 3). The high-resolution spectrum has been analysed in a similar manner as described for the c -band. Based on Fit I the observed transition is assigned to the $\tilde{A}^1A_2-\tilde{X}^1A_1$ vibronic transition of H₂CCC. Fit II (ground state constants fixed to the values from [7]) provided excited state rotational constants which are listed in Table 2.

The missing $K_a = 0 \leftarrow 1$ subband suggests that intensity is borrowed through an a -type Coriolis interaction. This absence cannot be explained by an abnormal Boltzmann population of the K -levels because a $K_a = 0 \leftarrow 1$ subband appears clearly in the simulated spectrum. Coriolis interactions can occur between levels with the same angular momentum and rovibronic symmetry. In the theoretical survey of the Coriolis effect [14] it was shown that the intensity of the forbidden electronic transition of formaldehyde induced by rotation is proportional to K_a^2 . Therefore, the absence of the $K_a = 0 \leftarrow 1$ subband is a peculiarity for the rotational structure of a vibronic transition induced by Coriolis interaction, as seen for the a -band (Table 3).

Table 4
Molecular structure and inertial defect of C₃H₂^a

State	Band	Δ^b	Bond length (Å)				Angle (°)
			C ₁ -C ₂	C ₂ -C ₃	C ₁ -C ₃	C ₃ -H	C ₂ -C ₃ -H
\tilde{X}^1A_1	0 ^c	0.0515	1.291	1.324	2.615	1.098	118.8
\tilde{A}^1A_2	a -band	-0.3827	1.3109(58)	1.367 ^d	2.6779(58)	1.082 ^d	115.387(12) ^e
	b -band		1.2948(24)	1.367 ^d	2.6618(24)	1.082 ^d	121.5511(35)
	c -band	0.0645	1.3092(11)	1.367 ^d	2.6762(11)	1.082 ^d	116.3584(20)

^a Values in parentheses denote the standard deviation and apply to the last digits.

^b Inertial defect (amu Å²).

^c Ref. [7].

^d Fixed to the ab initio values for the 1A_2 state in [8].

^e Accurate determination of this value is hindered by the Coriolis interaction.

Although only four transition were assigned in the $K_a = 2 \leftarrow 1$ subband of the a -band, the Q branch band head confirmed the assignment. The distance between the band heads of the adjacent subbands determines ΔA , which should not differ much from those of b - and c -bands.

Because the observed band is a c -type transition and considering a -type Coriolis interaction, the symmetry of the present vibronic state is B_2 with a b_1 vibrational component. Thus the observed transition borrowed its intensity through an interaction with the \tilde{B}^1B_1 state (Fig. 2).

The vibrational frequency should be $\geq 1600 \text{ cm}^{-1}$ even though a gas-matrix shift exists. A trial vibrational assignment gives rise to the following possible combinations: (i) $\omega_3 (a_1) + \omega_5 (b_1)$: 1966 cm^{-1} , (ii) $\omega_2 (a_1) + \omega_6 (b_1)$: 2044 cm^{-1} , (iii) $\omega_2 (a_1) + \omega_5 (b_1)$: 2237 cm^{-1} [8].

3.4. Molecular structure

The structure of H_2CCC in the ground state was determined to be a near prolate top with C_{2v} symmetry according to the analysis of the millimetre-wave spectrum [15]. The inertial defect Δ calculated from the rotational constants is just $0.0515 \text{ amu } \text{\AA}^2$ implying a near planar species.

To follow the structural changes upon electronic excitation, Δ was calculated for the a and c observed transitions. As shown in Table 4, the structure is no longer planar when the a transition is excited, suggesting that one of the out-of-plane vibrations of b_1 symmetry is involved, as already indicated from the rotational analysis. The inertial defect for the c transition was calculated to be $0.0645 \text{ amu } \text{\AA}^2$ implying that the molecule remains planar in the upper electronic state.

The rotational constants were used to determine the structural parameters for the 1A_2 excited state of propadienylidene species. The $r(C_2-C_3)$ and $r(C_3-H)$ distances were fixed to the ab initio values. The bond length $r(C_1-C_2)$ and

angle $\theta (C_2-C_3-H)$ were new determined to be 1.31 \AA , 115.39° and 1.31 \AA , 116.36° for the a and c transitions, respectively (Table 4).

Acknowledgments

This work has been supported by Swiss National Science Foundation (Grant 200020-100019) and is part of the European Union project ‘‘Molecular Universe’’ (MRTN-CT-2004-512303).

References

- [1] J.A. Miller, J.V. Volponi, J.-F. Pauwels, *Combust. Flame* 105 (1996) 451–461.
- [2] A.M. Mebel, W.M. Jackson, A.H.H. Chang, S.H. Lin, *J. Am. Chem. Soc.* 120 (1998) 5751–5763.
- [3] G. Maier, H.P. Reisenauer, W. Schwab, P. Carsky, B.A. Hess, L.J. Schaad, *J. Am. Chem. Soc.* 109 (1987) 5183–5188.
- [4] P. Thaddeus, M.C. McCarthy, *Spectrochim. Acta A* 57 (2001) 757–774.
- [5] A.J. Apponi, M.C. McCarthy, C.A. Gottlieb, P. Thaddeus, *Astrophys. J.* 530 (2000) 357–361.
- [6] J.A. Hodges, R.J. McMahon, J.F. Stanton, K.W. Sattelmeyer, *Astrophys. J.* 544 (2000) 838–842.
- [7] J.M. Vrtilik, C.A. Gottlieb, E.W. Gottlieb, T.C. Killian, P. Thaddeus, *Astrophys. J.* 364 (1990) L53–L56.
- [8] P. Birza, A. Chirakolava, M. Araki, P. Kolek, J.P. Maier, *J. Mol. Spectrosc.* 229 (2005) 276–282.
- [9] M. Araki, T. Motylewski, P. Kolek, J.P. Maier, *Phys. Chem. Chem. Phys.* 7 (2005) 2138–2141.
- [10] R.A. Seburg, E.V. Patterson, J.F. Stanton, R.J. McMahon, *J. Am. Chem. Soc.* 119 (1997) 5847–5856, and references therein.
- [11] J.W. Huang, W.R.M. Graham, *J. Chem. Phys.* 93 (1990) 1583–1596, and references therein.
- [12] W.M. Jackson, D.S. Anex, R.E. Continetti, Y.T. Lee, *J. Chem. Phys.* 95 (1991) 7327–7336.
- [13] M. Rubio, J. Stalring, A. Bernhardsson, R. Lindth, B.O. Roos, *Theor. Chem. Acc.* 105 (2000) 15–30.
- [14] J.A. Pople, J.W. Sidman, *J. Chem. Phys.* 27 (1957) 1270–1277.
- [15] C.A. Gottlieb, T.C. Killian, P. Thaddeus, P. Botschwina, J. Fluegge, M. Oswald, *J. Chem. Phys.* 98 (1993) 4478–4485.

Curriculum vitae

Personal information:

Name: Alexey Denisov
Day of birth: 09.11.1981
Place: Novosibirsk, Russia
Nationality: Russian
Marital status: Married

Education:

1987 – 1997 Primary and secondary school No. 25, Novosibirsk
1997 – 2001 Novosibirsk State University, Natural Sciences Department, Novosibirsk, Russia. B.Sc. in Environmental Chemistry.
2001 – 2003 Novosibirsk State University, Natural Sciences Department, Novosibirsk, Russia. M.Sc. in Chemistry.
2001 – 2006 University of Basel, Department of Chemistry, Switzerland, Ph.D. work in the group of Prof. John. P. Maier

The list of publications

1. Cias, P., et al., *Electronic gas-phase spectrum of the pentaacetylene cation*. Journal of Physical Chemistry A, 2002. **106**(42): p. 9890-9892.
2. Araki, M., et al., *High-resolution electronic spectroscopy of a nonlinear carbon chain radical $C_6H_4^+$* . Journal of Chemical Physics, 2003. **118**(23): p. 10561-10565.
3. Denisov, A., et al., *Sulfur terminated nanowires in the gas phase: laser spectroscopy and mass spectrometry*. International Journal of Mass Spectrometry, 2004. **233**(1-3): p. 131-136.
4. Cias, P., et al., *Gas phase detection of cyclic B_3 : $2^2E' \leftarrow X^2A_1'$ electronic origin band*. Journal of Chemical Physics, 2004. **121**(14): p. 6776-6778.
5. Araki, M., et al., *Electronic spectroscopy of the nonlinear carbon chains $C_4H_4^+$ and $C_8H_4^+$* . Canadian Journal of Chemistry-Revue Canadienne De Chimie, 2004. **82**(6): p. 848-853.
6. Araki, M., et al., *New laboratory data on a molecular band at 4429 angstrom*. Astrophysical Journal, 2004. **616**(2): p. 1301-1310.
7. Achkasova, E., et al., *Rotational analysis of the $A^2B_1 \leftarrow X^2A_2$ electronic spectrum of the allyl radical*. Molecular Physics, 2005. **103**(11-12): p. 1555-1560.
8. Achkasova, E., et al., *Gas phase electronic spectrum of propadienyliidene C_3H_2* . Journal of Molecular Spectroscopy, 2006. **237**(1): p. 70-75.